MINISTRY OF EDUCATION

THE ANNALS OF "DUNAREA DE JOS" UNIVERSITY OF GALATI

Fascicle IX
METALLURGY AND MATERIALS SCIENCE

YEAR XXXIX (XLIV)
September 2021, no. 3

ISSN 2668-4748; e-ISSN 2668-4756

2021
GALATI UNIVERSITY PRESS

EDITORIAL BOARD

THE ANNALS OF "DUNAREA DE JOS" UNIVERSITY OF GALATI
FASCICLE IX. METALLURGY AND MATERIALS SCIENCE
Nº. 3 - 2021, ISSN 2668-4748; e-ISSN 2668-4756
Volume DOI: https://doi.org/10.35219/mms.2021.3

Table of Contents

THE ANNALS OF "DUNAREA DE JOS" UNIVERSITY OF GALATI
FASCICLE IX. METALLURGY AND MATERIALS SCIENCE
Nº. 3 - 2021, ISSN 2668-4748; e-ISSN 2668-4756
Volume DOI: https://doi.org/10.35219/mms.2021.3

THE ANNALS OF "DUNAREA DE JOS" UNIVERSITY OF GALATI
FASCICLE IX. METALLURGY AND MATERIALS SCIENCE
No. 3 - 2021, ISSN 2668-4748; e-ISSN 2668-4756
Article DOI: https://doi.org/10.35219/mms.2021.3.01

ON THE FREE RECOVERY BENDING SHAPE MEMORY EFFECT IN POWDER METALLURGY FeMnSiCrNi

Lenuța CIURCĂ, Bogdan PRICOP, Mihai POPA, Victor Daniel APOSTOL, Leandru-Gheorghe BUJOREANU*
Faculty of Materials Science and Engineering, „Gheorghe Asachi" Technical University of Iași, Blvd. Dimitrie Mangeron 61A. 700050 Iași, Romania
e-mail: leandru-gheorghe.bujoreanu@academic.tuiasi.ro

ABSTRACT

This paper presents the results of an original experimental study on the training capacity of a powder metallurgy (PM) FeMnSiCrNi shape memory alloy (SMA). The specimens were sintered under protective atmosphere from blended elemental powders, 50 vol.%. of alloy particles being mechanically alloyed. Lamellar specimens, hot rolled to 1 mm thickness, were bent against cylindrical calibres with five decreasing radii, to induce cold shapes with higher and higher deformation degree, as compared to the straight hot shape. During the training procedure, bent specimens were heated with a hot air gun, and developed free-recovery shape memory effect (SME) and partially deflected, by reducing their curvature. The first set of experiments involved fastening the specimens at one end, heating it and monitoring free end's displacement by means of cinematographic analysis. Within the second set of experiments, both cold and hot shapes were recorded and digitalized and their chord's length (b) and circle segment height (a) were measured and the radius was determined as $R = a/2 + b^2/8a$ *for the cold (*R_c*) and hot shapes (*R_h*). Finally, the shape recovery degree was calculated for the* n^{th} *calibre as* $\Delta_{recn} = (R_h^n - R_r^n)/(R_h^{n-1} - R_r^n)$ *and the variation of* Δ_{recn} *with calibre's radius was discussed.*

KEYWORDS: shape memory effect, training, shape recovery degree, PM FeMnSiCrNi

1. Introduction

Shape memory effect (SME) represents the most prominent characteristic of shape memory materials and consists in the recovery of a permanent (hot) shape, as an effect of applying a stimulus (*e.g.*, heat, magnetic field, radiation, pH changing or water acceptance/rejection) to a material which has a temporary (cold) shape [1]. Shape memory materials include alloys, ceramics, polymers, composites and hydrides [2]. The first report on SME presence in alloys, refers to Au-Cd system and has an age of seven decades [3]. The same alloy system was exhibited seven years later, for the 1958 Brussels Universal and International Exhibition, under the form of cylindrical single crystal Ø 3 × 10 cm, which was martensitic at room temperature (RT), and represented the active part of a cyclic weight lifting device. The single crystal weighed approx. 10 g and had a 50 g weight fastened at its free end that bent it to a large extent. After heating, the cylinder became austenitic, therefore more strengthened and it lifted the load [4]. The list of alloy systems exhibiting SME rapidly increased with In-Tl (1953), Cu-Zn (1956), Cu-Al-Ni (1957), Ni-Ti (1963), Cu-Zn-Al (1970), Ti-Nb (1971), Au-Cu-Zn (1971), Ni-Al (1971), Fe-Pt (1971), Cu-Zn-Sn (1972), Cu-Zn-Si (1972), Ag-Cd (1973), Cu-Sn (1973), Cu-Zn-Ga (1974), Ti-Pd-Ni (1982), Fe-Mn-Si (1982) [5], and more recently Fe-Ni-Co-Al-Ta-B (2010) [6] and Fe-Mn-Al-Ni (2011) [7]. For each of these binary or ternary alloy systems, which have been finally designated as shape memory alloys (SMAs), quaternary, quintenary, etc. concentrations have been developed, by cumulating the beneficial effects of an increasing number of alloying elements.

Besides the above-mentioned alloy systems that are thermally activated, there is also an entire class of magnetically-driven SMAs [8] but their presentation falls beyond the scope of the present paper.

THE ANNALS OF "DUNAREA DE JOS" UNIVERSITY OF GALATI
FASCICLE IX. METALLURGY AND MATERIALS SCIENCE
Nº. 3 - 2021, ISSN 2668-4748; e-ISSN 2668-4756
Article DOI: https://doi.org/10.35219/mms.2021.3.01

In the specific case of Fe-Mn-Si SMAs, SME is based on thermally induced reversion to γ-face centered cubic (fcc) austenite of ε-hexagonal close packed (hcp) martensite which was stress induced when imprinting the temporary (cold) shape [9]. The development of Fe-Mn-Si based SMAs led to Fe-Mn-Si-Cr (1990) [10] and Fe-Mn-Si-Cr-Ni (1991) [11]. Fe-Mn-Si-Cr-Ni SMAs are corrosion resistant and they are able to recover strains as large as 7.7 % [12].

The most accessible method, for SME evaluation in straight lamellar specimens, consists in their progressive bending, at RT, against a small diameter cylindrical calibre and in subsequent heating. After measuring the bending (α_{max}), the unloading ($\alpha_{cold} < \alpha_{max}$, since the specimen has a small spring back during unloading) and the heating angles ($\alpha_{hot} < \alpha_{cold}$, since the specimens partially recover their straight) shape recovery degree is determined as $\Delta_{rec} = (\alpha_{cold} - \alpha_{hot})/ \alpha_{cold} \times 100$. Ideally, $\Delta_{rec} = 100$ % if $\alpha_{hot} = 0^o$ and the specimen completely recovered its straight shape [13].

As previously pointed out, powder metallurgy (PM) including mechanical alloying (MA) has the potential to represent an alternative processing technique for Fe-Mn-Si-Cr-Ni SMAs [14]. Nevertheless, in an Fe-Mn-Si-Cr-Ni SMA prepared by PM and containing 50 vol.% of MA'ed powder, up to 32 % α' - body centered cubic (bcc) martensite has been formed [15] which diminishes the magnitude of SME due to the obstruction of reverse martensitic transformation [16].

The present paper aims to investigate the training capacity of a powder metallurgy (PM) Fe-14Mn-6Si-9Cr-5Ni SMA with 50 vol.%. of mechanically alloyed particles, when subjected to SME cycles.

2. Experimental procedure

Lamellar (1 × 10 × 113 mm) specimens have been cut by wire spark erosion from an Fe-14Mn-6Si-9Cr-4Ni (wt.%) SMA which was pressed, sintered, homogenized and hot-rolled as previously pointed out [17].

These specimens are rather fragile and must be plastically deformed with great care as to avoid cracking [18]. For this reason, the specimens were progressively bent, at RT, against cylindrical calibres with decreasing radii. When two calibres were used, the specimens were bent between them. When a single calibre was used the specimens were bent along its outer surface being fastened by a grip or it was bent into its inner surface. Figure 1 shows the five calibres used for the present experiments.

Figure 2 shows successive stages of cold shape inducing during training. It is noticeable that the specimens changed their hot (straight) shape, from Figure 2(a) to a clod (curved) shape, in Figure 2(g). If this shape was induced directly, from the straight shape, the specimen would definitely crack. Nevertheless, the cold shape radius is much larger than the radius of the last calibre (18.4 mm), due to material's spring back.

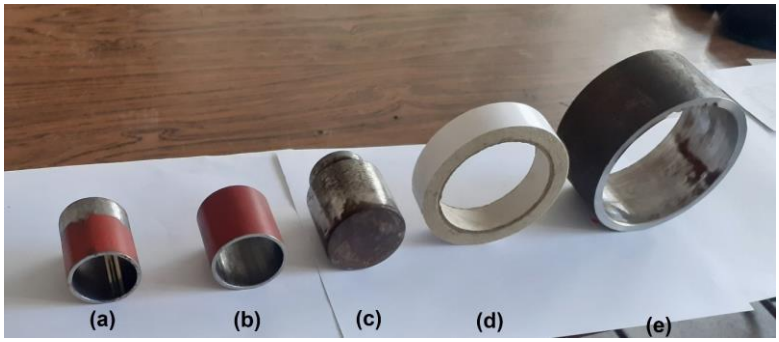

Fig. 1. *Succession of radius-increasing calibers used for cold shape induction, with the following radii: (a) interior - 18.39 mm and exterior - 21.71 mm; (b) interior - 24.4 mm; (c) exterior - 27.8 mm; (d) interior - 37.5 mm and (e) interior - 50 mm*

After inducing the cold shape, the specimens have been subjected to two types of training procedures, comprising the monitoring of: (i) free end's vertical displacement and (ii) curvature radius, during SME cycles (heating-cooling-deformation). Figure 3 illustrates two experimental stages of the training procedure involving the monitoring of specimen's free end vertical displacement with temperature. The specimen, with induced cold shape, has one end fastened in a grip, a thermocouple fixed on its surface and it is heated by a hot air gun. Specimen's deflection by SME is filmed and each vertical position of the specimen's free end is associated to a temperature value. For instance, Figure 3(b) shows specimen's free end position after heating with 140 ºC.

THE ANNALS OF "DUNAREA DE JOS" UNIVERSITY OF GALATI
FASCICLE IX. METALLURGY AND MATERIALS SCIENCE
Nº. 3 - 2021, ISSN 2668-4748; e-ISSN 2668-4756
Article DOI: https://doi.org/10.35219/mms.2021.3.01

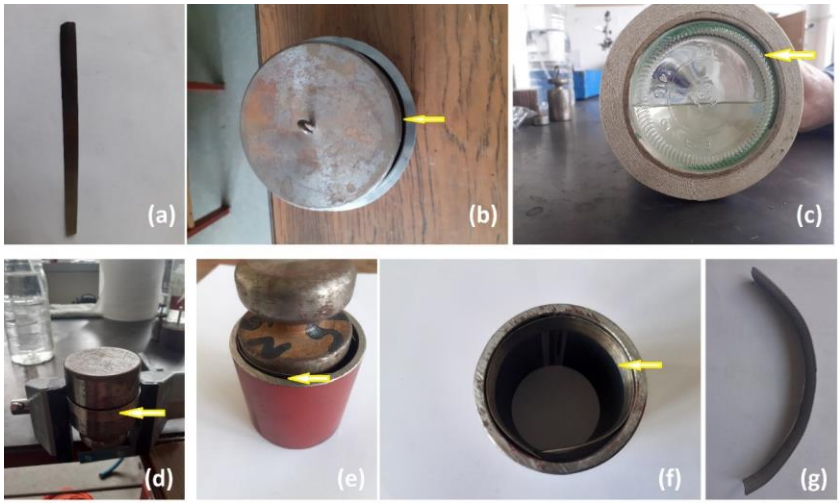

Fig. 2. *Successive stages of cold shape inducing during training: (a) initial straight (hot) shape; (b) inducing the cold shape with 50 mm-radius by means of outer and inner calibers; (c) inducing the cold shape with 37.5 mm-radius by means of outer and inner calibers; (d) inducing the cold shape with 27.8 mm-radius by means of an outer caliber and a grip; (e) inducing the cold shape with 24.4 mm-radius by means of outer and inner calibers; (f) inducing the cold shape with 18.4 mm-radius by means of an inner caliber; (f) final cold shape*

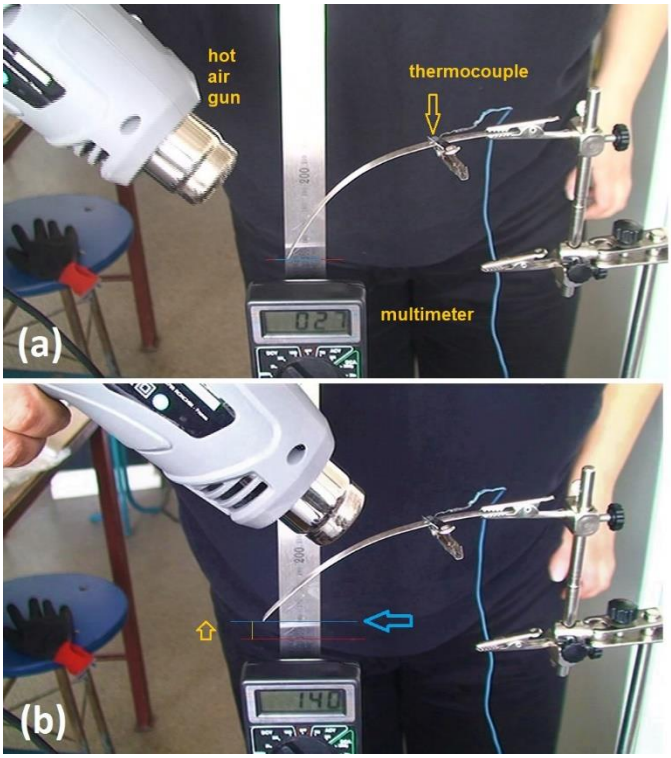

Fig. 3. *Experimental stages of the training procedure by free-recovery bending shape memory effect of a PM Fe-14Mn-6Si-9Cr-5Ni (wt.%) SMA: (a) initial stage, at RT, with the free end of the specimen with cold shape in the position marked with blue line; (b) final stage, after heating to 140 ºC, when specimen's free end (marked with blue arrow) developed the displacement marked with yellow arrow*

THE ANNALS OF "DUNAREA DE JOS" UNIVERSITY OF GALATI
FASCICLE IX. METALLURGY AND MATERIALS SCIENCE
N°. 3 - 2021, ISSN 2668-4748; e-ISSN 2668-4756
Article DOI: https://doi.org/10.35219/mms.2021.3.01

Within the second training procedure, the specimen, with induced cold shape, is placed on a plate and heated with the hot air gun. Both cold and hot shapes have been recorded and digitalized (by means of GeoGebra software) and their chord's length (b) and circle segment height (a) have been measured and the radius was determined as:

$$R = a/2 + b^2/8a \quad (1)$$

for the cold (R_c) and hot shapes (R_h), in accordance with Figure 4. Finally, shape recovery degree after the bending against the nth calibre was calculated as:

$$\Delta_{rec}^{n} = (R_h^n - R_r^n) / (R_h^{n-1} - R_r^n) \quad (2)$$

and the variation of Δ_{rec}^{n} with calibre's radius was discussed. In the above, R_h^{n-1} is the radius of the hot shape after specimen bending against the n-1th calibre.

3. Experimental results and discussion

3.1. Training cycles effects on the variation of vertical free end's displacement with temperature

Figure 5 illustrates the variations of specimen's free end displacement with temperature, for the first (c_1) and the nineteenth training cycles (c_{19}) as well as the total displacement rate. The symbols correspond to experimental values and the solid lines to second degree polynomial fits, performed by ORIGIN software.

It is noticeable that the free end's vertical position descended during training while its total stroke was maintained to about 6 mm. Another notable aspect, from Figure 5(a) is the fact the experimental values became better fitted with the theoretical variation, in cycle 19 as compared to cycle 1. The variation of theoretical vertical displacement (d) with temperature (T) has the form:

$$d = -3.87505\ T^2 + 0.11668\ T - 2.70793 \quad (3)$$

This second order polynomial approximation has standard errors ranging between 2.29×10-5 for the coefficient of T^2, and 0.1331, for the constant that would theoretically represent the vertical displacement at T = 0 °C, which has no real physical interpretation.

Figure 5(b) shows that the variation of total displacement rate (dl / dt) with the number of training cycles (N), for the 1st, the 6th and the 10th cycle, are perfectly fitted to a second-degree polynomial, performed by ORIGIN software. The theoretical variation of displacement rate with the number of cycles has the form:

$$dl/dt = -2.09671\ N^2 + 0.00155\ N + 0.1955 \quad (4)$$

Standard error is zero for each coefficient.

3.2. Training cycles effects on radius memory effect in bending

Figure 6 illustrates measuring examples of the chord's length (b) and circle segment height (a), defined in Figure 4, The values are determined by *GeoGebra* software and they correspond to the hot and cold shapes obtained for the last three calibres.

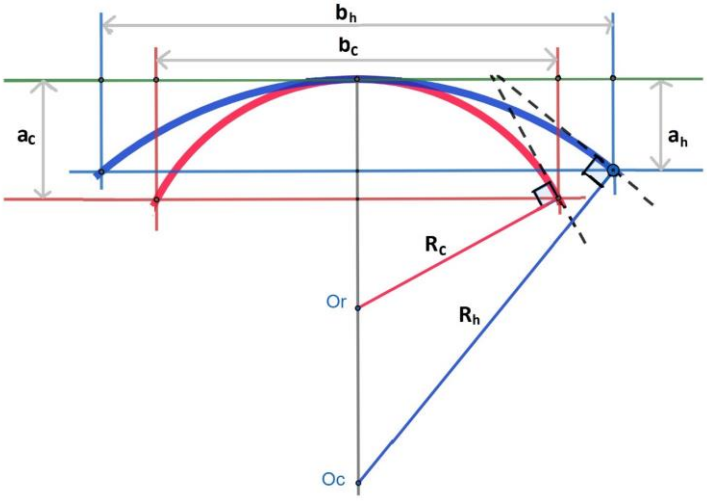

Fig. 4. *Principle scheme for the measurement of circle segment height (a) and chord's length (b) for the hot (h) and cold (c) shapes and for determining their respective radii*

THE ANNALS OF "DUNAREA DE JOS" UNIVERSITY OF GALATI
FASCICLE IX. METALLURGY AND MATERIALS SCIENCE
Nº. 3 - 2021, ISSN 2668-4748; e-ISSN 2668-4756
Article DOI: https://doi.org/10.35219/mms.2021.3.01

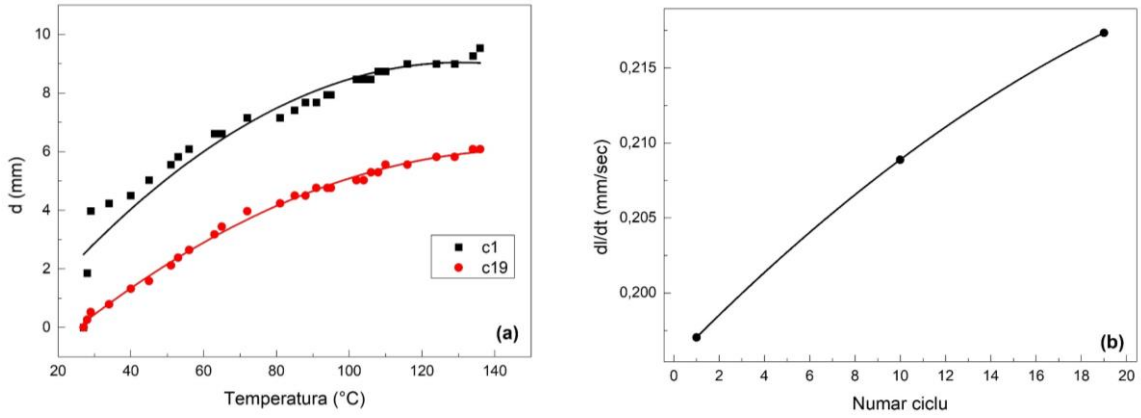

Fig. 5. *Experimental (symbols) and theoretical (solid line) results obtained during the training procedure that monitors the variation of free end's displacement: (a) temperature effects in the 1st and 19th cycles; (b) variation of total displacement rate with the number of cycles*

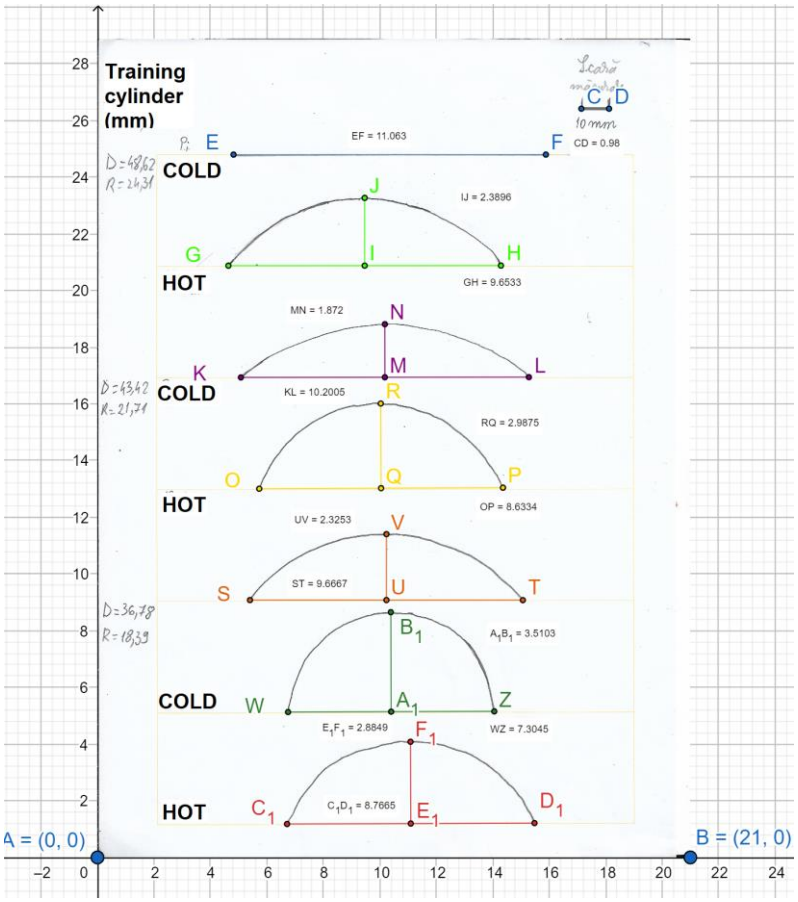

Fig. 6. *Measuring examples of circle segment height and chord's length, corresponding to the first three calibers (lowest radii) from Figure 2, by means of GeoGebra software*

The experimental values of specimen's radii have been calculated with eq. (1) and the values are listed in Tables 1 and 2 for the cold and hot shapes, respectively. It is noticeable that: (i) for each caliber value, $a_{cold} > a_{hot}$, $b_{cold} < b_{hot}$ and $R_{specimen}^{exp,cold} < R_{specimen}^{exp,hot}$ and (ii) due to the large elastic spring back of the specimen, in each case $R_{specimen}^{exp,cold}$ is much larger than $R_{calibre}$.

THE ANNALS OF "DUNAREA DE JOS" UNIVERSITY OF GALATI
FASCICLE IX. METALLURGY AND MATERIALS SCIENCE
Nº. 3 - 2021, ISSN 2668-4748; e-ISSN 2668-4756
Article DOI: https://doi.org/10.35219/mms.2021.3.01

Table 1. *Experimental measurements of cold shape*

a	b	$R_{calibre}$	$R_{specimen}$exp
17.63673	106.4265	50	89.09546
19.09082	105.5857	37.5	82.54087
22.4102	100.9582	27.8	68.05728
24.38367	98.50306	24.31	61.93236
30.58673	88.09592	21.71	47.0101
35.81939	74.53571	18.39	37.29714

Table 2. *Experimental measurements of hot shape*

a	b	$R_{calibre}$	$R_{specimen}$exp
11.35918	110.6316	50	140.3653
12.48469	110.6857	37.5	128.9058
15.12653	108.0878	27.8	104.1069
19.10204	104.0867	24.31	80.4469
23.72755	98.6398	21.71	63.12175
29.43776	89.45408	18.39	48.69749

Finally, the shape recovery degree in the n^{th} cycle has been calculated with eq. (2).

The variation of shape recovery degree with calibre radius is shown in Figure 7. It is noticeable that shape recovery degree varied from 44 %, at a calibre radius of 18.39 mm, to 80 % at a calibre radius of 37.5 mm. This evolution is rather expectable, if one considers that the specimen was subjected to a larger and larger deformation degree, thus accumulating more and more permanent deformation.

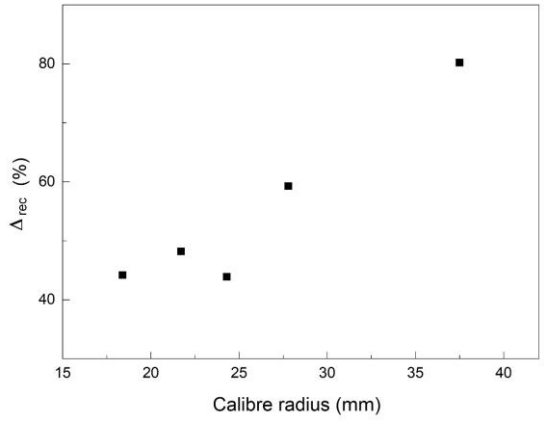

Fig. 7. *Variation of experimental values of recovery degree with the caliber radius*

4. Conclusions

The main conclusions are the following:

- the variation of vertical free end's displacement with temperature, during the training cycles, came closer to a second order polynomial fit under the form:

$$d = -3.87505\ T^2 + 0.11668\ T - 2.70793$$

- the variation of vertical displacement rate with the number of cycles was fitted under the form:

$$dl/dt = -2.09671\ N^2 + 0.00155\ N + 0.1955$$

- with decreasing the radius of the caliber used for cold shape induction, from 37.5 to 18.39 mm, the shape recovery degree decreased from 80 to 44 %, as an effect of the accumulating of permanent deformation.

References

[1]. Sun L., Huang M., Ding Z., Zhao Y., Wang C. C., Purnawali H., Tang C., *Stimulus-responsive shape memory materials: A review*, Materials & Design, 33, p. 577-640, 2012.

[2]. Wilhelm E., Richter C., Rapp B. E., *Phase change materials in microactuators: Basics, applications and perspectives*, Sensor Act. A 271, p. 303-347, 2018.

[3]. Chang L. C., Read T. A., *Plastic deformation and diffusionless phase changes in metals – The gold cadmium beta phase*, Trans. AlME, 189, Journal of Metals, p. 47-52, 1951.

[4]. Lieberman D. S., Schmerling M. A., Karz R. W., *Ferroelastic "memory" and mechanical properties in Gold-Cadmium, in Shape memory Effects in Alloys*, J. Perkins, ed., Plenum Press, New York, p. 203-244, 1977.

[5]. Wayman C. M., Duerig T. W., *An introduction to martensite and shape memory, in: Engineering Aspects of Shape Memory Alloys*, T. W. Duerig, K. N. Melton, D. Stockel, C. M. Wayman, Eds., Butterworth-Heinemann, Oxford, p. 3-20, 1990.

[6]. Tanaka Y., Himuro Y., Kainuma R., Sutou Y., Omori T., Ishida K., *Ferrous Polycrystalline Shape-Memory Alloy Showing Huge Superelasticity*, Science, 327, p. 1488-1490, https://doi.org/10.1126/science.1183169, 2010.

[7]. Omori T., Ando K., Okano M., Xu X., Tanaka Y., Ohnuma I., Kainuma R., Ishida K., *Superelastic Effect in Polycrystalline Ferrous Alloys*, Science, 333, p 68-71, https://doi.org/10.1126/science.1202232, 2011.

[8]. Chernenko V. A., Barandiarán J. M., *Preface, in: Advances in Shape Memory Materials. Ferromagnetic Shape Memory Alloys*, V.A. Chernenko Ed., Trans Tech Publications, 635, p. 1, doi: 10.4028/www.scientific.net/MSF.635.0, 2010.

[9]. Dunne D., *Shape memory in ferrous alloys, in: Phase Transformations in Steels. Vol 2 Diffusionless Transformations, High Strength Steels, Modelling and Advanced Analytical Techniques*, E. Pereloma and D.V. Edmonds, Eds., Woodhead Publishing, Cambridge, p. 83-125, 2012.

[10]. Otsuka H., Yamada H., Maruyama T., Matsuda S., Murakami, *Effects of Alloying Additions on Fe-Mn-Si Shape Memory Alloys*, ISIJ Int, 30, p. 674-679, 1990.

[11]. Moriya Y., Kimura H., Ishizaki S., Hashizume S., Suzuki S., Suzuki H., Sampei T., *Properties of Fe-Cr-Ni-Mn-Si (-Co) shape memory alloys*, J Phys IV, France 01 C4, p. 433-437, 1991.

[12]. Peng H., Wang G., Wang S., Chen J., Mac Laren I., Wen Y., *Key criterion for achieving giant recovery strains in polycrystalline Fe-Mn-Si based shape memory alloys*, Mater. Sci. Eng. A., 712, p. 37-49, doi: 10.1016/j.msea.2017.11.071, 2018.

[13]. Spiridon I.-P., Lohan N.-M., Suru M.-G., Mihalache E., Bujoreanu L.-G., Pricop B., *A study of free recovery in a Fe-Mn-Si-Cr shape memory alloy*, Metal Science and Heat Treatment, 57(9-10), p. 548-552, doi: 10.1007/s11041-016-9920-z, 2016.

[14]. Pricop B., Soyler A. U., Ozkal B., Bujoreanu L. G., *Powder Metallurgy: An Alternative for FeMnSiCrNi Shape Memory Alloys Processing*, Front. Mater., 7, 247 doi: https://doi.org/10.3389/fmats.2020.00247, 2020.

[15]. Pricop B., Söyler U., Özkal B., Lohan N. M., Paraschiv A. L., Suru M. G., Bujoreanu L.-G., *Inf1uence of Mechanical Alloying on the Behavior of Fe-Mn-Si-Cr-Ni Shape Memory Alloys Made by Powder Metallurgy*, Materials Science Forum, 739, p. 237-241, 2013.

[16]. Chen S. C., Chuang C. Y., Yan C. L., Hsu T. L., *Effect of fcc antiferromagnetism on martensitic transformation in Fe-Mn-Si based alloy*, Mater. Sci. Eng. 264, p. 262-268, https://doi.org/10.1016/S0921-5093(98)01105-8, 1999.

[17]. Ciurca L., Lohan N.-M., Pricop B., Bujoreanu L. G., *Study of tensile behaviour of Fe base shape memory alloys during mechanical cycling*, IOP Conf. Ser.: Mater. Sci. Eng. 591, 012009, doi:10.1088/1757-899X/591/1/012009, 2019.

[18]. Pricop B., Mihalache E., Stoian G., Borza F., Özkal B., Bujoreanu L.-G., *Thermo-mechanical effects caused by martensite formation in powder metallurgy FeMnSiCrNi shape memory alloys*, Powder Met., 61(4), p. 348-356, doi: 10.1080/00325899.2018.1492773, 2018.

THE ANNALS OF "DUNAREA DE JOS" UNIVERSITY OF GALATI
FASCICLE IX. METALLURGY AND MATERIALS SCIENCE
Nº. 3 - 2021, ISSN 2668-4748; e-ISSN 2668-4756
Article DOI: https://doi.org/10.35219/mms.2021.3.02

A STUDY ON THE WEAR BEHAVIOUR OF MONOLITHIC MULLITE MATERIALS FOR DENTAL APPLICATIONS

Perent GÜLER[1], Burcu ERTUĞ[1], Nazenin İPEK IŞIKÇI[1], Alpagut KARA[2]

[1] Nişantaşı University, Faculty of Engineering and Architecture, Istanbul, Turkey,
[2] Eskişehir Technical University, Department of Materials Science and Engineering, Eskişehir, Turkey
e-mail: burcu.ertug@nisantasi.edu.tr

ABSTRACT

The aim of this study is to evaluate the potential use of the monolithic mullite samples for the dental applications. For this purpose, at first the monolithic mullite samples obtained by the powder metallurgy method have been characterized by the scanning electron microscopy (SEM) together with the EDS analysis. The pin-on-disk tribometer has been used to conduct the wear test in order to determine the volumetric loss. After the wear tests, the worn surfaces of the sintered mullite samples have been studied. The presence of the $3Al_2O_3.2SiO_2$ structure has been confirmed by the FT-IR spectroscopy through the observation of the characteristic Al-O-Si linkages at the spectra. The wear rate results derived from the volumetric losses have been measured to be around 2.42×10^{-6} mm^3/Nm. This value has been found to be lower than those of alumina and alumina-mullite composites in the previous studies, which explains the higher wear resistance of these mullite materials. The room temperature friction coefficients of AS-1 and AS-2 samples have been determined to be 0.88 and 0.80, respectively. The wear behaviour of the samples has been correlated to the sintering temperature and the resultant relative density of the samples. The mullite samples obtained in this study have indicated better wear performance than the other materials (alumina and alumina-mullite composites) in spite of the usage of monolithic material. Therefore, this study suggests that the monolithic mullite materials have a potential to be exploited for the replacement of the previous ceramic-based dental materials. Further studies might contribute to the improvement of these materials to be utilized in the oral environment.

KEYWORDS: wear, mullite, dental material, implant

1. Introduction

Dental crowns are typically made out of porcelain veneer and alumina core. A three-layer dental structure with porcelain-mullite-alumina was produced against the risk of fracture [1]. Mullite is still an attractive material for its optical properties, such as adequate transparency. Mullite products are conventionally-processed by a shape-forming step followed by the sintering. A solid-solid reaction or a transient liquid-phase reaction can produce the mullitization process through the interdiffusion of the present atoms. The mullitization is carried out around 1600 °C during solid-state reaction [2-4]. For load bearing dental implants, poor fracture toughness is a weakening property which is the driving factor for the improvement of the dental ceramics [5, 6].

High-purity precursors are not preferred for the production of mullite ceramics for the dentistry applications due to their high costs. Instead, abundant raw materials of alumina and silica are subjected to reaction sintering to produce mullite samples with satisfactory mechanical properties at a low cost [7]. Mullite is among the oxides used for advanced ceramics with variety of optical, thermal and mechanical (strength, toughness etc) properties [8]. Besides, it exhibits some attractive properties for the field of dental implants such as thermal expansion coefficient, environmental durability.

The densification of mullite and alumina was accomplished using the additives such as La_2O_3, B_2O_3

THE ANNALS OF "DUNAREA DE JOS" UNIVERSITY OF GALATI
FASCICLE IX. METALLURGY AND MATERIALS SCIENCE
N°. 3 - 2021, ISSN 2668-4748; e-ISSN 2668-4756
Article DOI: https://doi.org/10.35219/mms.2021.3.02

and the final mechanical properties were improved. Also, with the addition of Y_2O_3, a full density was achieved together with mullitization [9-13]. A number of these methods have a potential to produce denser dental implants that might exhibit better mechanical performance. In addition, by studying the wear properties of the dental ceramics, a better understanding of the interacting surfaces might be facilitated in the oral environment [14].

In this study, single-stage sintering has been applied to produce dense mullite ceramics. The microstructures, and the wear properties of mullite-based dental materials have been investigated.

2. Materials and methods

In the present study, the mullite samples $3Al_2O_3.2SiO_2$ have been prepared in a stoichiometric ratio. The sample preparation has been done by powder metallurgy using the raw powders of SiO_2 and Al_2O_3 after the milling in a planetary ball mill [15] for 1-3 hours, the calcined powder has been compressed to obtain the disc samples. Then, the samples have been sintered at 1670 °C and 1700 °C for a dwell time of 180 min as described in detail in our previous study [16].

Fourier Transform Infrared Spectroscopy (ATR-FTIR) analysis (Perkin-Elmer) has been carried out at ambient temperature in the spectrum range of 4000-400 cm^{-1} for the qualitative analysis on the chemical bonding. Au-Pd coating unit has been utilized prior to the microstructural characterization by means of SEM (Scanning Electron Microscope), using Jeol-JSM-6060 equipped with Energy Dispersive Spectrometer (EDS).

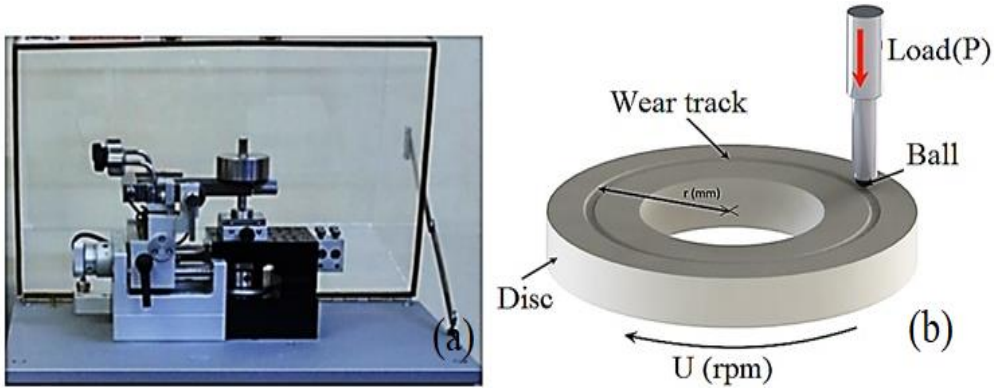

Fig. 1. *(a) Tribometer set-up and (b) design of pin-on-disk test according to ASTM-G99* [17]

The wear tests have been carried out using the tribometer set-up in Figure 1(a) (CSM Instruments). The tribometer is a pin-on-disk type set-up which applies a load of 10 N at a speed of 0.15 m/s. The test distance was 200 m and the wear test was conducted against Al_2O_3 balls as the counterpart under unlubricated wear conditions. The volumetric wear loss values for the samples AS-1 and AS-2 have been determined in cubic millimetres. After the wear test, the wear rates of the mullite samples have been calculated by Eq.1 as described in [18, 19].

$$W_{V\,(disc)} = V_{disc} / F_N . L \qquad (1)$$

where W_V is the disc wear rate (mm^3 /Nm), V_{disc} is the wear volume (mm^3), F_N-load (N), L sliding distance (m).

3. Results

According to FTIR results, as the sintering temperature changed from 1670 °C to 1700 °C, the intensities of the FTIR bands increased. Mullite is a structure of parallel chains where edge-sharing MO_6 octahedra is cross-linked with TO_4 tetrahedra [8] and at the spectra in Fig. 2 and Fig. 3, the wide bands at 3448 cm^{-1} and at 3450 cm^{-1} can be associated with the stretch vibration of OH for AS-1 and AS-2, respectively similar to those of the silicates. The stretch vibration of OH in Si-OH groups has also been observed at 3748 cm^{-1}. The bands observed at around 1150 cm^{-1} in Fig. 2 and Fig. 3 might be related to vibrational mode of asymmetric stretching of Si-O-Si and the peaks at 1137 cm^{-1} and 1140 cm^{-1} in any of the graphs which might be related to SiO_4.

Since 3/2-mullite with its formula $Al_2(Al_{2+2x}Si_{2-2x})O_{10-x}$ is an orthorhombic aluminosilicate (where x is 0.25) [8], the peaks observed at 755 cm^{-1} and 750 cm^{-1} are attributed to (Si,Al)-O-(Si,Al) bending mode for AS-1 and AS-2 samples, respectively in the mullite structure. The deformation vibration of the adsorbed water has been observed at around 1600 cm^{-1} [20].

Mullite microstructures have been given in Fig. 4 with the relevant EDS analysis results. EDS results

THE ANNALS OF "DUNAREA DE JOS" UNIVERSITY OF GALATI
FASCICLE IX. METALLURGY AND MATERIALS SCIENCE
N°. 3 - 2021, ISSN 2668-4748; e-ISSN 2668-4756
Article DOI: https://doi.org/10.35219/mms.2021.3.02

have indicated that the compositions are close to the mullite solid solution in the binary phase diagram. Also, the relative sintered densities have been measured to be 86-98% and the equiaxed grain morphology has been observed with grain size values of 2.5-4 μm in our previous study [16].

For AS-1 sample, the wear rate has been measured to be 2.42×10^{-6} mm^3/Nm as it can be seen in Fig. 5. For comparison, the wear rate of alumina was determined to be 6.76×10^{-5}-1.66×10^{-4} mm^3/Nm whereas that of alumina and mullite binary composites were 4.6×10^{-5}-1.3×10^{-4} mm^3/Nm. The friction coefficient of alumina and mullite binary composites were found to be lower, which results in a higher wear resistance of these composites with the co-working of both fracture and plastic wear mechanisms [21].

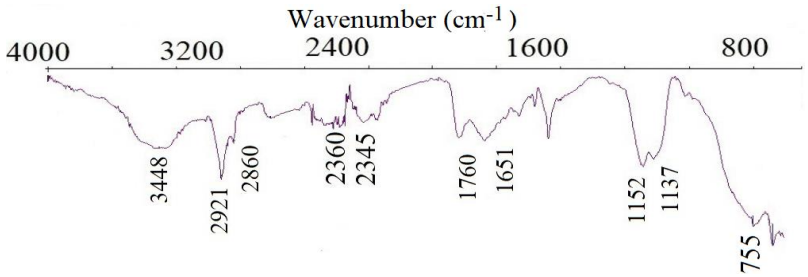

Fig. 2. *FTIR spectrum of AS-1 within 800-4000 cm^{-1} after heat treating*

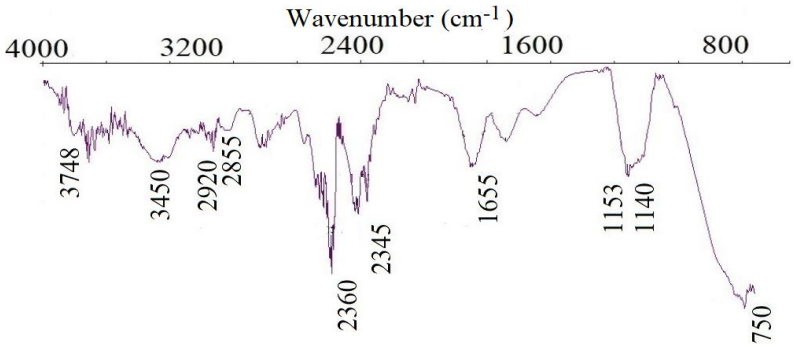

Fig. 3 *FTIR spectrum of AS-2 within 800-4000 cm^{-1} after heat treating*

The friction coefficients of AS-1 and AS-2 samples have been measured to be 0.88 and 0.80, respectively. For some of the different mullite compositions, friction coefficients were found to be 0.75-0.9 [22]. A number of researchers investigated the wear behavior of the mullite-based materials using various temperatures [23]. The room temperature friction coefficient was measured to be 0.75-0.90, rising up to 1.0 with the temperature. The wear rate values were found to be $7x10^{-4}$ mm^3/Nm and $3.5x10^{-5}$ mm^3/Nm for mullite and alumina materials, respectively [22].

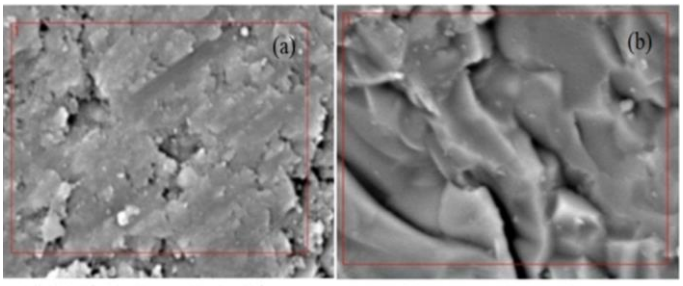

Component	Mole Conc.	Conc.		Component	Mole Conc.	Conc.	
Si	36.988	37.927	wt.%	Si	36.122	37.052	wt.%
Al	63.012	62.073	wt.%	Al	63.878	62.948	wt.%
	100.000	100.000	wt.%		100.000	100.000	wt.%

Fig. 4. *SEM-EDS analysis of (a) AS-1 and (b) AS-2*

THE ANNALS OF "DUNAREA DE JOS" UNIVERSITY OF GALATI
FASCICLE IX. METALLURGY AND MATERIALS SCIENCE
Nº. 3 - 2021, ISSN 2668-4748; e-ISSN 2668-4756
Article DOI: https://doi.org/10.35219/mms.2021.3.02

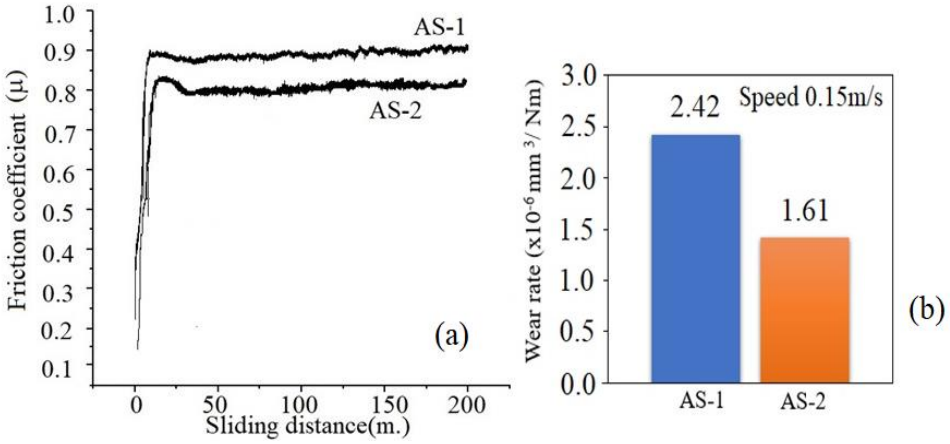

Fig. 5. *(a) Plot of friction coefficient vs. sliding distance and (b) wear rate values under 10 N for AS-1 and AS-2 against alumina*

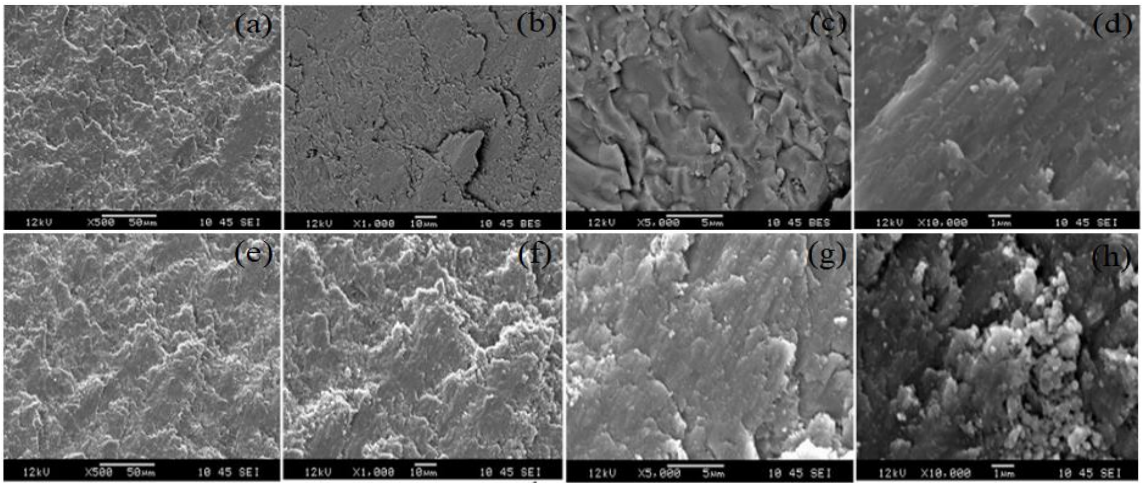

Fig. 6. *The worn surfaces after the wear test of the samples (a) AS-1 and (b) AS-2*

Following the wear test, worn surfaces of the two samples have been examined by SEM and the images have been given in Fig. 6. After the dry wear test of Al_2O_3-based materials, the repeated strips were observed on the worn surfaces perpendicular to sliding direction [24]. Also, the smooth regions were observed in the case of plastic deformation and the brittle fracture resulted in the pull-out of the material on the worn surface [18]. The wear rate values of the monolithic mullite samples have been found to be twenty-five times lower than the monolithic alumina materials and twenty times lower than alumina-mullite composites, showing a higher wear resistance.

The mullite phase peak intensity in the XRD pattern rises with the sintering temperature as a result of densification and the full mullitization [16]. This high wear resistance has been found to be related to the higher hardness and the densification of 98% due to sintering at 1700 °C. In addition, the uniform crystalline microstructure as described in [25] in these monolithic mullite samples has resulted in a high wear resistance.

4. Conclusions

This work presents the wear behavior of the monolithic mullite-based dental materials depending on the sintering temperature. FT-IR analysis observations have showed the characteristic Al-O-Si linkages confirming the presence of $3Al_2O_3.2SiO_2$ structure. Under test load of 10 N, the sintering at 1700 °C has yielded a higher friction coefficient. The increase in the sintering temperature has resulted in denser mullite samples and in the improvement of the relevant wear behavior. The wear rate values of the sintered dental materials have been measured to be twenty or twenty-five times lower by comparing the results of the previously-known materials from the literature, indicating a better wear performance. This high wear resistance might be explained by higher

densification, uniform crystalline microstructure and hardness. Further studies regarding the chemical durability tests of these materials might contribute to our knowledge on their behavior in the oral environment.

Acknowledgments

The authors are grateful to Metallurgical Engineer Haluk Gürses who provided the expertise for the microstructural analysis, FTIR spectroscopy and wear tests from Dokuz Eylul University, Industrial Services, Buca, Izmir.

References

[1]. Jang H. J., Park D. H., Jung Y. G., Lee H., *Microstructural design and evaluation of porcelain/mullite/alumina layered structure for dental application*, MRS OPL, 820, 2004.
[2]. Souto P. M., Menezes R. R., Kiminami R., *Sintering of commercial mullite powder: Effect of MgO dopant*, J Mater Process Tech, 209 (1), p. 548-553, 2009.
[3]. Viswabaskaran V., Gnanam F. D., Balasubramanian M., *Mullitisation behaviour of South Indian clays*, Ceram. Int., 28(5), p. 557-564, 2002.
[4]. Dong Y., Feng X., Ding Y., Liu X., Meng G., *Preparation of low-cost mullite ceramics from natural bauxite and industrial waste fly ash*, J Alloy Compd, 460(1), p. 599-606, 2008.
[5]. Lakshmi R., Sasikumar S., *Influence of needle-like morphology on the bioactivity of nanocrystalline wollastonite-an in vitro study*, Int J Nanomed, 10, p. 129-136, 2015.
[6]. Shirazi F. S., Mehrali M., Oshkoura A. A., Metselaara H. S. C., Kadri N. A., Abu Osman N. A., *Mechanical and physical properties of calcium silicate/alumina composite for biomedical engineering applications*, J Mech Behav Biomed, 30, p. 168-175, 2014.
[7]. Tripathi H. S., Ghosh A., Halder M. K., Mukherjee B., Maiti H. S., *Microstructure and properties of sintered mullite developed from Indian bauxite*, B Mater Sci, 35(4), p. 639-643, 2012.
[8]. Schneider H., Fischer R. X., Schreuer J., *Mullite: Crystal structure and related properties*, J Am Ceram Soc., 98(10), p. 2948-2967, 2015.
[9]. Fathi H. M., Johnson A., *The effect of TiO_2 concentration on properties of apatite-mullite glass-ceramics for dental use*, Dent. Mater., 32(2), p. 311-322, 2016.
[10]. Rahimi S., SharifianJazi F., Esmaeilkhanian A., Moradi M., Samghabadi A. H., *Effect of SiO_2 content on Y-TZP/Al_2O_3 ceramic-nanocomposite properties as potential dental applications*, Ceram. Int., 46(8), Part A, p. 10910-10916, 2020.
[11]. Cestari A., *Sol-gel methods for synthesis of aluminosilicates for dental applications*, J Dent., 55, p. 105-113, 2016.
[12]. She J., Mechnich P., Schmücker M., Schneider H., *Low-temperature reaction-sintering of mullite ceramics with an YO Addition*, Ceram. Int., 27(8), p. 847-852, 2001.
[13]. Mollazadeh S., Javadpour J., Eftekhari Yekta B., Jafarzadeh T. S., Youssefi A., *Synthesis and characterisation of dental composite materials reinforced with fluoroapatite-mullite glass-ceramic particles*, Adv Appl Ceram, 112(5), p. 294-300, 2013.
[14]. Basu B., Kalin M., *Tribology of ceramics and composites: A materials science perspective*, John Wiley & Sons, 2011.
[15]. ***, MTI Corporation, https://www.mtixtl.com/MSK-SFM-1-3.aspx.
[16]. Şahin M., Güler P., Güzel K., Ertuğ B., Kara A., *Influence of the mechanical alloying duration on the sintering of mullite ceramics*, IMSTEC18, Nevsehir, September 17-19, 2018.
[17]. Miramontes J. C., Tiburcio C. G., Tellez A. V., Salas C. P., Calderón F. A., *Wear resistance of thermal spray WC-Co-VC nanostructured coatings*, Advances in Tribology, IntechOpen, Croatia, p. 51-65, 2016.
[18]. Zhang F. C., Luo H. H., Wang T. S., Roberts S. G., Todd R. I., *Influence factors on wear resistance of two alumina matrix composites*, Wear, 265(1-2), p. 27-33, 2008.
[19]. Sulima I., *Tribological properties of steel/TiB_2 composites prepared by spark plasma sintering*, Arch Metall Mater, 59(4), p. 1263-1268, 2014.
[20]. Gören R., Ersoy B., Ozgur C., Alp T., *Colloidal stability-slip casting behavior relationship in slurry of mullite synthesized by the USP method*, Ceram. Int., 38, p. 679-685, 2012.
[21]. Luo H. H., Zhang F. C., Roberts S. G., *Wear resistance of reaction sintered alumina/mullite composites*, Mater Sci Eng, 478(1-2), p. 270-275, 2008.
[22]. Schneider H., Komarneni S., *Mullite*, John Wiley & Sons, 2005.
[23]. Nishikawa T., Kawabe K., Takatsu M., Kamiya H., *Sliding wear properties of sintered mullite ceramics*, J Ceram Soc Jpn, 100(1163), p. 912-917, 1992.
[24]. Taktak S., Baspinar M. S., *Wear and friction behaviour of alumina/mullite composite by sol-gel infiltration technique*, Mater Design, 26(5), p. 459-464, 2005.
[25]. Medvedovski E., *Alumina-mullite ceramics for structural applications*, Ceram. Int., 32(4), p. 369-375, 2006.

THE ANNALS OF "DUNAREA DE JOS" UNIVERSITY OF GALATI
FASCICLE IX. METALLURGY AND MATERIALS SCIENCE
N°. 3 - 2021, ISSN 2668-4748; e-ISSN 2668-4756
Article DOI: https://doi.org/10.35219/mms.2021.3.03

STUDIES AND RESEARCH ON THE INFLUENCE OF DEPOSIT PARAMETERS ON THE CHARACTERISTICS OF COMPOSITE COATINGS Ni-Al_2O_3 OBTAINED BY ELECTROCHEMICAL METHODS

Simona BOICIUC
"Dunarea de Jos" University of Galati, Romania
e-mail: simonaboiciuc@yahoo.com

ABSTRACT

The paper presents the characterization of composite coatings with nickel matrix using as dispersed phases Al_2O_3 particles, both from the microstructural point of view and from the point of view of the layer thickness, micro-hardness and corrosion behavior in saline fog. The presence of dispersed phase particles led to the finishing of the structure because they acted as nucleus centres, reducing the size of nickel crystallites. The parameters of the deposits influence the structure and properties of the obtained layers.

KEYWORDS: Ni composite coatings, electro-depositing, Al_2O_3, corrosion in saline fog

1. Introduction

Electrodeposition of a metal in a solution containing dispersed particles (Al_2O_3, ZrO_2, TiO_2, SiO_2 SiC, Si_3N_4, WC) leads to their incorporation in the metal matrix with the formation of composite coatings that sum up both the properties of the metal and those of the dispersed particles.

The composite layers thus obtained have special properties such as improved corrosion resistance, increased hardness, wear resistance, good adhesion of subsequent paint layers and longer life [1, 2].

The superior properties are due to the dispersed phase which is an obstacle to the displacement. It must have optimal shapes, sizes, distributions and quantities, correlated with the electrodeposition parameters, it must also have low solubility in the matrix material and it should not lead to chemical reactions with the matrix.

The co-deposition of the dispersed particles in the metal matrix, simultaneously with the electrodeposition of the metal is performed in the following stages:

- After the introduction of the dispersed phase particles in the electrolyte, a diffuse electric double layer of adsorbed ionic species (ionic cloud) is formed around them;
- The particles are transported to the limit of the hydrodynamic layer due to the agitation of the electrolyte;
- Under the influence of the electric field the positively charged particles diffuse towards the cathode surface, and those that have not been adsorbed on the surface, predominantly negative ions, will be rejected towards the solution volume;
- At the cathode there is a reduction of free or adsorbed electroactive ion species on particles;
- As a result of the reduction of ionic species adsorbed on particles, the incorporation of particles in the metal matrix takes place [3].

The properties of alumina are: high thermal conductivity, hardness, high melting point, high chemical resistance (it is attacked only by molten hydroxides and alkaline bisulphates and phosphoric acid) and electrical resistivity [4].

In this paper, the metallographic analysis and the corrosion resistance on composite coatings in nickel matrix using as dispersed phase technical alumina with dimensions of around 5 µm, have been achieved.

2. Experimental conditions

To obtain nickel and nickel matrix composite coatings, an electrochemical cell with a volume of 300 mL was used.

Watts electrolytes have been also used [5], temperature 50 °C, pH = 4, current density of 3 and 6 A/dm^2, dispersed phase concentration of 10 and 30

THE ANNALS OF "DUNAREA DE JOS" UNIVERSITY OF GALATI
FASCICLE IX. METALLURGY AND MATERIALS SCIENCE
Nº. 3 - 2021, ISSN 2668-4748; e-ISSN 2668-4756
Article DOI: https://doi.org/10.35219/mms.2021.3.03

g/L, stirring speed of 500 rpm, deposition time of 60 minutes.

The anode (99% nickel) was positioned at a distance of 14 mm from the cathode (being made of copper strip, with dimensions 20 x 40 x 10 mm).

The copper cathode was prepared by organic degreasing (trichloroethylene), stripping (HNO_3 + HCl) followed by washing with distilled water.

The microstructural characterization of the samples was performed on a Neophot 2 microscope.

To determine the micro-hardness, the PMT-3 micro-hardness hardness tester was used with a load of 50 g.

The corrosion behavior in the salt mist of the composite layers was performed according to SR EN ISO 9227:2017 for a period of 96 hours.

3. Experimental results

Metallographic analysis of pure nickel deposits, Fig. 1 showed that the deposited layers are homogeneous, uniform, adherent to the substrate and do not show cracks. It was found that, as the current density increases from 3 A/dm^2 for sample P1 to 6 A/dm^{2,} for sample P2, the thickness of the deposited layer increases from 0.0331 mm to 0.06 mm. The increase of the current density determines the formation of finer grains due to the additional activation of the inactive areas on the cathode.

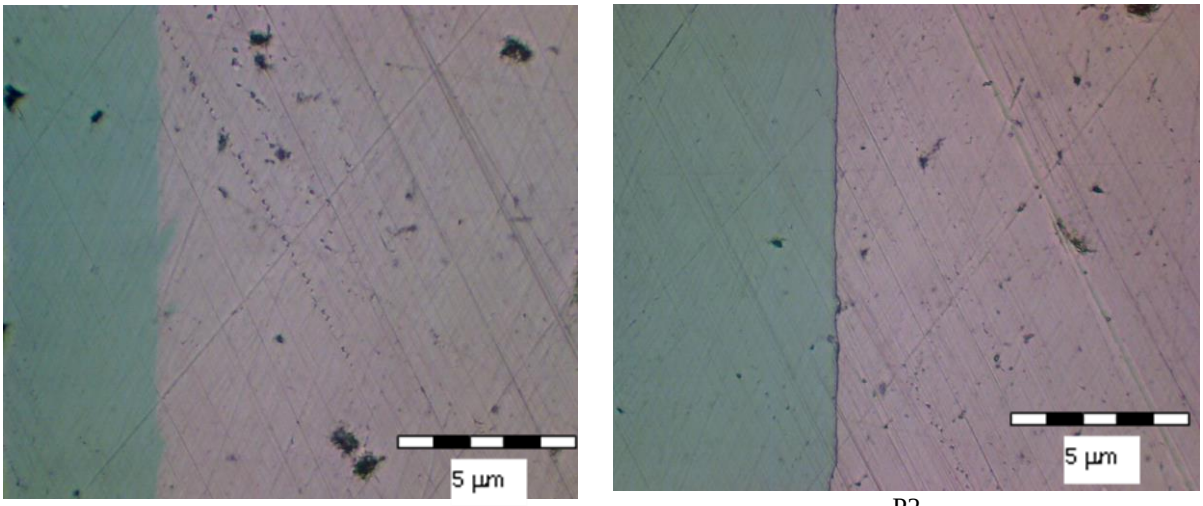

P1 P2

Fig. 1. *Microstructure of pure nickel layers obtained at current densities of 3 A/dm^2 - P1 and 6 A/mm^2 - P2*

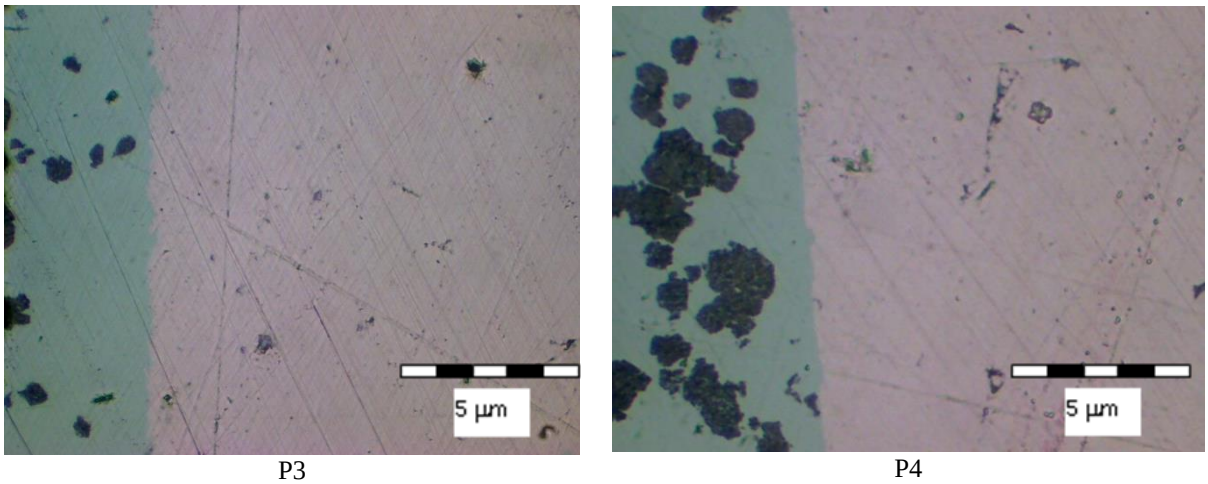

P3 P4

Fig. 2. *Microstructure of composite coatings obtained at a current density of 3 A/dm^2 and dispersed phase concentrations of 10 g/L - P3 and 30 g/L - P4*

THE ANNALS OF "DUNAREA DE JOS" UNIVERSITY OF GALATI
FASCICLE IX. METALLURGY AND MATERIALS SCIENCE
N°. 3 - 2021, ISSN 2668-4748; e-ISSN 2668-4756
Article DOI: https://doi.org/10.35219/mms.2021.3.03

As for the microhardness of the deposited nickel layers, it increases from 257.2 daN/mm^2 for sample P1 to 360 daN/mm^2 for sample P2, being greater than the microhardness of the substrate which was 104.4 daN/mm^2.

Metallographic analysis of composite coatings performed at current density of 3A/dm^2, Fig. 2 highlighted the fact that with the increase of the dispersed phase concentration in the electrolyte from 10 g/L to 30 g/L there is an increase of the percentage of phase included in the deposited layer. There is also an increase in the micro-hardness of the layers deposited from 435.3 daN/mm^2 for a dispersed electrolyte phase concentration of 10 g/L for sample P3 at 495.3 daN/mm^2 for a concentration of 30 g/L, to sample P4. The increase in hardness is due to the combined effect of particle dispersion, finer grain size compared to pure nickel deposits and increased deformation resistance due to limited displacement (by dispersed particles), reduced mobility and accumulation at the grain boundary.

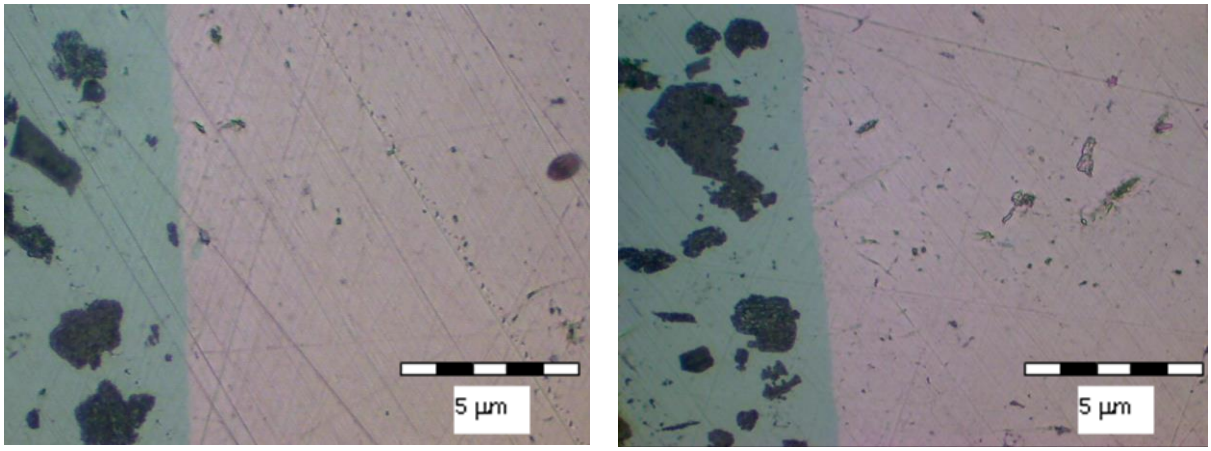

P5 P6

Fig. 3. *Microstructure of composite coatings obtained at a current density of 6 A/dm^2 and dispersed phase concentrations of 10 g/L - P5 and 30 g/L - P6*

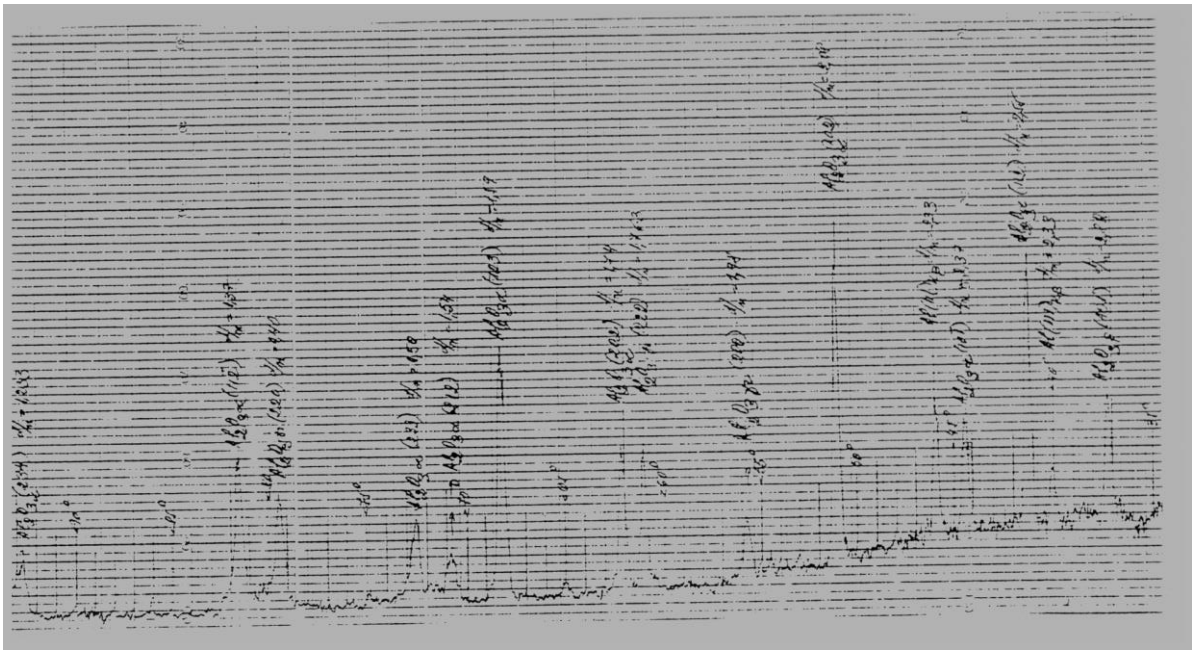

Fig. 4. *The diffractometric analysis of the dispersed phase particles*

There is also an increase in layer thickness from 0.0417 mm to 0.0531 mm.

When increasing the current density at 6 A/mm^2 it is found that the percentage of phase included in the

THE ANNALS OF "DUNAREA DE JOS" UNIVERSITY OF GALATI
FASCICLE IX. METALLURGY AND MATERIALS SCIENCE
Nº. 3 - 2021, ISSN 2668-4748; e-ISSN 2668-4756
Article DOI: https://doi.org/10.35219/mms.2021.3.03

metal matrix decreases. This is due to the activation phenomenon of the reduction of unabsorbed metal ions on the particles caused by the increase of the current density. The flux of metal ions in the diffusion layer towards the cathode surface increases with increasing current density, and that of oxide particles with adsorbed ionic species decreases, due to their lower mobility.

Regarding the evolution of the micro-hardness of the composite coatings obtained at current densities of 6 A/dm^2 it can be mentioned that values of 398.4 daN/mm^2 for a dispersed phase concentration of 10 g/L and of 414.5 daN/mm^2 for concentrations of 30 g/L have been obtained / have been achieved.

Layer thicknesses have values of 0.0741 mm for the layers obtained with a concentration of 10 g/L of the desperate phase and of 0.0798 mm for a concentration of the dispersed phase of 30 g/L.

Figure 4 presents the diffractometric analysis of the dispersed phase particles.

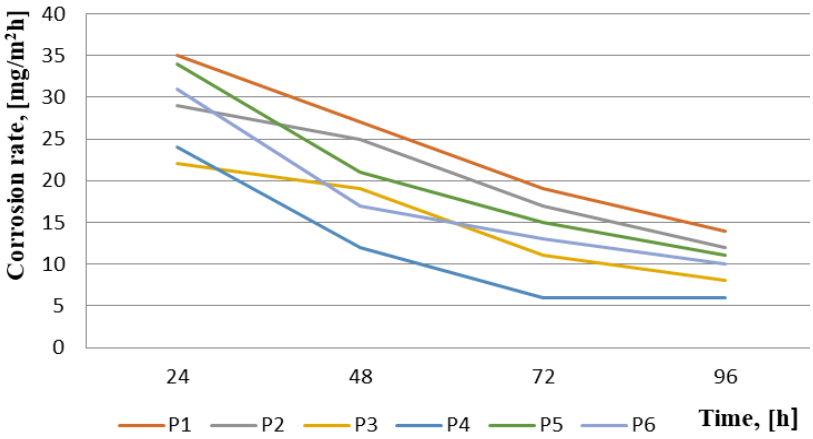

Fig. 5. *Corrosion behavior of nickel coatings and composite coatings obtained*

It was found that the composite coatings show a better corrosion behavior in accelerated corrosion test performed in saline fog compared to the pure nickel coatings, as it can be seen in Fig. 5. Dispersed phase particles of Al_2O_3 act as a barrier against the initiation and development of corrosion. A spot corrosion was observed around the imperfections from the growth of the film, or around the inclusions from the electrolyte bath, or around the pores. It is found that the corrosion resistance of composite coatings obtained at current densities of 3 A/dm^2 is superior to the corrosion resistance of coatings obtained at 6 A/dm^2.

4. Conclusions

Following the experimental research performed, the following conclusions can be mentioned:

- Nickel coatings obtained at different current densities do not have cracks, they are homogeneous and they have a good adhesion to copper supports;
- As the current density increases, the thickness of the deposited nickel layers increases from 0.0331 mm to 0.06 mm;
- The micro-hardness of the deposited nickel layers, increases from 257.2 daN/mm^2 for sample P1 to 360 daN/mm^2 for sample P2, being greater than the micro-hardness of the substrate which was 104.4 daN/mm^2;
- Electrochemically obtained composite coatings in nickel matrix using as dispersed phases particles of Al_2O_3 are homogeneous and they have no cracks; the increase in current density causes the formation of finer structures due to the multiplication of crystallization germs on the cathode compared to pure nickel deposits;
- At a current density of 3 A/dm^2 there is an increase in the micro-hardness of the deposited composite layers from 435.3 daN/mm^2 for a dispersed phase concentration of the electrolyte 10 g/L for sample P3 to 495.3 daN/mm^2 for a concentration of 30 g/L in the sample P4; there is also an increase in layer thickness from 0.0417 mm to 0.0531 mm;
- When increasing the current density at 6 A/mm^2 it is found that the percentage of phase included in the metal matrix decreases.
- Micro-hardness of composite coatings obtained at current densities of 6 A/dm^2 is of 398.4 daN/mm^2 for a dispersed phase concentration of 10 g/L and of 414.5 daN/mm^2 for concentrations of 30 g/L.
- The layer thicknesses have values of 0.0741 mm for the layers obtained with a concentration of 10 g/L dispersed phase and of 0.0798 mm for a concentration of the dispersed phase of 30 g/L.
- Composite coatings have a better corrosion behavior compared to pure nickel coatings, due to their passivation.

THE ANNALS OF "DUNAREA DE JOS" UNIVERSITY OF GALATI
FASCICLE IX. METALLURGY AND MATERIALS SCIENCE
Nº. 3 - 2021, ISSN 2668-4748; e-ISSN 2668-4756
Article DOI: https://doi.org/10.35219/mms.2021.3.03

References

[1]. Zamblau I., Popescu I. C., Varvara S., Mureşan L. M., *Corrosion of nanocomposite Cu-SiO_2 deposits obtained by electrodeposition in the presence of surfactants*, Anticorrosive Protection, vol. IV, 2009.

[2]. Zamblau I., Popescu I. C., Varvara S., Mureşan L. M., *Composite coatings with improved anticorrosive properties by co-electrodeposition of copper with Al_2O_3 nanoparticles*, Anticorrosive Protection, 2008.

[3]. Benea L., *Obtaining and structural analysis of protective films from composite materials*, PhD thesis summary, 1995.

[4]. Muşat V., *Advanced ceramics*, Technical Publishing House, Bucharest.

[5]. Boiciuc S., *Studies and research on the corrosion behavior of Ni-Al_2O_3 compound coatings obtained by electrochemical methods*, The Annals of "Dunarea de Jos" University of Galati, Fascicle IX. Metallurgy and Materials Science, no. 3, 2020.

THE ANNALS OF "DUNAREA DE JOS" UNIVERSITY OF GALATI
FASCICLE IX. METALLURGY AND MATERIALS SCIENCE
Nº. 3 - 2021, ISSN 2668-4748; e-ISSN 2668-4756
Article DOI: https://doi.org/10.35219/mms.2021.3.04

STUDIES AND RESEARCH ON OBTAINING MULTIFUNCTIONAL THIN FILMS BY MAGNETRON-ASSISTED PVD PROCESS

Simona BOICIUC
"Dunarea de Jos" University of Galati, Romania
e-mail: simonaboiciuc@yahoo.com

ABSTRACT

The paper aims to obtain thin films of nickel and zinc through the magnetron-assisted spraying process and their characterization from a structural point of view, of electrical, optical properties and corrosion resistance. It was found that as the intensity and discharge power increase, changes occur in the structure and properties of the deposited films.

KEYWORDS: thin films, d.c. magnetron, electrical and optical properties

1. Introduction

In addition to the basic function (electrical, optical, magnetic), the multifunctional coatings also have additional protection functions that ensure / increase their durability in operation.

Thin films are used for decorative - protective purposes, in electronic and optoelectronic applications, in the medical industry, as biocompatible films, in the field of mechanical parts manufacturing, to improve resistance to oxidation, corrosion, fatigue, wear, friction, to create thermal barriers and / or diffusion [1].

PVD deposition processes allow the deposition of films consisting of pure metals, oxides, nitrides, carbides whose structure can vary from porous to fibrous columnar, to compact columnar or with equiaxial grains (increasing the temperature favours recrystallization phenomena leading to polyhedral grains), depending on the submission parameters.

In the case of the magnetron-assisted PVD process, by superimposing a magnetic field parallel to the cathode surface, over the created electric field, the electrons are forced to remain for a longer time near the target, having helical trajectories. This creates a plasma with a high degree of ionization in front of the target, increases the spray rate and the deposition rate, and the pressure can be considerably reduced [1].

The deposition of pure metals by the magnetron-assisted PVD process can be performed to obtain reflective surfaces, contactor contact surfaces, for the protection of plastics, metals or glass or for decorative purposes.

Nickel deposits are used in many industries due to their resistance to atmospheric corrosion, water, alkaline solutions, salt solutions, weak organic acids, dry gases containing hydrochloric acid, hydrofluoric acid up to temperatures of 500 ºC. In the presence of nitric acid, sulfuric acid, hydrochloric acid, sulphur compounds, condensed water vapor or moisture, halogens corrode [2, 3].

The use of nickel deposits is also due to properties such as the melting temperature of 1455 ºC, density 8.9 g/cm^3, specific heat of 0.105 cal/g ºC, coefficient of linear expansion of 13.3 1/ºC, thermal conductivity of 0.22 cal/cm ºC, electrical conductivity at 20 ºC of 14.6 m/Ωmm^2, modulus of elasticity 19700 kgf/mm^2 [4].

Zinc deposits are used to improve the resistance to atmospheric corrosion, in the presence of moisture, natural waters, flue gases, contact with petroleum products or alkaline solutions of medium or low concentration. In tropical climates and in seawater it corrodes strongly [2, 3].

The use of zinc deposits is also due to properties such as the melting temperature of 419.5 ºC, density 7.1 g/cm^3, specific heat of 0.0915 cal/g ºC, coefficient of linear expansion of 29.8 1/ºC, thermal conductivity of 0.27 cal/cm ºC, electrical conductivity at 20 ºC of 16.9 m/Ωmm^2, modulus of elasticity 9400 kgf/mm^2 [4].

The paper aims to obtain thin films of nickel and zinc by the magnetron-assisted PVD process using glass plates as support and their characterization from a microstructural point of view, of electrical, optical properties and corrosion resistance.

2. Experimental conditions

To obtain the films, nickel and zinc plates of 99.9% purity, circular with a diameter of 46.5 mm and a thickness of 1 mm were used as targets.

A PVD spray deposition system was used [8], in a pressure range between $1 \cdot 10^{-3}$ - $8 \cdot 10^{-3}$ mbar.

THE ANNALS OF "DUNAREA DE JOS" UNIVERSITY OF GALATI
FASCICLE IX. METALLURGY AND MATERIALS SCIENCE
Nº. 3 - 2021, ISSN 2668-4748; e-ISSN 2668-4756
Article DOI: https://doi.org/10.35219/mms.2021.3.04

The deposits were made on glass plates, measuring 76 x 25 x 1 mm, which were subjected to ultrasonic degreasing with 50% ethyl alcohol at a temperature of 18-25 ºC, for 0.5-1 minute and then they were rinsed with distilled water for 1-2 minutes and dried.

Ultrasonic degreasing merges the combined degreasing effect of organic solvents with the mechanical effect of ultrasound. These, due to the cavitation phenomenon produced, cause high hydrostatic pressures that lead to the dislocation of fat particles from the samples.

A Neophot 2 optical microscope was used to performed microstructural analysis of the obtained films.

The electrical properties (resistivity), the transparency and the layer thickness of the films have been determined [8].

In the case of thin layers, the resistivity is calculated with the relation:

$$\rho = \frac{\pi \cdot t}{\ln 2}\left(\frac{U}{I}\right)$$

where: t - layer thickness, U - measured voltage, I - applied current.

$\frac{\rho}{t} = \frac{\pi}{\ln 2}\left(\frac{U}{I}\right)$ - represents the surface strength of the film.

Also, it was determined the corrosion behavior in the salt fog of the obtained films according to SR EN ISO 9227:2017 for a period of 96 hours.

The regimes used to obtain the films are presented in the Table 1.

Table 1. *The deposition regimes of Ni, Zn films*

Sample code / Material	Tension [V]	Current [mA]	Pressure [mbar]	Substrate temperature [°C]	Target - substrate distance [mm]	Deposition time [min]
P1/Ni	220	110	$1x10^{-3}$	45	60	20
P2/Ni	270	120	$5x10^{-3}$	55	60	20
P3/Ni	240	170	$5x10^{-3}$	70	60	20
P4/Zn	320	100	$6x10^{-3}$	53	60	20
P5/Zn	*350*	*120*	*$7x10^{-3}$*	*60*	*60*	*20*
P6/Zn	*360*	*150*	*$8x10^{-3}$*	*70*	*60*	*20*

3. Results and discussions

Following the microscopic analysis, it was observed that the obtained films are glossy, do not show cracks, are relatively homogeneous and adherent, as it can be seen in Fig. 1.

If the current is low, the spray power is low, which reduces the deposition rate. This is due to the lower energy of the argon atoms hitting the target. Thus, a nucleation and a reduced growth take place, which leads to obtaining thinner, non-uniform, discontinuous and inhomogeneous films as it can be seen in samples P1 and P4.

If the current intensity increases, the spray power increases, which leads to an increase in the deposition rate and the film thickness. The mobility of the pulverized atoms and the energy of the adsorbed atoms on the surface are improved, thus increasing the crystallinity of the film, as it can be seen in samples P3 and P6.

It has been found [5-7] that at higher deposition powers there is a Volmer-Weber's growth, respectively an island 3D growth (through the coalescence of nuclei with the formation of material islands). Thus, uniform, continuous, homogeneous films are obtained with the orientation of the grains perpendicular to the surface, which leads to the improvement of their properties.

Due to the increase of the discharge power, the temperature of the substrate increases which leads to the increase of the degree of crystallinity and of the grain size.

The results of the measurements of electrical resistance, transparency and layer thickness are presented in Tables 2 and 3.

THE ANNALS OF "DUNAREA DE JOS" UNIVERSITY OF GALATI
FASCICLE IX. METALLURGY AND MATERIALS SCIENCE
Nº. 3 - 2021, ISSN 2668-4748; e-ISSN 2668-4756
Article DOI: https://doi.org/10.35219/mms.2021.3.04

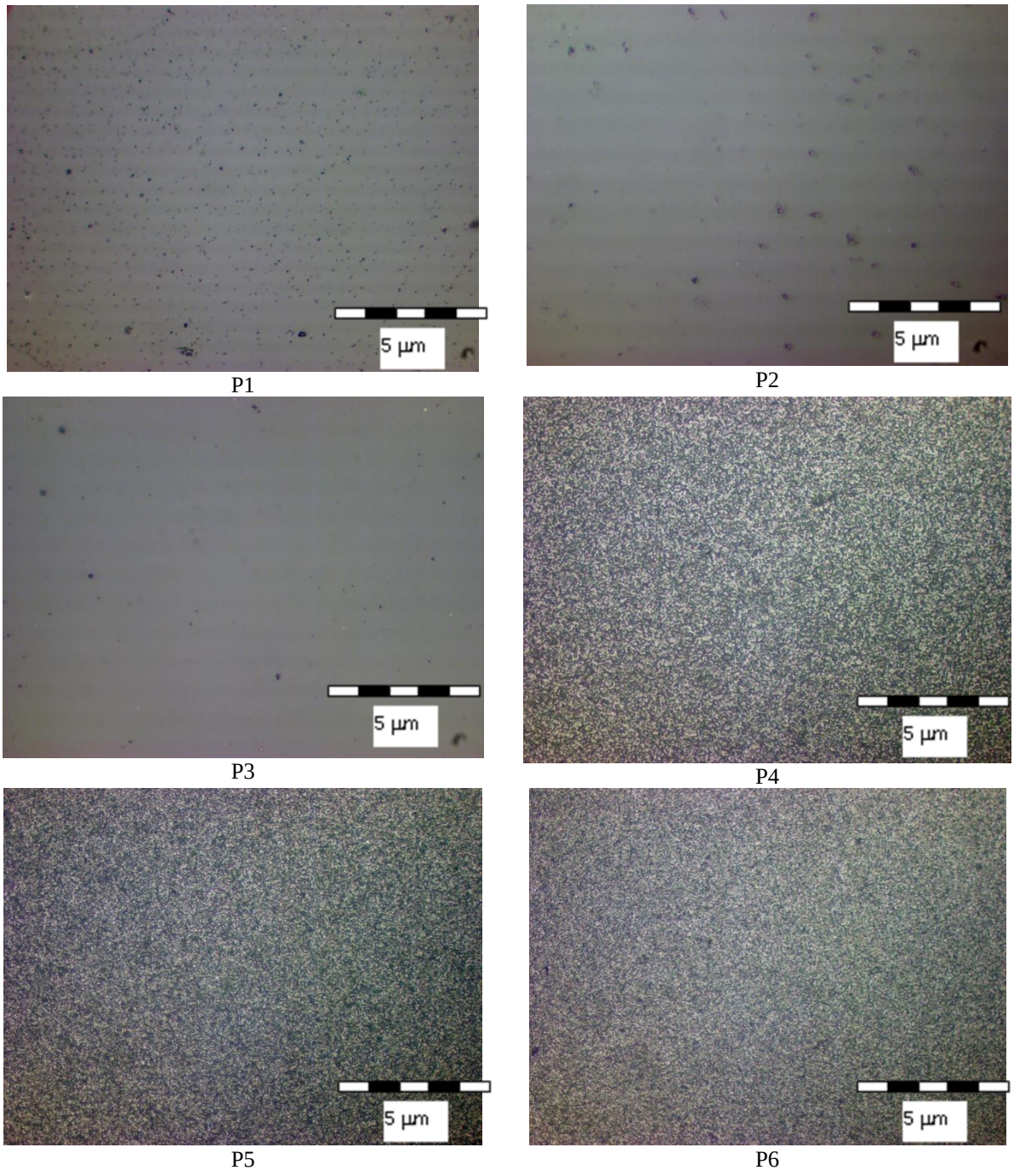

Fig. 1. *Micrographs of the deposited films*

Table 2. *Properties of nickel films*

Sample code	Film surface resistance Rs [Ω]	Films transparency	Thickness of films [nm]
P1	85.16	2	3.8
P2	64	0.85	5.5
P3	17.33	0.38	33

THE ANNALS OF "DUNAREA DE JOS" UNIVERSITY OF GALATI
FASCICLE IX. METALLURGY AND MATERIALS SCIENCE
Nº. 3 - 2021, ISSN 2668-4748; e-ISSN 2668-4756
Article DOI: https://doi.org/10.35219/mms.2021.3.04

Table 3. *Properties of zinc films*

Sample code	Film surface resistance Rs [MΩ]	Films transparency	Thickness of films [nm]
P4	12	2.25	4.6
P5	4.5	1.8	31.5
P6	2.8	1.2	38

Analysing Tables 2 and 3 it can be seen that at low current intensities the discharge power is low, the film thickness is reduced, and the surface resistance is higher. This is attributed to structural defects (dislocations, interstitial defects, vacancies), impurities (foreign atoms soluble in nickel, zinc), low density and crystallinity, due to the reduced mobility of adsorbed atoms. The presence of internal stresses (caused by the difference between the coefficients of thermal expansion between the film and the substrate) in the deposited film increases its susceptibility to oxidation. If the temperature developed during deposition is low, the value of these voltages is negligible.

As the current intensity increases, the discharge power increases, the film thickness increases and the surface resistance decreases. The decrease is due to the improved film density and increased grain size. The density of dislocations, the probability of defects occurring and the micro-tensions in the film decrease as its thickness increases.

The transparency of the films decreases as the current intensity increases, respectively as the spray power increases. This is due to the increase in film thickness.

The corrosion behavior in the salt mist was performed on the samples with the highest thickness. Analysing Figure 2, it can be seen that the nickel film has a higher corrosion resistance than the zinc film. Corrosion has been found in points that evolve over time, as surface passivation occurs.

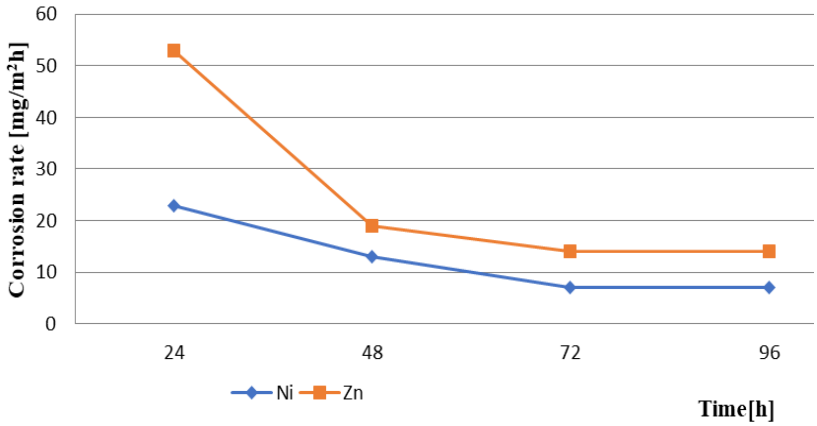

Fig. 2. *Corrosion behavior of deposited films*

4. Conclusions

The following conclusions can be drawn from the experiments performed:

- magnetron-assisted spraying is used in many fields, to obtain thin films and ensures a rigorous, advanced control over the composition and microstructure and implicitly over their properties;

- the obtained films are glossy, they do not show cracks, and they are even more homogeneous and adherent, the higher the current intensity, the higher the spray power; thus, increasing the film thickness from 3.8 to 33 nm for nickel deposits and from 4.6 to 38 nm for zinc deposits and grain size and improving the crystallinity;

- as the current intensity increases, the surface resistance decreases because the density of the film improves and the probability of structural defects, impurities and increase of micro-tensions is reduced; thus, it has values between 85.16 and 17.33 Ω for nickel deposits and between 12 and 2.8 Ω for zinc deposits;

- the transparency of the films is reduced with the increase of the spraying power and their thickness; it has values between 2 and 0.38 for nickel deposits and between 2.25 and 1.2 for zinc deposits;

THE ANNALS OF "DUNAREA DE JOS" UNIVERSITY OF GALATI
FASCICLE IX. METALLURGY AND MATERIALS SCIENCE
Nº. 3 - 2021, ISSN 2668-4748; e-ISSN 2668-4756
Article DOI: https://doi.org/10.35219/mms.2021.3.04

- the corrosion behavior in salt mist of nickel film is superior to zinc film.

References

[1]. Vermeşan G., *et al.*, *Introduction to surface engineering*, Dacia publishing house, Cluj-Napoca, 1999 (Introducere în ingineria suprafeţelor, editura Dacia, Cluj-Napoca, 1999).
[2]. Maria Constantinescu, *Corrosion protection of metals*, Technical Publishing House, Bucharest, 1979. (Protecţia anticorozivă a metalelor, Editura Tehnică, Bucureşti, 1979).
[3]. Marinescu A, Andonianţ Gh., *E Bay – Electrochemical and chemical technologies for the protection of metallic materials*, Bucharest Technical Publishing House, 1984 (Tehnologii electrochimice și chimice de protectie a materialelor metalice, Editura Tehnica București, 1984).
[4]. Schumann H., *Physical Metallurgy*, Technical Publishing House, 1962 (Metalurgie fizică, Editura tehnică, 1962).
[5]. Mech K., Kowalik R., Zabiński P., *Cu thin films deposited by dc magnetron sputtering for contact surfaces on electronic components*, Archives of Metallurgy and Materials, Issue 4, vol. 56, 2011.
[6]. Minh-Tung Le, Yong-Un Sohn, Jae-Won Lim, Good-Sun Choi, *Effect of Sputtering Power on the Nucleation and Growth of Cu Films Deposited by Magnetron Sputtering*, Materials Transactions, vol. 51, No. 1, p. 116-120, 2010.
[7]. Ali Gelali, Azin Ahmadpourian, Shahoo Valedbagi, Behroz Safibonab, Bandar Astinchap, Eisa Karimzadeh, *Structure and Morphology of the Cu Films Grown by DC Magnetron Sputtering*, J. Basic. Appl. Sci. Res., 3(6), p. 846-849, 2013.
[8]. Boiciuc S., *CuO films obtained by oxidation of cu layers deposited by the pvd process - magnetron sputtering*, The Annals of "Dunarea de Jos" University of Galati, Fascicle IX. Metallurgy and Materials Science, no. 3, 2020.

THE ANNALS OF "DUNAREA DE JOS" UNIVERSITY OF GALATI
FASCICLE IX. METALLURGY AND MATERIALS SCIENCE
Nº. 3 - 2021, ISSN 2668-4748; e-ISSN 2668-4756
Article DOI: https://doi.org/10.35219/mms.2021.3.05

THE CORRELATION BETWEEN THE OPERATING CONDITIONS OF AN OIL TANKER AND FUEL CONSUMPTION

Mariana LUPCHIAN
"Dunarea de Jos" University of Galati, Romania
e-mail: mariana.lupchian@ugal.ro

ABSTRACT

This paper presents a calculation method to determine optimum operating conditions of power plants installations with internal combustion engines used on ships. The scope of this document is to make a minimum fuel consumption calculation using software Engineering Equation Solver. Analysing several operating regimes, the specific consumption of heavy fuel used on the main engine of the oil tanker is calculated. Vessel must operate at the parameters for which it was designed and built, thus satisfying all technical and economic aspects.

KEYWORDS: fuel consumption, oil tanker, propeller, operating regimes, internal combustion engines

1. Introduction

The propulsion engines operating in different exploitation conditions was determined by the technical condition of the ship and the propulsion plant and external factors that have an influence on the operation [1, 5].

A power plant with internal combustion engine is a heat power plant mainly processing the chemical energy of the fuel used, and transformed into heat energy from combustion processes and mechanical work necessary for its consumers [2].

The main engine of a ship is the main fuel consumer and major energy manufacturer on board.

By introducing the technical state, as an independent variable, there must be taken into consideration the periods of time in which the fixing of the capital naval propulsion plant must be done, as well as the ship docking, in order to clean the careen etc., so the exploitation costs be minimum [3].

The fundamental purpose of the activities performed during the operation, maintenance of the propulsion installation and of the hull of the ship is the maintenance of the marching qualities during its entire service life.

When carrying out the propulsion of ships, in principle, two basic requirements are imposed: ensuring the prescribed speed of the ship and minimizing fuel consumption.

When choosing the number of engines and shaft line elements, the full load draft and the ballast ship draft are taken into account, determining the diameter, optimum speed, propeller efficiency and total engine power necessary to achieve the speed required by the design theme [1, 9].

2. Study on fuel consumption for several operating regimes

The paper is a continuation of a study on a 37000 tdw oil tanker. The studied oil tanker is equipped with a diesel engine MAN B & W & 6-cylinder, engine power: 9480 [KW], 127 [rpm].

The main mechanical characteristics of compression ignition engines at optimum thermal regimes are given by the following dependencies:

- Pe [kW] - effective engine power;
- n [rpm] - engine speed;
- h - position of the control system of the injection system [5].

The vessel must operate at the parameters for which it was designed and built, thus satisfying all technical and economic aspects [5, 7].

Fuel efficiency is reliant on several parameters of a vehicle, including engine parameters, aerodynamic, weight and rolling resistance.

In order to improve ship propulsion an installation is used for main marine diesel fuel with sulphur heavy fuel oil, that is especially hard to slow diesel engines and diesel engines semirapid ones [5, 6].

The selection of the type of propulsion system must be the result of a technical-economic analysis, which takes into account all the factors on which the

THE ANNALS OF "DUNAREA DE JOS" UNIVERSITY OF GALATI
FASCICLE IX. METALLURGY AND MATERIALS SCIENCE
N°. 3 - 2021, ISSN 2668-4748; e-ISSN 2668-4756
Article DOI: https://doi.org/10.35219/mms.2021.3.05

safety and economy ship is used. The vessel must operate at the parameters for which it was designed and built, satisfying all the competitiveness aspects, both technically and economically [4].

The resistance to progress is one of the most important qualities for navigation, which depends on the power of the propulsion system [3, 5, 8].

The J. Holtrop and G. G. J. Mennen methods have been used to determine the ship's forward resistance [10].

The advantage of this method is that it can be easily programmed in order to achieve an optimization program.

Ship resistance in advancement R (kN) is given by:

$$R = R_F(1+k_1) + R_{AP} + R_W + R_B + R_{TR} + R_A \quad (1)$$

where:

$1+k_1$ - form factor linking the viscosity resistance of the body in conjunction with abrasion resistance R_F [5, 9, 10]

R_{AP} - resistance apendincs;

R_W - wave resistance;

R_B - additional pressure density of the bulb near the water surface;

R_{TR} - density of the additional pressure of stern cut;

R_A -strength of the correlation model ship (correction of roughness).

The propulsion factors are calculated at several operating regimes, considering the ship loaded and ballasted.

Figure 1 shows Rt [kW] depending on the speed of the ship [Nd] (for the loaded and ballasted ship).

For several operating modes, it is calculated the power of the propulsion engine, the towing power, the power available at the propeller (P_{rem}, P_{el}, $P_{MP,m}$) [5].

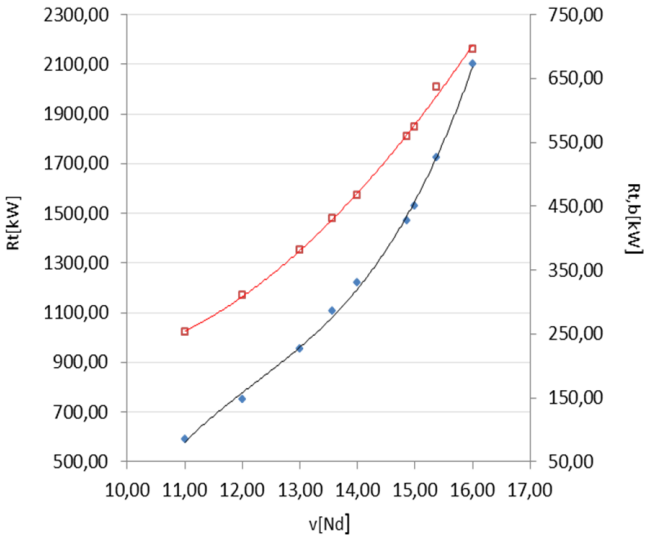

Fig. 1. *Resistance to the advancement of the ship*

Figure 2 shows R_t, P_{rem}, P_{el}, P_{MP} depending on the speed [Nd] for different operating modes.

The dependence of power of towing of the ship, the power required to drive the propeller, relies on the engine power propulsion and the resistance to progress of the ship (full load).

The actual specific fuel consumption was calculated according to the propeller characteristic (full load) for some of the analyzed operating modes.

The forward resistance of the ship R = f (Tj), the loaded ship has the draft Tj = 10.5 m.

The specific fuel consumption is determined according to the hourly fuel consumption and the effective power of the main engine.

Considering the ship defined as a subsystem of the operating system, through the main characteristics (capacity, speed, autonomy, etc.), there is the problem of establishing the form, energy and functional parameters that determine the optimal operating conditions for the given ship.

c_{s1} - the actual effective fuel consumption for the loaded ship;

THE ANNALS OF "DUNAREA DE JOS" UNIVERSITY OF GALATI
FASCICLE IX. METALLURGY AND MATERIALS SCIENCE
Nº. 3 - 2021, ISSN 2668-4748; e-ISSN 2668-4756
Article DOI: https://doi.org/10.35219/mms.2021.3.05

c_{s2} - the actual effective fuel consumption for the ballast ship;

Figure 3 shows the specific consumption of heavy fuel c_{s1}, c_{s2} for the analyzed operating regimes.

The main factor for the specific cost is the fuel consumption- which actually means the minim fuel consumption of the energetic plant with internal combustion engines, for which the optimum control proportions, which assure the optimal functioning regimes, must be found. [4]

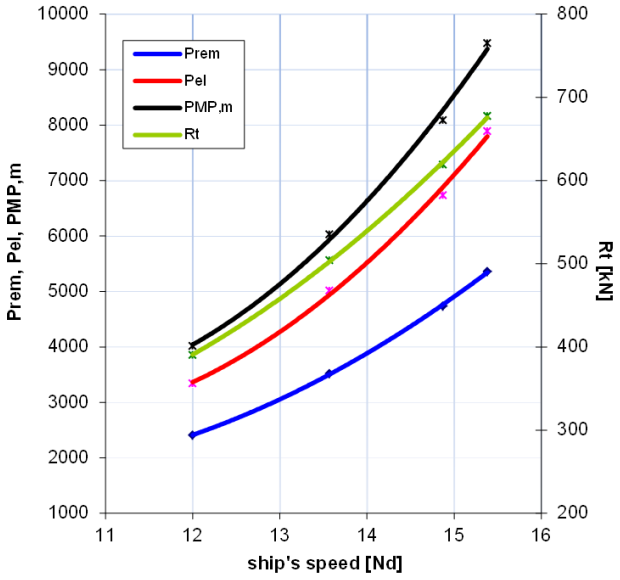

Fig. 2. *R_t, P_{rem}, P_{el}, P_{MP} - depending on the speed of the ship*

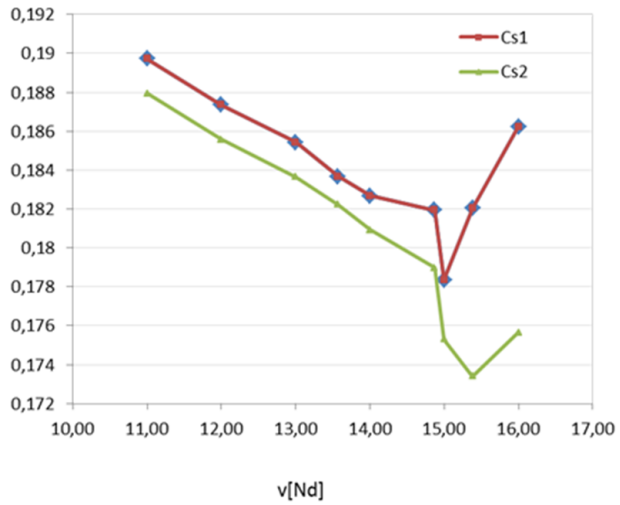

Fig. 3. *The specific effective consumption of fuel (loaded ship and ballasted)*

3. Obtained results

The energetic and functional parameters result from the analysis of the navigation regimes considered representative for the operation of the ship in the conditions imposed by the considered transport system.

Fuel consumption is the main factor that determines the specific cost, which is actually a minimum specific fuel consumption for minimum naval propulsion plant.

Fuel efficiency is reliant on several parameters of a vehicle, including engine parameters, aerodynamic, weight and rolling resistance.

In order to improve ship propulsion an installation is used for main marine diesel fuel with sulphur heavy fuel oil that is especially hard to slow diesel engines and diesel engines semirapid.

THE ANNALS OF "DUNAREA DE JOS" UNIVERSITY OF GALATI
FASCICLE IX. METALLURGY AND MATERIALS SCIENCE
Nº. 3 - 2021, ISSN 2668-4748; e-ISSN 2668-4756
Article DOI: https://doi.org/10.35219/mms.2021.3.05

The actual specific fuel consumption of the propulsion engine was determined by the propeller characteristic, for several operating and running modes; resulted in an optimum speed of 15 Nd for the loaded ship with a minimum specific consumption of 0.17835 kg/kWh and an optimal speed of 15.38 Nd for the ballasted ship with a minimum specific consumption of 0.1734 kg/kWh.

Figure 4 and 5 show the specific effective consumption of heavy fuel used by the propulsion engine of the oil tanker.

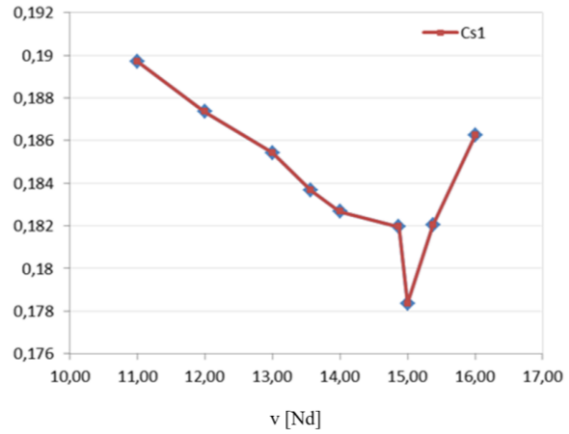

Fig. 4. *The specific effective consumption of fuel depending on ship speed [Nd] (loaded ship)*

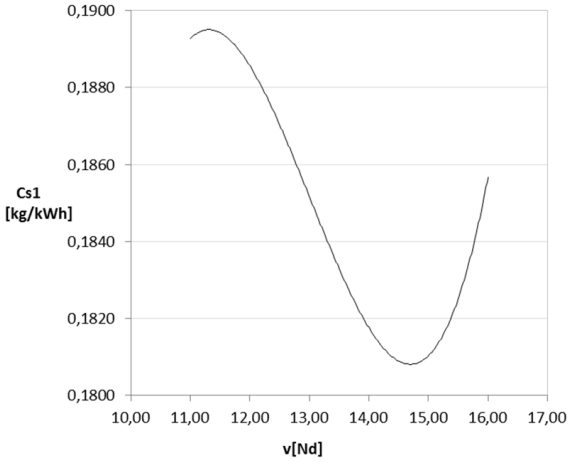

Fig. 5. *Minimum fuel consumption*

References

[1]. Simionov Mihai, *Instalații de mașini*, Galati University Press, Editura Universității "Dunărea de Jos" din Galați, 2018.
[2]. Lupchian Mariana, *The influence of propulsion factors on the functioning regimes of a naval power plant*, Constanta Maritime University Annals, vol. 21, Publisher: Constanta Maritime University, ISSN: 1582-3601, 2014.
[3]. Lupchian Mariana, *Analysis of the operating regimes of power plants for different situations naval navigation, SECTION I – Navigation and Maritime Transport*, Constanța Maritime University Annals, vol. 19, p 51, Editura Nautica, 2013.
[4]. Lupchian Mariana, *Determination of optimum operating regime for a naval power plant based on minimum fuel consumption*, ModTech International Conference - New face of TMCR, Modern Technologies, Quality and Innovation, New face of TMCR, 24-26 May, Sinaia, Romania, 2012.
[5]. Lupchian Mariana (Caraghiulea Mariana), *Contribuții la optimizarea regimurilor de funcționare ale instalațiilor energetice cu motoare cu ardere internă*, PhD thesis, Galati, 2012.
[6]. Simionov Mihai, *Instalații de propulsie navale. Linii de arbori navale*, Editura Evrika, Brăila, 2001.
[7]. ***, *The Motor Ship*, Waste management is a grey area for owners, 2001.
[8]. Simionov Mihai, *Instalații de propulsie navală*, Galati University Press, 2009.
[9]. Ceangă V., Mocanu C. I., Teodorescu C., *Dinamica sistemelor de propulsie*, Editura Didactică și Pedagogică, Bucuresti, 2003.
[10]. Bidoaie I., Sarbu N., Chirica I., Ionaș O., *Indrumar de proiectare pentru teoria navei*, p. 169-178, Universitatea Dunarea de Jos, Galati, 1986.

THE ANNALS OF "DUNAREA DE JOS" UNIVERSITY OF GALATI
FASCICLE IX. METALLURGY AND MATERIALS SCIENCE
N°. 3 - 2021, ISSN 2668-4748; e-ISSN 2668-4756
Article DOI: https://doi.org/10.35219/mms.2021.3.06

COPPER CORROSION IN ULTRASOUND CAVITATION FIELD

[1]Cristian Ștefan DUMITRIU, [2,*]Alina BĂRBULESCU
[1]SC Utilnavorep SA, Constanța, Romania,
[2]Transilvania University of Brașov, Faculty of Civil Engineering, Brașov, Romania
e-mail: *cris.dum.stef@gmail.com, alinadumitriu@unitbv.ro

ABSTRACT

This article contains the results of the experiments concerning the mass loss of copper in seawater, in the cavitation presence. The cavitation is produced by ultrasound in an experimental setup designed for this purpose. The models of mass loss are provided and validated by statistical methods. Gravimetric indices are computed, to compare the mass loss in different cases. Differences are noticed in the mass-loss trend at different power of the ultrasound generator.

KEYWORDS: cavitation, corrosion, mass loss, gravimetric index, mathematical model

1. Introduction

When ultrasound waves pass through a liquid, they exhibit a cyclic succession of expansion and compression phases imparted by mechanical vibrations [1]. During the compression periods, the waves produce a positive pressure that pushes together the liquid molecules. During the expansion periods, the ultrasound waves produce a negative pressure that pulls the molecules apart [2]. At a certain energy level, tiny bubbles (called cavitation bubbles) containing vapours or gases appear [3, 4]. This dynamical process of apparition, development, and collapse of some bubbles or cavities that contain vapours or gases in the liquid mass is called cavitation [5]. The results of these cycles are sonoluminescence, the apparition of oscillations with a frequency that is not the same as that of the ultrasonic field, emulsification and chemical reactions, destruction of parts of solid materials [6-9].

Systematic studies have evolved for many decennia giving different explanations for the damages produced on materials under the action of the cavitation field. Rayleigh [10] was among the first scientists giving them a mechanical explanation, while others considered that these damages were the result of many processes [11-13] of chemical and/or electrical nature [6, 8, 14-16]. Researches proved that plastic deformations appear everywhere in the presence of cavitation, leading to the idea that the chemical action cannot be the primary cause of the destructions produced by cavitation. It seems that the cavitation destructions are the results of the mechanical pressures from the inside of bubbles [5], and erosion is the effect of high-speed jets on the unstable surface of the cavitation bubbles [6].

It is known that various chemical reactions produced under the ultrasound action are related to the cavitation action. Chemical processes induced in the ultrasound field are produced only if the ultrasound intensity is big enough to assure the cavitation apparition and development. From this point of view, one can distinguish between two categories of chemical reactions: accelerated by cavitation and others, produced only simultaneous or after applying a cavitation field and under the action of some factors such as high temperature or high pressure [6]. The corrosion in saline water belongs to the first class.

This article presents the experimental results related to the mass loss of copper in seawater in cavitation field obtained using an experimental setup specially designed for this purpose. Models validated by statistical methods describe the mass loss trend, and gravimetric indices are provided to compare the mass loss at different powers of the generator.

2. Materials and methods

2.1. Experimental setup

The studied material is Cu, with 99.78% Cu, 0.0747% Zn, 0.0395% Fe, 0.0446% Sn. The composition of the seawater used for all the experiments is the following: salinity: 22.17 g/L NaCl, pH = 7, 6.27 meq/L - total water hardness, 0.051 mg/L Fe, 0.0033 mg/L Ni.

THE ANNALS OF "DUNAREA DE JOS" UNIVERSITY OF GALATI
FASCICLE IX. METALLURGY AND MATERIALS SCIENCE
Nº. 3 - 2021, ISSN 2668-4748; e-ISSN 2668-4756
Article DOI: https://doi.org/10.35219/mms.2021.3.06

The experimental setup used for studying the mass loss in the cavitation field is presented in Fig. 1 [6, 14, 15]. The ultrasound generator operates at 20 kHz and three power levels: 80 W, 120 W, and 180 W. Vessel A (the generator tank) contains a ceramic transducer, with 3.7 cm diameter, connected to the high-frequency generator that excites the transducer to produce the ultrasound. Vessel B contains electrodes of electrolytic copper that measure the potential difference appeared between different points at the cavitation zone boundaries.

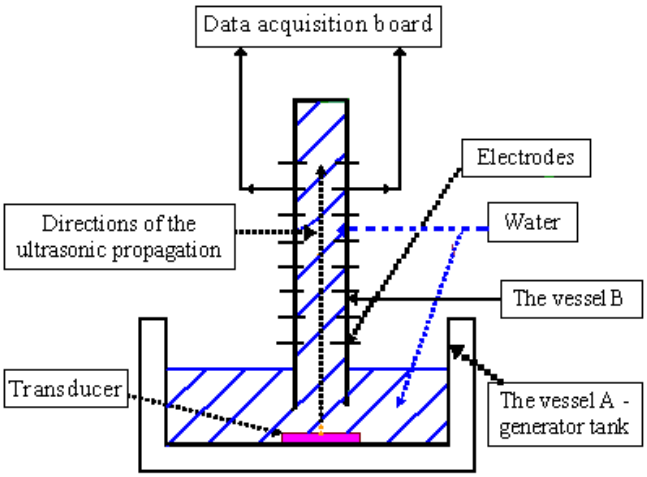

Fig. 1. *The experimental set up*

The data acquisition board can be connected to different electrodes. It converts analogical signals into a digital sequence and stores the signal in the on-board memory. The PC is then allowed to access the memory and retrieve the data for further processing.

The setup works in the following mode: the liquid is introduced in the bulk and the samples are positioned at the distance of 30 cm from the transducer. The ultrasound generator is switched on, at one of the power levels. If one wants to study the signal induced by the cavitation bubbles produced by the ultrasonic field, the computer and the software of data acquisition are also switched on. We don't discuss here the last aspect, treated in other work articles [6, 9, 17-22]. We focus on the mass loss of the four samples, in seawater in the presence of cavitation. The working temperature has been kept constant at 20 ºC.

The samples have been kept in saline water under cavitation produced by ultrasound for a total of 1320 minutes (380 minutes at 80 W, 480 minutes at 120 W, and 480 minutes at 180 W of the generator power) and weighted every 20 minutes. All data were put together and the model of the mass loss has been determined.

2.2. Statistical methods

The material mass loss and relative mass in the cavitation field have been modelled, and statistical methods have validated the models. The following statistical tests have been used to validate the regression models:

• The determination coefficients (R^2) and the residuals standard deviation (s) are reported. For a good model, R^2 should be close to 1 the standard deviation close to zero.

• The P-P plot and the Anderson-Darling test [23], to check the hypothesis that the residuals in the model are normally distributed.

P-P plot is used for assessing how closely the given data and the theoretical normal distribution are. If the distribution of the tested variable is normal, then the points P-P describe a line superposed with the straight line that represents the theoretical distribution.

In this study, the theoretical confidence intervals at a 95% confidence level are also provided.

The Anderson-Darling test has been performed at a 5% significance level. If the p-value associated is less than 0.05, the normality hypothesis cannot be rejected.

• Testing for the absence of the residuals' correlation by using the autocorrelation function. If the values of the autocorrelation function are inside the confidence interval at the confidence level of 95%, then the residuals are not correlated.

• To check the null hypothesis that the residuals are homoskedastic (they have the same variance), the Bartlett test is used [24] by dividing the residuals series into three groups containing $n_1 = 11$, $n_2 = n_3 = 12$ values. At a significance level $\alpha = 0.05$, if the p-

THE ANNALS OF "DUNAREA DE JOS" UNIVERSITY OF GALATI
FASCICLE IX. METALLURGY AND MATERIALS SCIENCE
Nº. 3 - 2021, ISSN 2668-4748; e-ISSN 2668-4756
Article DOI: https://doi.org/10.35219/mms.2021.3.06

value corresponding to the test is greater than 0.05, the homoscedasticity hypothesis cannot be rejected.

The Kruskal-Wallis nonparametric [25] test has been performed to determine whether data series originate from the same distribution. Since the null hypothesis was rejected, the non-parametric Wilcoxon test [26] has been performed to test the same hypothesis for pairs of series.

To quantitatively appreciate the corrosion-erosion, the absolute mass variation on the surface (S) has been determined. It is computed by the equation:

$$\Delta m_t / S = (m_1 - m_t) / S \quad (1)$$

where S is the sample surface, m_1 is the initial mass of the sample and m_t is the mass at the moment t.

Finally, the gravimetric index is presented, to assess the mass loss in time per surface.

3. Results and discussion

Let us denote by t - the time, m_t - the sample mass at the moment t, s - the standard deviation, R_2 - the determination coefficient, S - the total surface of a sample.

Figures 2 (a-c) present the evolution of the mass loss of the copper sample in time, at each power level of the generator, together with the trends and their equations, while Fig. 2 (d) presents the overall evolution of the mass loss in time of this sample.

From Fig. 2 (a-c) we remark that the trend equations are parabolic and R^2 are 0.9832, 0.987 and 0.9931 respectively, so the models describe well mass loss in time.

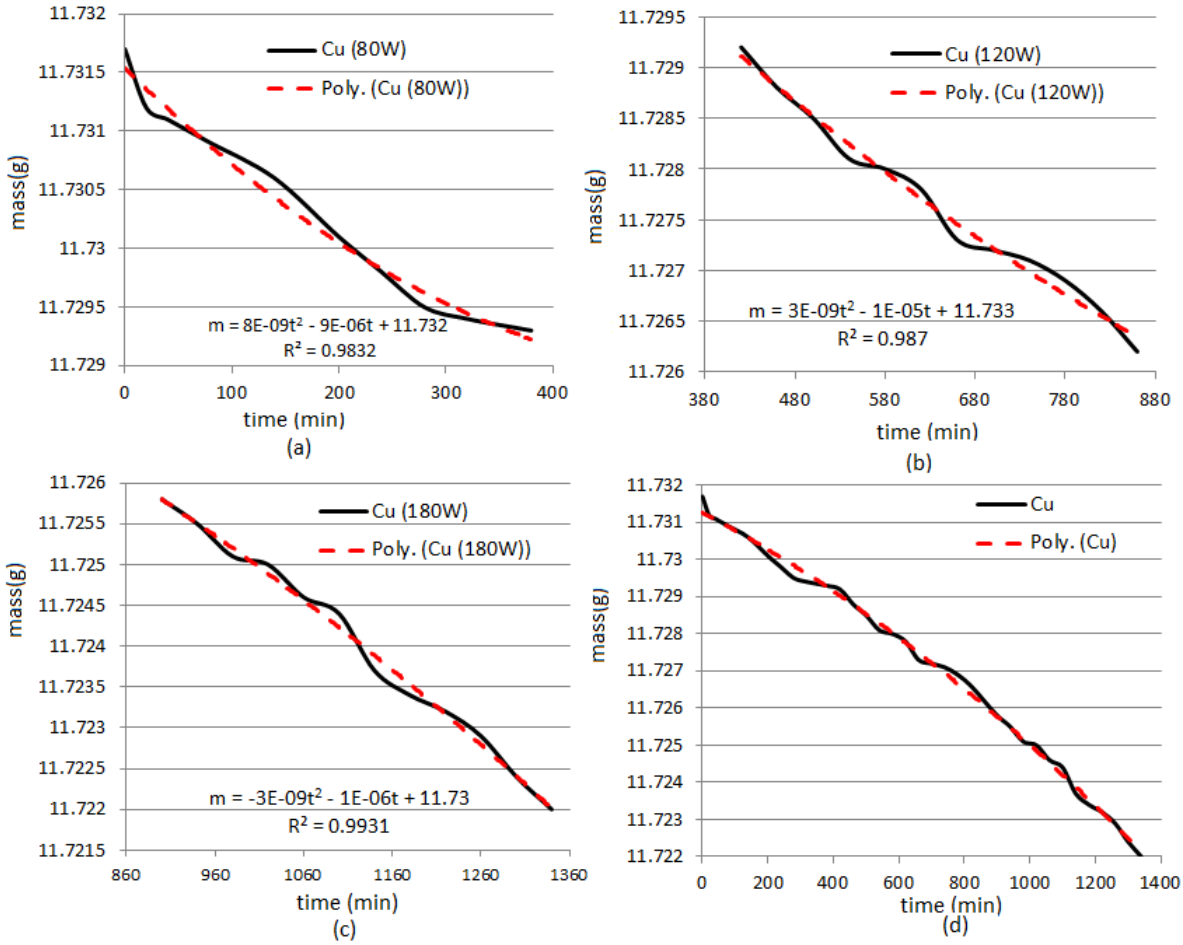

Fig. 2. *The mass variation of Cu sample: (a) at the power of 80 W, (b)at the power of 120 W, (c) at the power at 180 W, (d) during all the experiment. The continuous line represents the record data, and the dotted ones represent the trend*

THE ANNALS OF "DUNAREA DE JOS" UNIVERSITY OF GALATI
FASCICLE IX. METALLURGY AND MATERIALS SCIENCE
N°. 3 - 2021, ISSN 2668-4748; e-ISSN 2668-4756
Article DOI: https://doi.org/10.35219/mms.2021.3.06

The equation of the overall mass loss of the Cu sample is:

$$m_t = 11.731265 - 4.643760 \cdot 10^{-6} t - 1.615216 \cdot 10^{-9} t^2 \quad (2)$$

with a standard deviation s = 0.0001637 and R_2 = 0.9968.

We discuss the residuals of the model (2).

R2 is very high and s is very small, so the model is well fitted.

Figure 3(a) presents the P-P plot of the residual in the model (2). Since the observed values (represented by plots) are situated along the straight line (the central one) which represents the theoretical normal distribution, and they are inside the limit of the confidence interval (represented by the exterior continuous line) the hypothesis that the residuals are normally distributed can't be rejected. The value of the Anderson-Darling statistics is AD = 0.477, and the corresponding p-value is 0.224 > 0.05, so this test cannot reject the hypothesis that the residuals are normally distributed.

Figure 3(b) contains the residuals correlogram, together with the 95% confidence interval. Since all the values of the autocorrelation function (represented by vertical lines) are inside the confidence interval, the residual autocorrelation can be rejected.

Applying the Bartlett test, the hypothesis that the residuals in the model (2) are homoskedastic cannot be rejected because the p-value = 0.184 > 0.05.

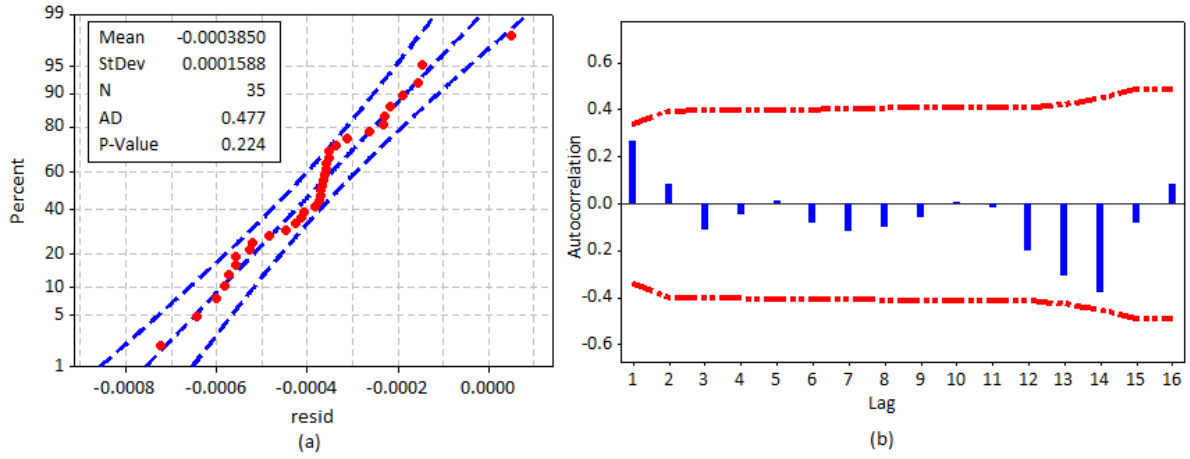

Fig. 3. *(a) Q-Q plot for residuals in the model (1); (b) The correlogram of the residual*

The results of the Kruskal-Wallis nonparametric test rejected the null hypothesis (p-val < 0.05). After performing the Wilcoxon test, the hypothesis that pairs of series have the same distribution has been rejected as well. This means that the intensity of the corrosion process in seawater depends on the generator power.

To confirm this hypothesis, the absolute mass variations on the surface have been computed for each power level. From Figure 4, it results that the absolute mass loss per surface in time is the lowest when the power was 80 W and the highest at 180 W. This is confirmed by the total mass loss, in time (Table 1), which is respectively 0.024 (at 80 W), 0.0031 g (at 120 W) and 0.042 g (at 180 W).

The gravimetric indices [$gm^{-2}h^{-1}$] are computed based on the results from Table 1. They are: 0.146706 (at 80 W), 0.150012 g (at 120 W) and 0.203242 g (at 180 W), and 0.168966 (total). The lowest is the gravimetric index for the first power level and the highest for the third one.

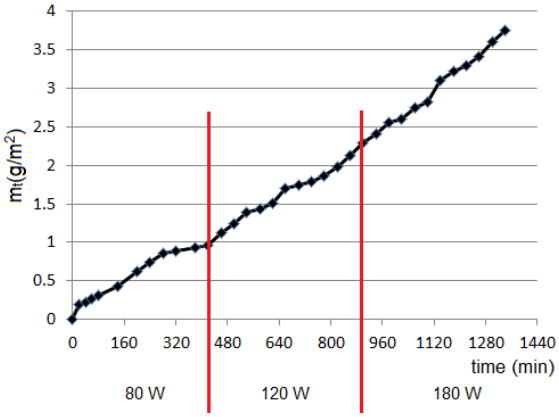

Fig. 4. *The absolute mass variations per surface. The vertical red lines delimitate the values obtained at different power of generator*

THE ANNALS OF "DUNAREA DE JOS" UNIVERSITY OF GALATI
FASCICLE IX. METALLURGY AND MATERIALS SCIENCE
N°. 3 - 2021, ISSN 2668-4748; e-ISSN 2668-4756
Article DOI: https://doi.org/10.35219/mms.2021.3.06

Table 1. *The total mass loss(g) in time (min) in seawater in the ultrasonic field*

Power [W]	Time [min]	Copper [g]
80	380	0.0024
120	480	0.0031
180	480	0.0042

4. Conclusions

The experiments proved the dependence of the erosion/corrosion speed in seawater on the generator power, increasing with the power level. This finding is in concordance with other studies. Also, it can be shown that the corrosion speed is higher than in freshwater, due to the accentuated chemical corrosion that appears due to the salt content. In the next study we shall present the comparative results of the corrosion-erosion of other copper-based materials in saline water, given the importance of these materials for the naval constructions.

References

[1]. Tang W. Z., *Physicochemical treatment of hazardous wastes*, CRC Press, USA, 2003.
[2]. Vajnhandl S., Marechal A. M. L., *Ultrasound in textile dyeing and the decolourization/mineralization of textile dyes*, Dyes Pigments, vol. 65, p. 89-101, 2005.
[3]. Wu T. Y., *et al.*, *Advances in Ultrasound Technology for Environmental Remediation*, Springer, Dordrecht, Heidelberg, New York, London, 2013.
[4]. Chen D., *Applications of ultrasound in water and wastewater treatment*, in: Handbook on application of ultrasound: sonochemistry for sustainability (Eds. D. Chen, S. K. Sharma, A. Mudhoo), CRC Press, Taylor & Francis Group, Boca Raton, USA, p. 373-406, 2012.
[5]. Anton A., *Cavitation*, Editura Academiei Române, Bucharest, Romania, 1985.
[6]. Marza V., *Contributions to the study of the ultraacoustic cavitation and of some electrical and chemical phenomena induced by it*, „Ovidius" University Press, Constanta, Romania, 2003.
[7]. Suslick K., *Ultrasound: its Chemical, Physical and Biological Effects*, VCH Pub, New York, USA, 1988.
[8]. Roy R. A., *Physical aspects of sonoluminescence from A. M. L., Ultrasound in textile dyeing and the decolourization/mineralization acoustic cavitation*, Ultrason. Sonochem., vol. 1, 1, p. S5-S8, 1994.
[9]. Young F. E., *Cavitation*, Mac Graw-Hill, Maidenhead, UK, 1989.
[10]. Rayleigh L., *On the pressure developed in a liquid during the collapse of a spherical cavity*, The London, Edinburgh, and Dublin Philos. Magazine and J. Sci., vol. 34, p. 94-98, 1917.
[11]. Dumitriu C. S., Bărbulescu A., *Studies about the copper base alloys used in naval constructions – modeling the loss mass in different media*, Sitech, Craiova, 2007.
[12]. Amann T., *et al.*, *Analysis of mechanical and chemical mechanisms on cavitation erosion-corrosion of steels in salt water using electrochemical methods*, Tribol. Int., vol. 124, p. 238-246, 2018.
[13]. Iwai I., *et al.*, *Effects of applied stress on cavitation erosion*, Wear, vol. 79 (2), p. 283-293, 1982.
[14]. Bărbulescu A., Marza V., *Electrical effect induced at the boundary of an acoustic cavitation zone*, Acta Phys. Pol. B, vol. 37(2), p. 507-518, 2006.
[15]. Bărbulescu A., *Models of the voltage induced by cavitation in hydrocarbons*, Acta Phys. Pol. B, 37 (10), p. 2919-2931, 2006.
[16]. Bărbulescu A., Toncu C., Orac L., *Analysis and models of some composites corrosion evolution*, Recent Advances in Materials Science, p. 63-69, 2008.
[17]. Bărbulescu A., Marza V., Dumitriu C. S., *Installation and method for measuring and determining the effects produced by cavitation in ultrasound field in stationary and circulating media*, Patent no RO 123086-B1, 30.09.2010.
[18]. Bărbulescu A., Dumitriu C. S., *Mathematical aspects of the study of the cavitation in liquids*, in Series on Mathematical Modelling of Environmental and Life Sciences Problems, Proceedings of the 4th Workshop, Constanţa, Romania, S. Ion, G. Marinoshi, C. Popa (eds.), Ed. Academiei Române, Bucureşti, p. 7-15, Sept. 2005.
[19]. Bărbulescu, A. Dumitriu C. S., *Models of the mass loss of some copper alloys*, Chem. Bull. Politehnica University (Timişoara), vol. 52 (66), 1-2, p. 120-123, 2007.
[20]. Dumitriu C. Ș., Dragomir F., *Modeling the signals collected in cavitation field by stochastic and Artificial intelligence methods*, 13th International Conference on Electronics, Computers and Artificial Intelligence (ECAI), 01-03 July, Pitești, Romania, p. 1-4, doi: 10.1109/ECAI52376.2021.9515016, 2021.
[21]. Bărbulescu A., Dumitriu C. S., *ARIMA and Wavelet-ARIMA Models for the Signal Produced by Ultrasound in Diesel*, ICSTCC, Iasi (accepted), 2021.
[22]. Bărbulescu A., Dumitriu C. S., *Assessing the Fractal Characteristics of Signals in Ultrasound Cavitation*, ICSTCC, Iasi (accepted), 2021.
[23]. Anderson T. W., Darling D. A., *Asymptotic theory of certain "goodness-of-fit" criteria based on stochastic processes*, Ann. Math. Stat., vol. 23, p. 193-212, doi:10.1214/aoms/1177729437, 1952.
[24]. Bartlett M. S., *Properties of sufficiency and statistical tests*, Proc. Royal Stat. Soc. A, vol. 160, p. 268-282, 1932.
[25]. Kruskal W. H., Wallis W. A., *Use of ranks in one-criterion variance analysis*, J. Am. Stat. Assoc., vol. 47 (260), p. 583-621, doi:10.1080/01621459.1952.10483441, 1952.
[26]. Mann H. B., Whitney D. R., *On a Test of Whether one of Two Random Variables is Stochastically Larger than the Other*, Ann. Math. Stat., vol. 18 (1), p. 50-60. doi:10.1214/aoms/1177730491, 1947.

THE ANNALS OF "DUNAREA DE JOS" UNIVERSITY OF GALATI
FASCICLE IX. METALLURGY AND MATERIALS SCIENCE
Nº. 3 - 2021, ISSN 2668-4748; e-ISSN 2668-4756
Article DOI: https://doi.org/10.35219/mms.2021.3.07

USE OF TAGUCHI METHODS FOR HIERARCHY OF INFLUENCE FACTORS IN THE APPLICATION OF CARBONITRATION IN A FLUIDIZED BED STEEL FOR 41Cr4 STEEL

Nelu CAZACU
"Dunarea de Jos" University of Galati, Romania
e-mail: nelu.cazacu@ugal.ro

ABSTRACT

The work is based on carbonitriding in a fluidized layer with methane and ammonia gas applied to 41Cr4 steel samples. To achieve the best possible results, other factors must be taken into account, than those specific to carbonitring. It was necessary to use a partially factorial working procedure due to the increase in the number of factors. An A18 matrix has been used, with 18 lines of experiments in which three levels have been modified for 6 factors. The objective function was fixed at the final hardness after carbonitriding, hardening and tempering. The carbonitriding was performed in fluidized bed with granular solid ground and sorted to 0.1- to 0.16mm, and brought to fluidization with a mixture of methane and ammonia. The hardening has been done directly after carbonitriding in the fluidized bed. The experiments have been performed according to Taguchi Methods and the results indicate an optimal regime and the influence of the factors considered on the hardness after the thermo-chemical treatment and the thermal treatment. Metallographic analysis has been performed on the carbonitrided layer.

KEYWORDS: fluidized bed, Taguchi method (T M), 41Cr4, carbonitriding

1. Introduction

The fluidized bed is used as a medium for heat treatments of small bulk parts providing high heat transfer and mass capacities. High heat and mass transfer coefficients lead to balancing treatment costs by drastically reducing the process time. The limitations brought by the fluidization are related to the dimensions of the fluidization spaces and implicitly to the dimensions of the parts, and last but not least to the treatment costs. The quality indicators are influenced by the positioning of the active surfaces in relation to the axis of the fluidization chamber [1].

41Cr4 steel is an alloy steel for improvement but to which subsequent surface treatments can be applied. Usually this steel is intended for: - machine parts and heat-treated parts with a guaranteed hardening depth according to the brand's quality curve such as: smooth shafts, grooved shafts, crankshafts, bandages.

The chemical composition of 41Cr4 steel is: C = (0.36÷0.44)%; P = max 0.035%; Mn = (0.50÷0.80)%; S = max 0.035%, Si = (0.17÷0.37)%; Cr = (0.8÷1.1)%.

Also, some residual elements are accepted: max. 0.3% Ni; max. 0.3% Cu; max. 0.02% Ti (Table 1).

Forms of delivery: hot rolled flat products; semi-finished products for forging; rolled and drawn wires

Recommended heat treatments:

Soaking annealing consisting of austenitization at T = (680 ÷ 720) °C followed by oven cooling.

Normalization for which austenitization is performed at T = (840 ÷ 870) °C followed by cooling in still air.

The most important treatment is martensitic volumetric hardening, which is done after austenitization at T = (820 ÷ 850) °C followed by cooling in water and with subsequent cooling in water or oil.

Afterwards, surface treatments can be made for nitriding, nitrocarburizing or local hardening by laser hardening.

Carbonitriding is considered the most widely used thermo-chemical treatment (surface heat treatment with diffusion) [1]. The presence of active nitrogen in the decomposition of ammonia makes it possible to increase the chemical activity of carbon at lower heating temperatures, which leads to a decrease in costs without affecting the structure/surface

THE ANNALS OF "DUNAREA DE JOS" UNIVERSITY OF GALATI
FASCICLE IX. METALLURGY AND MATERIALS SCIENCE
Nº. 3 - 2021, ISSN 2668-4748; e-ISSN 2668-4756
Article DOI: https://doi.org/10.35219/mms.2021.3.07

properties complex. Carbonitriding leads to a controlled increase in surface carbon and it may lead to changes in surface properties relative to the base material if surface treatment is properly continued. The paper studies the situation in which, in order to increase the hardenability of the surface layer, a surface treatment is made prior to the hardening and recovery mentioned above. In this case, the fluidized bed is used as a carbonitriding medium, which brings new process control factors [2, 3]. The experimental procedure used is based on TM with orthogonal array [2] to determine the share of influencing factors on the overall heat treatment applied to 41Cr4 steel.

2. Experimental conditions

Samples of 41Cr4 steel have been used for experiments. The chemical composition is shown in Table 1 and it reveals the class of steels to which it belongs, namely steels with 1% Cr. The steel is intended for improvement, but the application prior to the improvement of a carbonitriding treatment versus the increase of the calcification of the surface layer and thus, of the complex of superior surface properties, can be obtained [2-4].

It is a mass and energy transfer medium that can be very active which leads to high values of mass and energy transfer coefficients. For example, for an ITTSF furnace (5) with a fluidized layer with a diameter of 0.35 m and initial H/D ratio = 1.1 the temperature of the centre of a spherical sample with a diameter of 0.05 m introduced in the incubator with the temperature of 850 ºC, shows that by increasing the fluidization speed c = it occurs a significant decrease in equalization time to approx. 100 s of the sample temperature. For the same oven without a fluidized bed that has been transformed into an electric oven with a retort, the equalization time of the sample is 400 s. It is also found that the fluidization speed influences, within certain limits, the heat transfer process (Fig. 1).

Similarly, fluidization speed also influences the mass transfer coefficient, which becomes important in surface diffusion treatments such as carbonitriding (Table 2) [1].

Table 1. *Chemical composition of 41Cr4 steel samples*

C	Mn	Si	P	S	Cr	Ni	Cu	Mo	Al
0.4	0.6	0.3	0.019	0.02	0.97	0.2	0.27	0.065	0.015

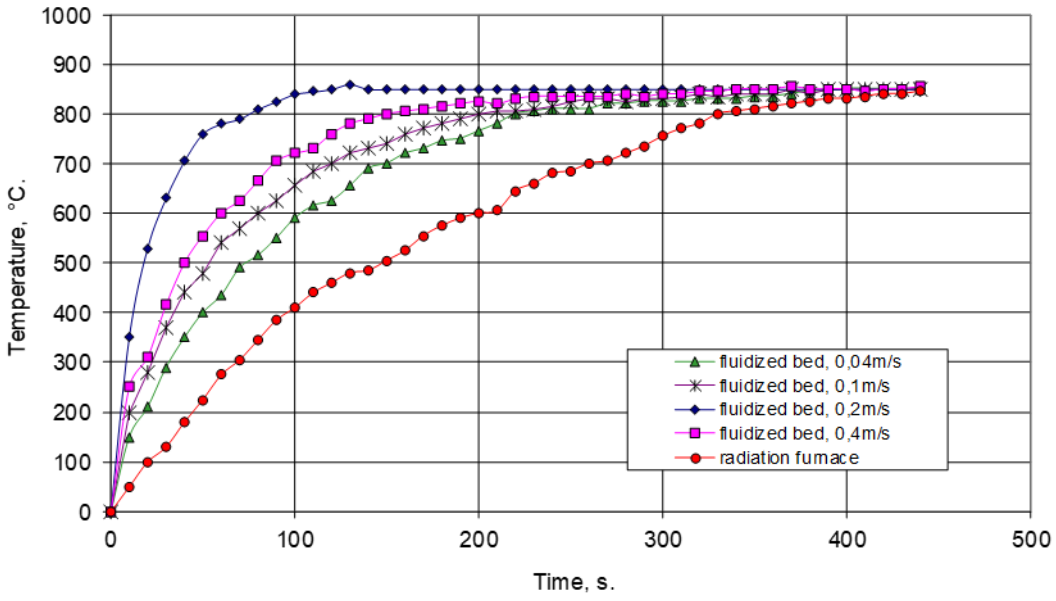

Fig. 1. *Temperature variation of a stainless-steel spherical sample (2 inches) when introduced at an 85 ºC in an electric furnace at and in a fluidized bed furnace (ITTSF (5), for different fluidization speed)* [1]

THE ANNALS OF "DUNAREA DE JOS" UNIVERSITY OF GALATI
FASCICLE IX. METALLURGY AND MATERIALS SCIENCE
N°. 3 - 2021, ISSN 2668-4748; e-ISSN 2668-4756
Article DOI: https://doi.org/10.35219/mms.2021.3.07

Table 2. *Fluidisation speed (levels for experiments)*

no.	debit			under mesh speed	fluidisation speed
1	394	6.56	0.394	0.015	0.029
2	544	9.07	0.544	0.021	0.040
3	694	11.57	0.694	0.027	0.051

Table 3. *Other factors that characterize used fluidized bed*

parameter	symbol	value	m.u.
the average diameter of the soli	d_p	0.00024	m
form factor	ϕ	0.6	-
solid density	ρ_p	2650	kg/m^3
gas density	ρ_g	1.29	kg/m^3
kinematic viscosity	η	1.34E-05	m^2/s
gravitational acceleration	g	9.81	m/s^2
initial height of the bed	H	0.1	m
Inside diameter of the enclosure	D	0.096	m
Archimedes' criterion	Ar	1550.74	-
initial porosity	ε	0.52	-
fluidization speed	w	0.000154	m/s

Table 4. *Factors considered to have significant influence over experiments*

No.	factors	mu	range
1	carbonitriding temperature	°C	800…900
2	carbonitriding time	s	60…600
3	debit	l/h	433, 584, 734
4	tempering temperature	°C	100... 250
5	tempering time	min	5...15
6	pozition in furnace	-	low, medium, high
7	dimension of granular solid	$m*10^{-3}$	0,10…0,16
8	fluidized bed volume	m^3	ct
9	steel chemical composition	%	ct.
10	fluidized bed shape rate D/H	-	1…1,5
11	ammonia rate	%	5…15
12	surface quality	-	small, medium, large

2.1. Experimental matrix

The multitude of factors influences the process of carbonitriding + hardening + tempering, to which are added the influencing factors of fluidization and carbonitriding in fluidized layer, making the factors in Table 5 to be selected from Tables 4. Previous experiments [3] for the carbonitriding of 41Cr4 steel in a fluidized layer with an initial gaseous mixture of methane and ammonia, showed the factors influencing the experiments and their fields of variation Table 4.

According to the procedure known as Taguchi Methods [6-8] when the number of factors is large, it is difficult to perform "full factorial" technological experiments due to increased costs, duration of experiments and their complexity, the use of experimental matrix being recommended. Using an appropriate mathematical model [6, 8], a matrix with a small number of experiments can be constructed.

For the proposed experiments we have the orthogonal matrix L18, with 18 lines, which has 8 factors considered and each three values. 3^8 = 6561 experiments are replaced with 18 experiments.

THE ANNALS OF "DUNAREA DE JOS" UNIVERSITY OF GALATI
FASCICLE IX. METALLURGY AND MATERIALS SCIENCE
Nº. 3 - 2021, ISSN 2668-4748; e-ISSN 2668-4756
Article DOI: https://doi.org/10.35219/mms.2021.3.07

Another property that results from the orthogonality of the matrix is that two columns can be omitted (column 1 and column 7) without influencing the result of the experiments, thus obtaining a matrix with 18 lines for 6 factors and each with three levels i.e., 3^6 = 729 experiments are replaced with 18 experiments.

The results provide the weight of influence of the considered factors and they can be completed with a set of full-factorial experiments on a much smaller number of factors and with smaller domains of variation [6, 8].

Orthogonal matrix L18 [6, 8] is presented in Table 6. Completing the L18 matrix with the values of the factor levels it will lead to the experiment matrix with 18 lines Table 7. The main difficulty of this experimental matrix is that the transition from one line to another is done by modifying the settings for several factors, which in the "full factorial" type experiment matrix means changing only one factor.

Table 5. *Selected factors over experiments*

no.	factors	m.u.	selected levels		
			1	2	3
1	carbonitriding temperature	°C	800	850	900
2	carbonitriding time	min	1	5	10
3	debit	l/h	394	544	694
4	tempering temperature	°C	100	150	200
5	tempering time	min	5	10	15
6	ammonia rate	%	5	10	15

Table 6. *Typical orthogonal array L18 for 6 factors and each 3 levels*

Experiment	Factori specificati							
	1	2	3	4	5	6	7	8
	e	A	B	C	D	E	e	F
1	1	1	1	1	1	1	1	1
2	1	1	2	2	2	2	2	2
3	1	1	3	3	3	3	3	3
4	1	2	1	1	2	2	3	3
5	1	2	2	2	3	3	1	1
6	1	2	3	3	1	1	2	2
7	1	3	1	2	1	3	2	3
8	1	3	2	3	2	1	3	1
9	1	3	3	1	3	2	1	2
10	2	1	1	3	3	2	2	1
11	2	1	2	1	1	3	3	2
12	2	1	3	2	2	1	1	3
13	2	2	1	2	3	1	3	2
14	2	2	2	3	1	2	1	3
15	2	2	3	1	2	3	2	1
16	2	3	1	3	2	3	1	2
17	2	3	2	1	3	1	2	3
18	2	3	3	2	1	2	3	1

THE ANNALS OF "DUNAREA DE JOS" UNIVERSITY OF GALATI
FASCICLE IX. METALLURGY AND MATERIALS SCIENCE
No. 3 - 2021, ISSN 2668-4748; e-ISSN 2668-4756
Article DOI: https://doi.org/10.35219/mms.2021.3.07

Table 7. *Experimental matrix with 18 lines*

experiment	specified factors					
	1	2	3	4	5	6
	carbonitriding temperature	carbonitriding time	debit	tempering temperature	tempering time	ammonia rate
	A	B	C	D	E	F
m.u.	°C	min	l/h	°C	min	%
1	800	1	394	100	5	5
2	800	5	544	150	10	10
3	800	10	694	200	15	15
4	850	1	394	150	10	15
5	850	5	544	200	15	5
6	850	10	694	100	5	10
7	900	1	544	100	15	15
8	900	5	694	150	5	5
9	900	10	394	200	10	10
10	800	1	694	200	10	5
11	800	5	394	100	15	10
12	800	10	544	150	5	15
13	850	1	544	200	5	10
14	850	5	694	100	10	15
15	850	10	394	150	15	5
16	900	1	694	150	15	10
17	900	5	394	200	5	15
18	900	10	544	100	10	5

Table 8. *Hardness determination for each experiment and target function calculus*

experiment	hardness		average hardness	target function
	HV1	HV2		
m.u	kgf/mm^2	kgf/mm^2	kgf/mm^2	dB
1	336	341	339	25.30
2	781	857	819	29.13
3	701	655	678	28.31
4	667	667	667	28.24
5	795	857	826	29.17
6	946	1027	987	29.94
7	825	825	825	29.16
8	781	781	781	28.93
9	810	891	851	29.30
10	494	509	502	27.00
11	874	810	842	29.25
12	857	825	841	29.25
13	713	689	701	28.46
14	825	857	841	29.25
15	891	874	883	29.46
16	752	781	767	28.85
17	726	701	714	28.53
18	739	766	753	28.77
			m=	28.68

THE ANNALS OF "DUNAREA DE JOS" UNIVERSITY OF GALATI
FASCICLE IX. METALLURGY AND MATERIALS SCIENCE
N°. 3 - 2021, ISSN 2668-4748; e-ISSN 2668-4756
Article DOI: https://doi.org/10.35219/mms.2021.3.07

Table 9. *Calculus for average effect of each level for each factor over experiments*

	relation	value
mA1=	1/6(n1+n2+n3+n10+n11+n12)=	28.04
mA2=	1/6(n4+n5+n6+n13+n14+n15)=	29.09
mA3=	1/6(n7+n8+n9+n16+n17+n18)=	28.92
mB1=	1/6(n1+n4+n7+n10+n13+n16)=	27.83
mB2=	1/6(n2+n5+n8+n11+n14+n17)=	29.04
mB3=	1/6(n3+n6+n9+n12+n15+n18)=	29.17
mC1=	1/6(n1+n4+n9+n11+n15+n17)=	28.35
mC2=	1/6(n2+n5+n7+n12+n13+n18)=	28.99
mC3=	1/6(n3+n6+n8+n10+n14+n16)=	28.71
mD1=	1/6(n1+n6+n7+n11+n14+n18)=	28.61
mD2=	1/6(n2+n4+n8+n12+n15+n16)=	28.98
mD3=	1/6(n3+n5+n9+n10+n13+n17)=	28.46
mE1=	1/6(n1+n6+n8+n12+n13+n17)=	28.40
mE2=	1/6(n2+n4+n9+n10+n14+n18)=	28.61
mE3=	1/6(n3+n5+n7+n11+n15+n16)=	29.03
mF1=	1/6(n1+n5+n8+n10+n15+n18)=	28.10
mF2=	1/6(n2+n6+n9+n11+n13+n16)=	29.15
mF3=	1/6(n3+n4+n7+n12+n14+n17)=	28.79
	m=	28.68

Table 10. *Average effect of each level of each factor*

factors			levels		
		m.u.	1	2	3
A	carbonitriding temperature	dB	28.04	29.09	28.92
B	carbonitriding time	dB	27.83	29.04	29.17
C	debit	dB	28.35	28.99	28.71
D	tempering temperature	dB	28.61	28.98	28.46
E	tempering time	dB	28.40	28.61	29.03
F	ammonia rate	dB	28.10	29.15	28.79
			average	m=	28.68

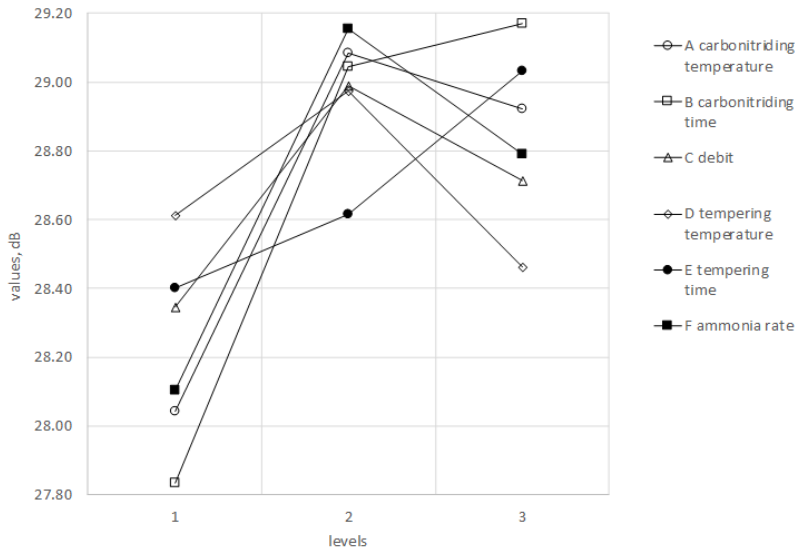

Fig. 2. *Graphical representation for average effect of each level of each factor*

THE ANNALS OF "DUNAREA DE JOS" UNIVERSITY OF GALATI
FASCICLE IX. METALLURGY AND MATERIALS SCIENCE
N°. 3 - 2021, ISSN 2668-4748; e-ISSN 2668-4756
Article DOI: https://doi.org/10.35219/mms.2021.3.07

Table 11. *ANOVA Analysis*

	factor	SSDTF	weight of factor
	m.u.	$(dB)^2$	%
A	carbonitriding temperature	3.79	22.06
B	carbonitriding time	6.53	37.98
C	debit	1.25	7.27
D	tempering temperature	0.84	4.86
E	tempering time	1.25	7.25
F	ammonia rate	3.53	20.57
	Total	17.18	

3. Experiments

The experiments have been performed following the experimental matrix from Table 7. After completing the 18 experiments on steel sample cabs thus treated, hardness measurements were made on the flat surface, far from the edges (Table 8). For each experiment, the objective function was calculated with the relationship specific to the dependence "the greater is the better" (it is desired to achieve the highest hardness):

$$n = 10log\ (HVm)$$

The average objective function was calculated for all 18 experiments (Table 8). An important step in the procedure is to calculate the average effect of the level of each factor for all 18 levels (6 factors x3 levels). This is shown in Table 9. It should be noted that the properties of orthogonal matrices also include the frequency of identical occurrence in the matrix for each level of each factor, which means that simplifications of the mathematical model do not influence the achievement of the technological objective by more than a few percent [6, 8].

The reorganisation of the values of the mean effect of each factor as in Table 10, allows an intuitive graphical representation (Fig. 2). This graphical representation shows how each factor influences the selected range of variation, respectively the allure of the influence (linear ascending, linear decreasing, with maximum, with minimum, without influence, etc.).

4. Results and discussion

The metallographic analysis of the surface layers after carbonitriding is shown from Fig. 5 to Fig. 20.

The microstructures show the combined influence of factors A, B, C and F that influence the carbonitriding process in the fluidized layer. An analysis of the micrographs shows that:

- for carbonitriding temperatures of 800 °C (experiments 1, 2, 3, 10, 11 and 12;
- for carbonitriding temperatures of 850 °C experiments 4, 5, 6, 13, 14 and 15;
- for carbonitriding temperatures of 900 °C experiments 7, 8, 9, 16, 17 and 18.

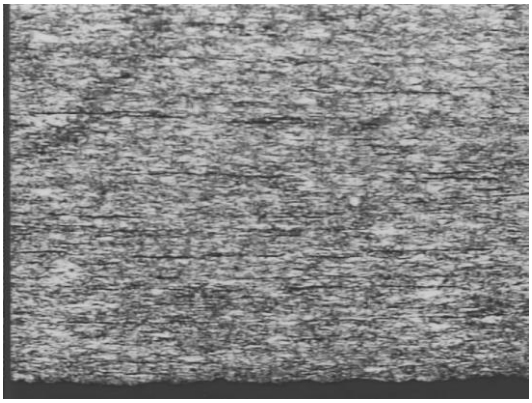

Fig. 3. *Heat and thermochemical treatment according to regime 1 (magnification 50x, attack: nital 2%)*

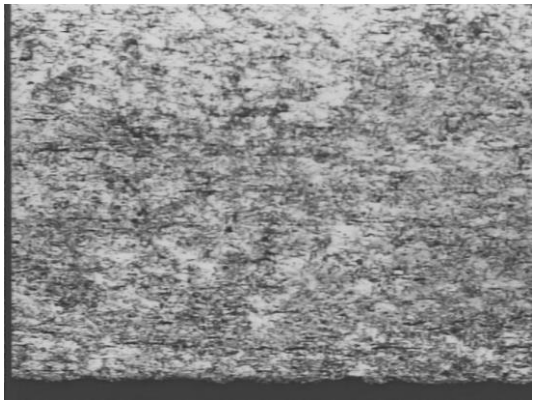

Fig. 4. *Heat and thermochemical treatment according to regime 2 (magnification 50x, attack: nital 2%)*

THE ANNALS OF "DUNAREA DE JOS" UNIVERSITY OF GALATI
FASCICLE IX. METALLURGY AND MATERIALS SCIENCE
Nº. 3 - 2021, ISSN 2668-4748; e-ISSN 2668-4756
Article DOI: https://doi.org/10.35219/mms.2021.3.07

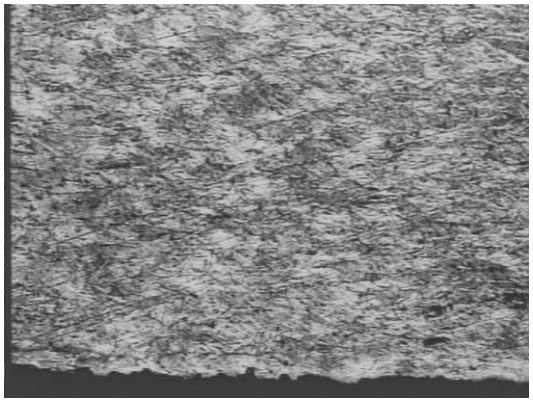

Fig. 5. *Heat and thermochemical treatment according to regime 3 (magnification 50x, attack: nital 2%)*

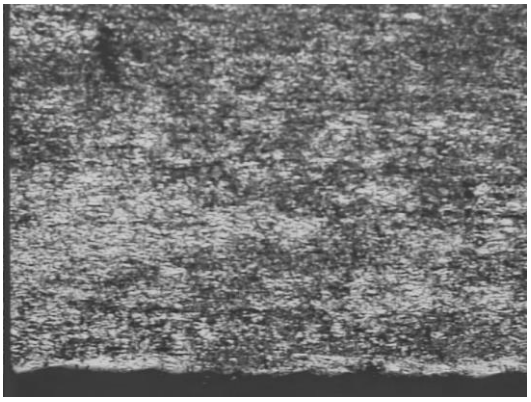

Fig. 8. *Heat and thermochemical treatment according to regime 6 (magnification 50x, attack: nital 2%)*

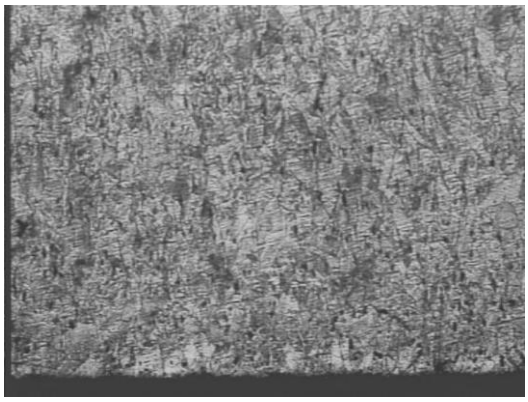

Fig. 6. *Heat and thermochemical treatment according to regime 4 (magnification 50x, attack: nital 2%)*

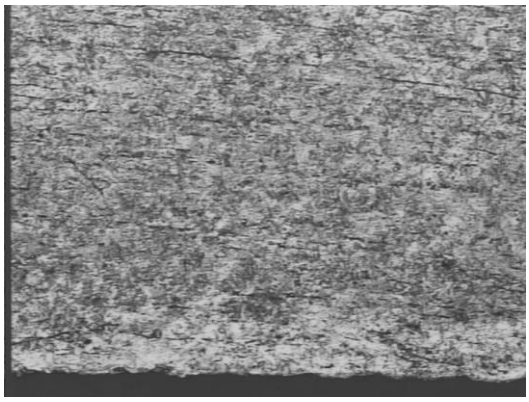

Fig. 9. *Heat and thermochemical treatment according to regime 7 (magnification 50x, attack: nital 2%)*

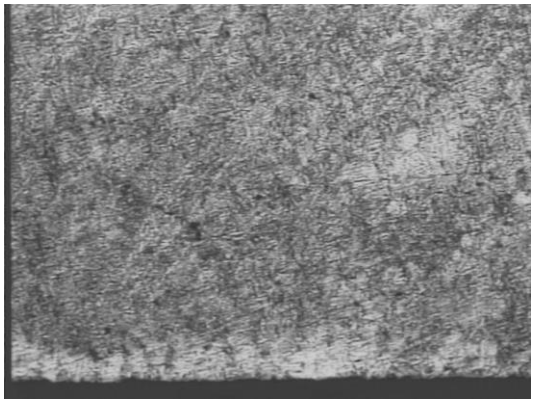

Fig. 7. *Heat and thermochemical treatment according to regime 5 (magnification 50x, attack: nital 2%)*

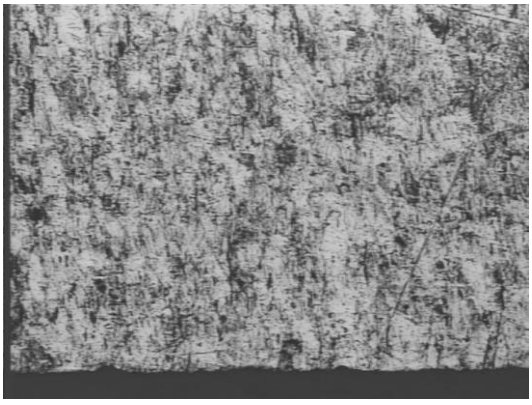

Fig. 10. *Heat and thermochemical treatment according to regime 8 (magnification 50x, attack: nital 2%)*

THE ANNALS OF "DUNAREA DE JOS" UNIVERSITY OF GALATI
FASCICLE IX. METALLURGY AND MATERIALS SCIENCE
Nº. 3 - 2021, ISSN 2668-4748; e-ISSN 2668-4756
Article DOI: https://doi.org/10.35219/mms.2021.3.07

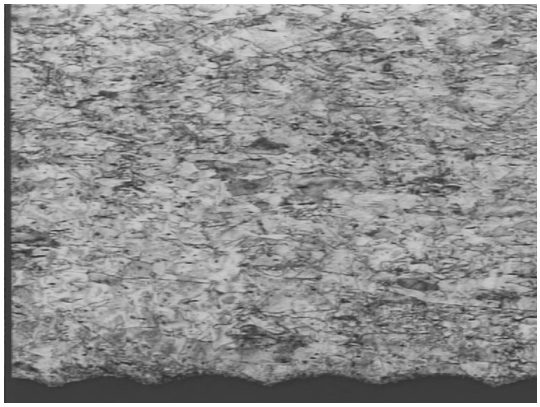

Fig. 11. *Heat and thermochemical treatment according to regime 9 (magnification 50x, attack: nital 2%)*

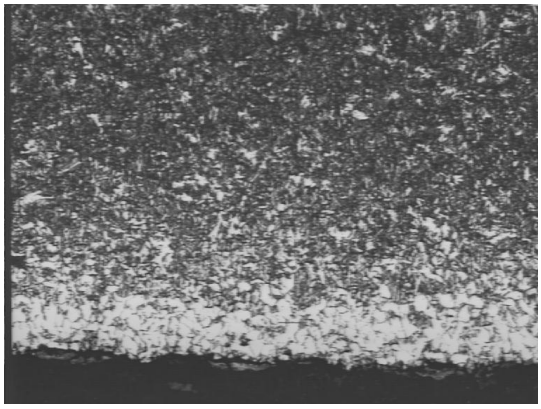

Fig. 12. *Heat and thermochemical treatment according to regime 10 (100x magnification, attack: nital 2%)*

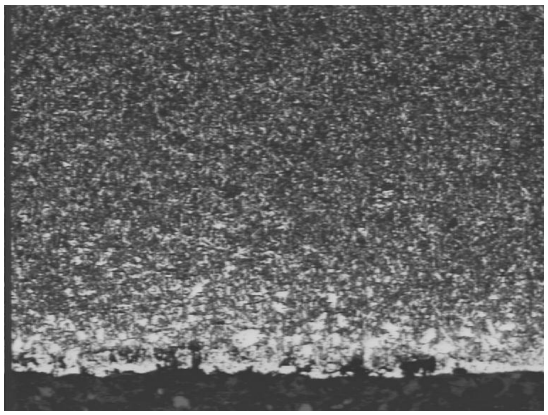

Fig. 13. *Heat and thermochemical treatment according to regime 11 (magnification 100x, attack: nital 2%)*

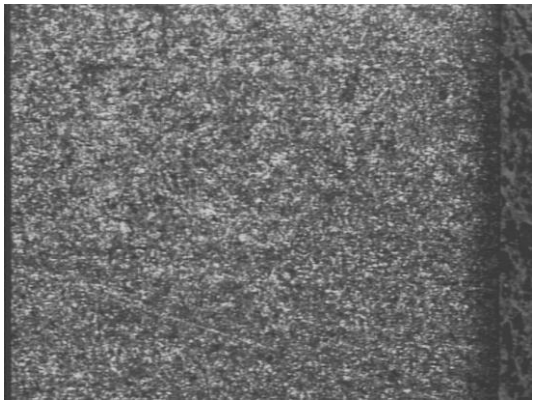

Fig. 14. *Heat and thermochemical treatment according to regime 12 (magnification 50x, attack: nital 2%)*

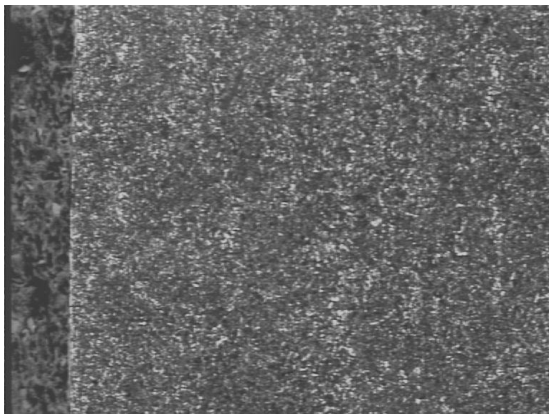

Fig. 15. *Heat and thermochemical treatment according to regime 13 (100x magnification, attack: nital 2%)*

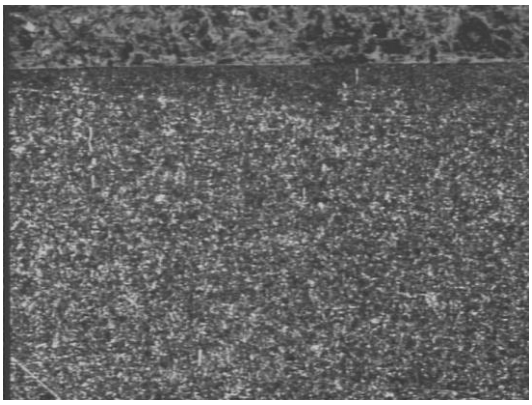

Fig. 16. *Heat and thermochemical treatment according to regime 14 (100x magnification, attack: nital 2%)*

THE ANNALS OF "DUNAREA DE JOS" UNIVERSITY OF GALATI
FASCICLE IX. METALLURGY AND MATERIALS SCIENCE
Nº. 3 - 2021, ISSN 2668-4748; e-ISSN 2668-4756
Article DOI: https://doi.org/10.35219/mms.2021.3.07

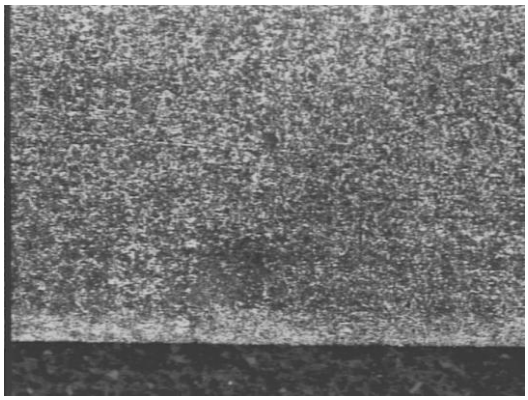

Fig. 17. *Heat and thermochemical treatment according to regime 15 (magnification 100x, attack: nital 2%)*

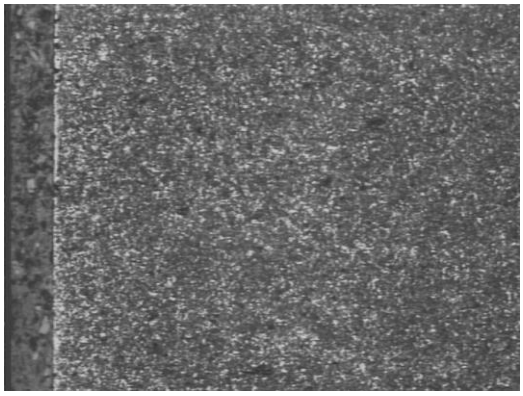

Fig. 18. *Heat and thermochemical treatment according to regime 16 (magnification 100x, attack: nital 2%)*

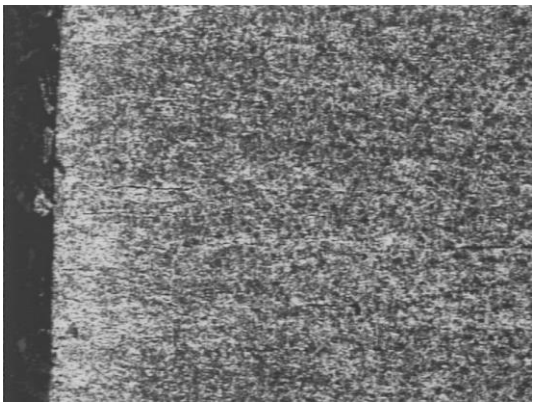

Fig. 19. *Heat and thermochemical treatment according to regime 17 (magnification 100x, attack: nital 2%)*

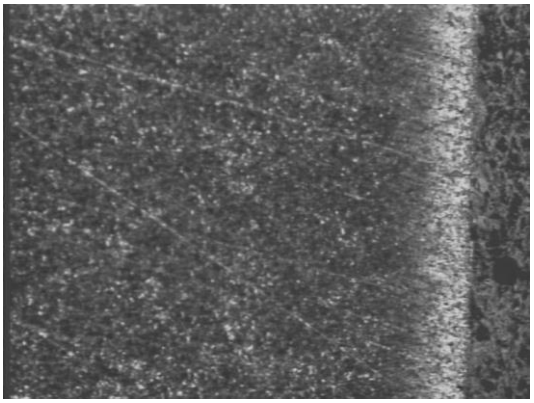

Fig. 20. *Heat and thermochemical treatment according to regime 18 (100x magnification, attack: nital 2%)*

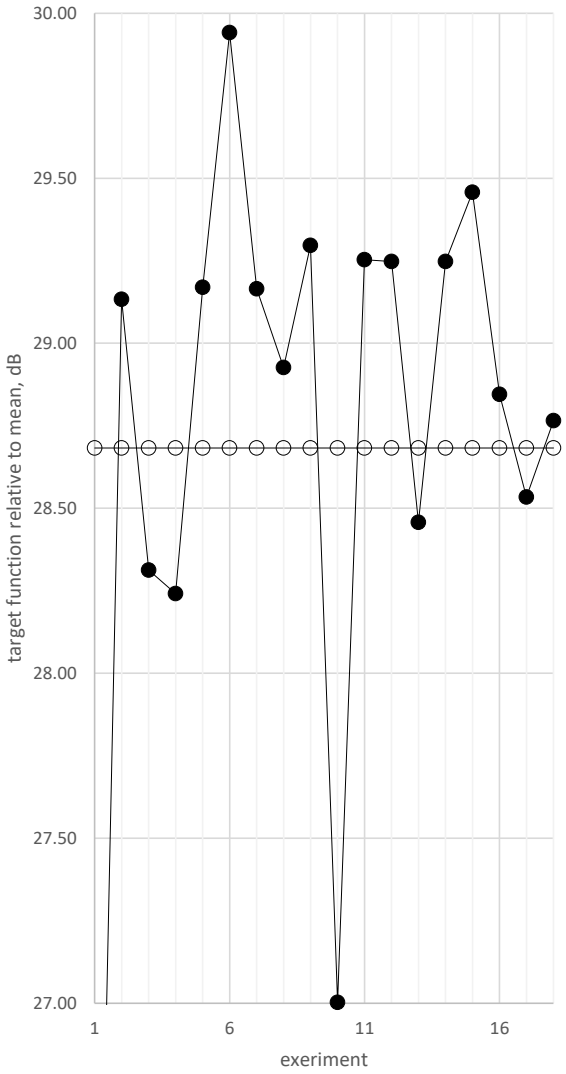

Fig. 21. *Target function variations over experiments and mean*

THE ANNALS OF "DUNAREA DE JOS" UNIVERSITY OF GALATI
FASCICLE IX. METALLURGY AND MATERIALS SCIENCE
Nº. 3 - 2021, ISSN 2668-4748; e-ISSN 2668-4756
Article DOI: https://doi.org/10.35219/mms.2021.3.07

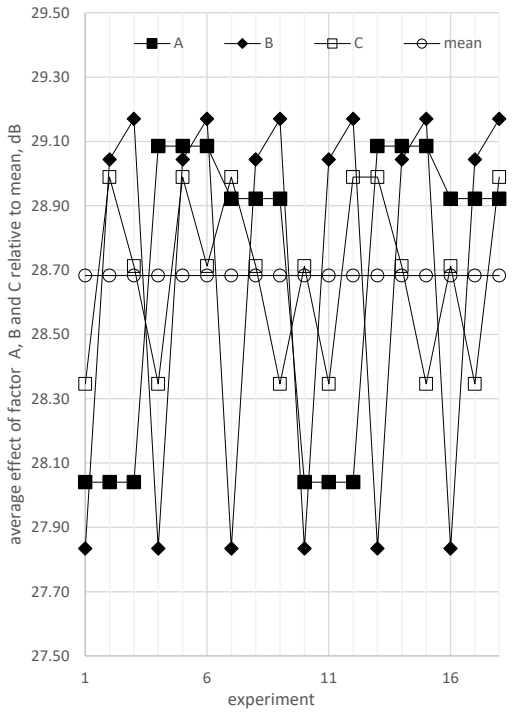

Fig. 22. *Average effect of factor A, B and C over experiments relative to mean*

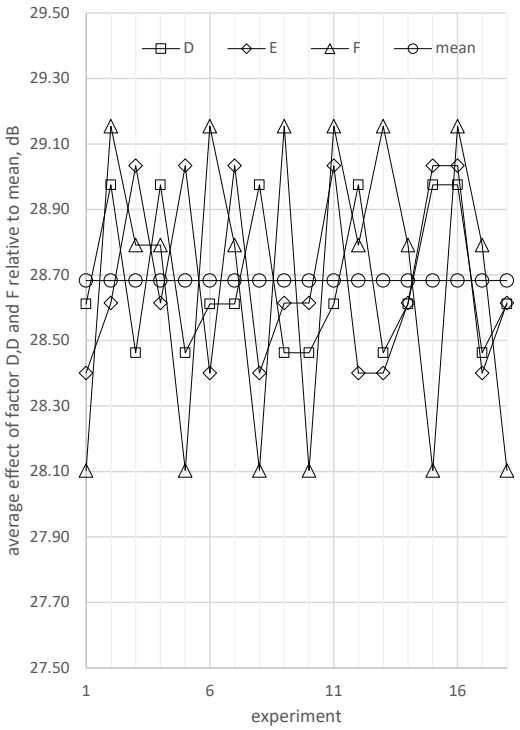

Fig. 23. *Average effect of factor E, F and G over experiments relative to mean*

Table 13. *Optimal setting for each level of each factor*

	factors	levels			
		m.u.	1	2	3
A	carbonitriding temperature	dB		29.09	
B	carbonitriding time	dB			29.17
C	debit	dB		28.99	
D	tempering temperature	dB		28.98	
E	tempering time	dB			29.03
F	ammonia rate	dB		29.15	
			average	m=	9.69

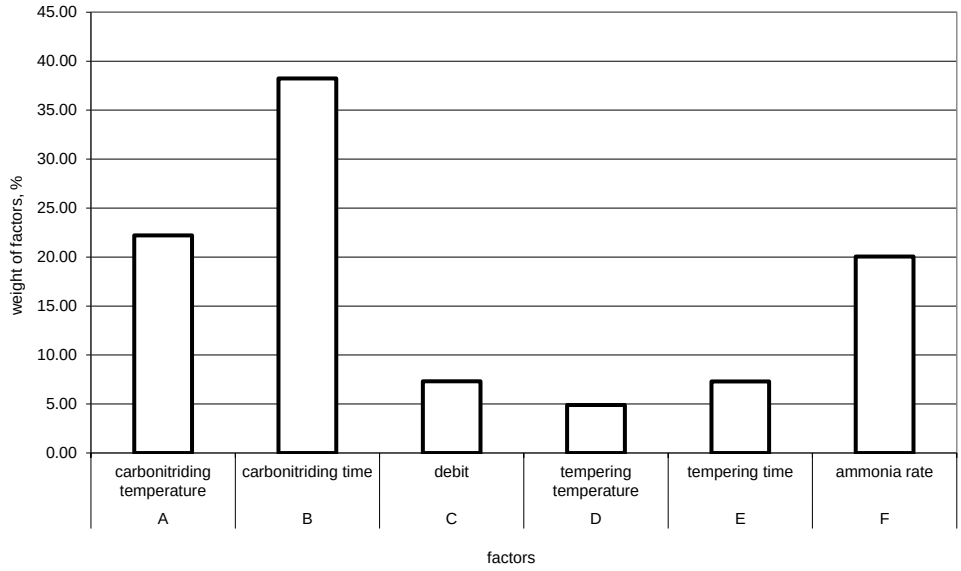

Fig. 24. *Weight of factors over experiments*

THE ANNALS OF "DUNAREA DE JOS" UNIVERSITY OF GALATI
FASCICLE IX. METALLURGY AND MATERIALS SCIENCE
Nº. 3 - 2021, ISSN 2668-4748; e-ISSN 2668-4756
Article DOI: https://doi.org/10.35219/mms.2021.3.07

4. Conclusions

The carbonitride layer at high temperatures has a structure similar to the carburized layer (microstructures made before the final hardening) (Fig. 5-20) nitrogen increases the diffusion coefficient of carbon simultaneously with the decrease of the treatment temperature.

Carbonitriding temperatures allow a direct hardening from that temperature, with the advantage of the open chamber used for fluidization.

The mathematical experimentation procedure in orthogonal matrix with its afferent mathematical model offers the different importance of the factors on the experiment, the character of the influence (linear, logarithmic, with maximum / minimum) (Fig. 2.

The microstructures confirm the realization of the thermal and thermochemical treatment processes.

The highest hardness is obtained at temperatures of 850 °C and a holding time of 10 min (regime 6) (Table 7, Fig. 8). The lowest hardness has been obtained at temperatures of 800 °C and a holding time of 1min (Table 7, Fig. 3). The influence of temperature and time on carbonitriding is most obvious and is in line with recognized technologies [9, 10].

The greatest influence on a carburized layer has carbonitriding temperatures, carbonitriding time and the proportion of ammonia. These factors can be considered centroid factors, for which the measurement accuracy is significantly increased.

The least influence on the carburized layer has the inlet gas flow, tempering temperature and return time (Fig. 22).

Experiments show once again that the use of fluidized layers in heat and thermochemical treatments reduces the duration of treatments directly (through specific heat and mass transfer phenomena) and indirectly by reducing loading / unloading times due to working with the enclosure open (Table 7).

References

[1]. ***, *ASM Handbook. Heat Treating*, vol. 4, s.l., ASM International, ISBN 0-87170-379-3, 1991.
[2]. Dobrovici Sorin, Bâclea Adolf, *Weight Factors over Carbonitriding in Fluidized Bed for 40Cr10 Steel*, The Annals of "Dunarea de Jos" University of Galati, Fascicle IX, Metallurgy and Materials Science, p. 70-74, ISSN 1453-083X, 2002.
[3]. Dobrovici Sorin, Cazacu Nelu, *Some Aspects of 40Cr10 Steel Behavior on Fluidized Bed Carbonitriding*, The Annals of "Dunarea de Jos" University of Galati, Fascicle IX, Metallurgy and Materials Science, p. 17-22, ISSN 1453-083X, 1999.
[4]. Bâclea Adolf, *et al.*, *Surface Hardening of 40Cr10 Steel After Short Time Nitriding in Fluidized bed*, The Annals of "Dunarea de Jos" University of Galati, Fascicle IX, Metallurgy and Materials Science, vol. 2, p. 40-44, ISSN 1453-083X, 2006.
[5]. ***, ITTSF paper.
[6]. Taguchi G., *Introduction to quality engineering into products and processes*, s.l.: Asian productivity organization, 1986.
[7]. Logothetis N., Wynn H. P., *Quality through design*, Oxford: Clarendon Press, ISBN 0 19 859395 3, 1994.
[8]. Phadke M. S., *Quality engineering using robust design*, Englewood Cliffs, New Jersey: Prentice Hal, 1989.
[9]. Samoila C., Ionescu M.S., Drugă L., *Tehnologii şi utilaje moderne de încălzire*, Bucureşti: Editura Tehnică, 1986.
[10]. Vermeşan G., *Tratamente termice*, Indrumător, Editura Dacia: Cluj Napoca, 1987.
[11]. Popescu N., Vitănescu C., *Tehnologia tratamentelor termice*, Bucureşti: Editura Tehnică, 1974.
[12]. Mihăilă C., *Procese termodinamice în sisteme gaz-solid şi aplicaţiile lor în industrie*, Bucureşti: Editura Tehnică, 1983.
[13]. Kunii D., Levenspiel O., *Fluidization engineering*, New York, John Wiley & Sons, Inc., 1969.
[14]. Baskakov A. P., *Nagrev I ohlajdenie metallov v kipiasciem sloe*, Moscova: Metalurghia, 1974.
[15]. Ivanuş Gh., Todea I., Pop Al., Nicola S., Damian Gh., *Ingineria fluidizării*, Bucureşti, Editura Tehnică, 1996.
[16]. Esayan L., Esayan M., *Fluidizarea*, Editura Tehnică, Bucureşti, 1959.
[17]. Samoila C. Drugă, Stan I., *Cuptoare şi instalaţii de încălzire*, Bucureşti, Editura Didactică şi Pedagogică, 1983.
[18]. Bâclea Adolf, Dobrovici Sorin, *Quality Engineering Applications on the Nitriding Steel in Fluidized Bed*, The Annals of "Dunarea de Jos" University of Galati, Fascicle IX, Metallurgy and Materials Science, p. 81-87, ISSN1453-083X, 2002.

THE ANNALS OF "DUNAREA DE JOS" UNIVERSITY OF GALATI
FASCICLE IX. METALLURGY AND MATERIALS SCIENCE
N°. 3 - 2021, ISSN 2668-4748; e-ISSN 2668-4756
Article DOI: https://doi.org/10.35219/mms.2021.3.08

APPLICATION OF THE NATURAL CELLULOSIC SUPPORTS FOR THE TREATMENT OF THE INDUSTRIAL EFFLUENTS

Andreea BONDAREV
Petroleum-Gas University of Ploiesti, Faculty of Petroleum Processing and Petrochemistry, Chemistry Department, 39 Bucharest Blvd., 100680, Ploieşti, Romania
e-mail: andreeabondarev@yahoo.com

ABSTRACT

Wastewater treatment is one of the most important concerns of the research studies in the field of environmental protection. The current study relates to the removal of Crystal violet dye from aqueous solutions through adsorption experiments onto natural cellulosic supports.

Various waste materials that have in their composition lignocellulose are adsorbent supports with low costs for the removal of heavy metal ions and dyes from aqueous solutions.

The use of chemically modified sawdust to obtain an inexpensive adsorbent for removing the Crystal violet dye (CV) from synthetic aqueous solutions has been presented in this research paper. The influence of some important parameters such as: initial dye concentration, adsorbent dose, contact time and temperature on adsorption efficiency for this dye removal have been studied. The Freundlich, Langmuir and Temkin mathematical models have been used to evaluate the data of Crystal violet adsorption from aqueous media using wood sawdust.

The research study shows that beech wood sawdust (Fagus sylvatica), as an agricultural waste which is readily available and relatively inexpensive has the potential to be an applicable alternative adsorbent for Crystal violet dye removal from industrial effluents.

KEYWORDS: adsorption, sawdust, dyes, removal, agricultural wastes

1. Introduction

Discharge of industrial effluents containing hazardous components, such as phenolics, heavy metals and dyes, even at low concentrations produce a negative impact on the environment [1, 2]. Dyes are notorious organic contaminants that can be discharged into the environment during textile, dye, leather, paints and paper manufacturing [1, 3, 4].

Due to toxicity, increasing the content of industrial sludge affects water bodies and finding environmentally friendly and economically accessible treatment methods is a priority [1].

Some industry domains such as leather tanning, food, paper, plastics production, cosmetics, printing rubber and textile demand a large amount of synthetic dyes. Due to their chemical structure and large-scale production and applications, synthetic dyes present serious health risks and they can also cause environmental pollution [5-8].

Treatment of wastewater by adsorption is one of the most researched and used methods, in order to eliminate priority pollutants, such as dyes, phenolic compounds and heavy metals. Granular activated carbon has been used successfully as adsorbent support, but it is cost-prohibitive, because it requires complexing agents to improve the capacity of adsorption for various contaminants. This aspect has led to research studies for cheaper adsorbent substitutes derived from biomass, such as agricultural and wood waste [1, 4-7]. The need to use alternative methods of water treatment, with widespread applicability, has led to a new area of interest: green technology, which has addressed specific procedures for environmental sustainability by minimizing pollution and using non-renewable resources [1, 8, 9].

Different natural waste materials such as citrus peel, almond shells, coconut shell, coffee and tea leave waste, olive leaves, carrot residue are promising material for biosorption of heavy metal ions and dyes from wastewater. Adsorbent materials of agricultural origin have in their chemical structure carbohydrate

THE ANNALS OF "DUNAREA DE JOS" UNIVERSITY OF GALATI
FASCICLE IX. METALLURGY AND MATERIALS SCIENCE
No. 3 - 2021, ISSN 2668-4748; e-ISSN 2668-4756
Article DOI: https://doi.org/10.35219/mms.2021.3.08

polymers -cellulose, hemi-cellulose and lignin, which act as active centres for synthetic dyes removal [5, 10-14].

There are many solid agricultural waste products that are available in large quantities, they are biodegradable and might be potential sorbents, due to their physico-chemical characteristics [2, 11, 12-15]. The adsorption of synthetic dyes on materials based on wood waste has been extensively studied in research projects. Wood waste can be burned, then fermented to obtain methane and alcohols, for the production of green energy, biofuels or certain industrial chemicals. Generally, sawdust is considered a timber-industrial waste, but it can become a valuable commodity, considering these directions: manufacturing, energy and agricultural utilization [9, 10]. Sawdust can be processed by advanced industrial methods, obtaining various products: adhesives, epoxy resins, fertilizers, adsorbent materials, floor tile, cleaning products and wood fillers [1, 10, 12]. It is well documented that the adsorption capacity of sawdust is significantly reliant on the species of wood [5, 14]. Sawdust, as an agricultural waste which is highly efficient, readily available and relatively inexpensive, has the potential to be an applicable alternative adsorbent for dyes removal from synthetic domestic wastewater [5, 13, 14].

This study showed that the beech wood sawdust could be employed as low-cost and effective sorbent for the removal of dyes from aqueous solution.

This study showed that chemically modified beech wood sawdust (Fagus sylvatica) could be used as effective sorbent for the removal of Crystal violet dye (CV) from synthetic aqueous solutions. The influence of some important parameters such as: initial dye concentration, adsorbent dose, contact time and temperature on adsorption efficiency for this dye removal have been studied.

The Langmuir, Temkin and Freundlich isotherms have been selected to study dye - adsorbent systems, in order to establish the optimum conditions for the adsorption of Crystal violet dye from aqueous solutions.

2. Materials and methods

2.1. Dye solution

The cationic dye Crystal violet ($C_{25}H_{30}N_3Cl$, λ_{max} = 590 nm and MW= 407.98 g/mol) was purchased from Sigma-Aldrich and used without further purification.

A stock solution of Crystal violet (CV) dye (1000 mg/L) was prepared by dissolving 1 g of dye in 1 L of deionized water. Different concentrations of Crystal violet (CV) dye used in these experiments were prepared by diluting the stock solution with distilled water.

Calibration plots were made in the concentration range of 5-25 mg/L. Dye concentrations were determined at the wavelength corresponding to the highest absorbance, λ_{max} = 590 nm. The UV–Vis Spectrophotometer (Jasco, model V-550) was employed to measure residual dye concentrations.

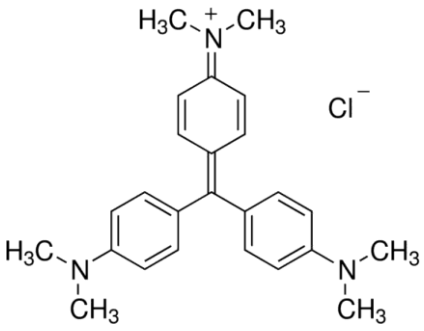

Fig. 1. *Chemical structure of Crystal violet dye (CV) (source: https://www.sigmaaldrich.com)*

2.2. Preparation of the adsorbent support

Beech wood sawdust (Fagus sylvatica) has been dried in an oven for 24 h, at a temperature of 80 °C and then it was treated at room temperature with an aqueous solution of NaOH 1N. This adsorbent support has been oven dried for 8 hours at a temperature of 80 °C, then it was ground and sieved, to get the homogenous particle sized material (between 0.3-0.6 mm in diameter). The characterization of the adsorbent material was described in a previous study [14].

2.3. Adsorption studies

The influence of some important parameters such as: initial dye concentration (60-150 mg/L), adsorbent dose (0.3-1 g), contact time (20-100 min) and temperature (25-50 °C) on the adsorption efficiency for this dye removal have been studied.

THE ANNALS OF "DUNAREA DE JOS" UNIVERSITY OF GALATI
FASCICLE IX. METALLURGY AND MATERIALS SCIENCE
Nº. 3 - 2021, ISSN 2668-4748; e-ISSN 2668-4756
Article DOI: https://doi.org/10.35219/mms.2021.3.08

The cellulosic waste material was added into 100 mL of dye solutions with initial concentrations ranging between 60 and 150 mg/L, respectively. The resulting suspensions have been shaken at a constant stirring rate (200 rpm) for 1 h to reach equilibrium. After each experiment, the adsorbent was separated using Whatman 42 blue band filter paper and each sample of the treated aqueous solution has been evaluated to detect the residual dye using UV-Vis spectrometry. The tests were repeated in duplicate.

Dye adsorbed per unit mass of the adsorbent (q_e, *mg/g*) and percentage dye removal (R%) for all samples have been calculated using Eq. 1 and Eq. 2, respectively [1-5, 10-13].

$$q_e = (C_0\text{-}C_e)\frac{V}{W} \quad (1)$$

$$\%R = \frac{C0-Ce}{C0} \cdot 100 \quad (2)$$

where C_0 (mg/L) is the initial concentration of Crystal violet dye, C_e (mg/L) is the final Crystal violet dye concentration, V is the total volume of the solution (L) and W is the weight of the adsorbent support (g).

The achieved results from investigating the effect of contact time, initial concentration of pollutant, adsorbent dose and temperature have been used to study the isotherm modeling of the adsorption process.

3. Results

3.1. The effect of initial concentration

The effect of the initial dye concentration on the adsorption rate has been determined from the dye solution containing 60 mg/L, 80 mg/L, 100 mg/L and 150 mg/L. The adsorption experiments have been carried out at room temperature i.e., 22±2 ºC, the adsorbent amount was of 0.5 g and contact time 60 min, using an Orbital Shaker Incubator, at 200 rot/min.

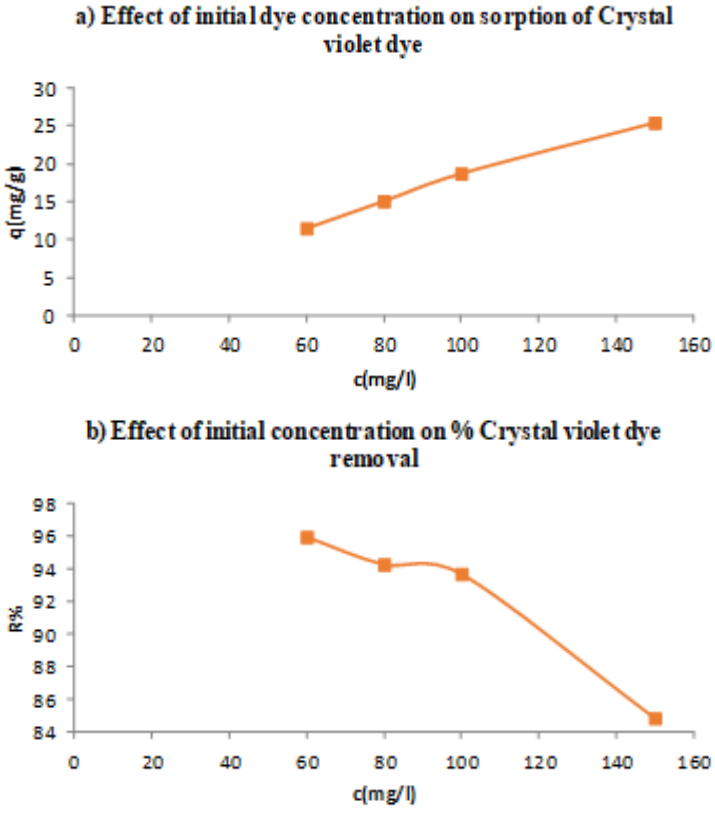

Fig. 2. *The effect of initial concentration on Crystal violet dye adsorption on the beech wood sawdust (Fagus sylvatica)*

The adsorption mechanism is dependent on the initial dye concentration: at low concentrations, the pollutant is adsorbed by specific sites of sawdust; increasing concentrations, the specific sites are saturated and the exchange sites are filled [10-13].

THE ANNALS OF "DUNAREA DE JOS" UNIVERSITY OF GALATI
FASCICLE IX. METALLURGY AND MATERIALS SCIENCE
Nº. 3 - 2021, ISSN 2668-4748; e-ISSN 2668-4756
Article DOI: https://doi.org/10.35219/mms.2021.3.08

3.2. The effect of adsorbent dose

The effect of adsorbent dose has been investigated in the range 0.3-1 g, for 100 mg dye/L. The adsorption experiments have been carried out at the contact time 60 min and using an Orbital Shaker Incubator, at 200 rot/min.

The increase in the removal efficiency by increasing the adsorbent dose can be due to the increment of active sites and sufficient surface for adsorbing of crystal violet molecules. The decrement in adsorption capacity with an increase in adsorption dose can be caused by various factors such as overlapping of active sites at high doses of adsorbent support [1, 8, 14].

The quantity of adsorbent applied in the adsorption process is crucial because it influences the sorbent–sorbate ratio in the adsorption process and also in cost forecasting [4].

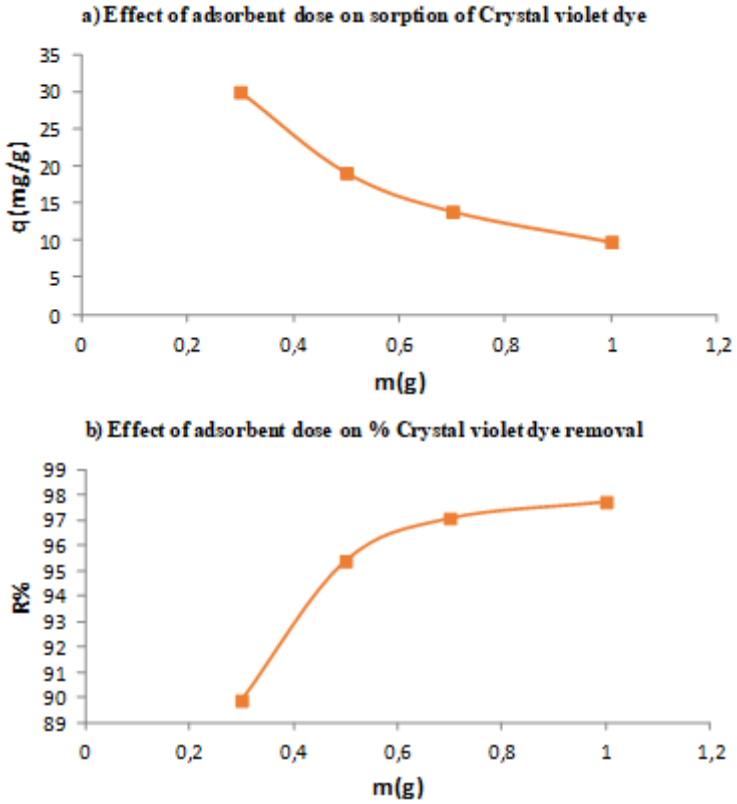

Fig. 3. *The effect of adsorbent dose on the adsorption process of Crystal violet dye on chemically modified beech wood sawdust (Fagus sylvatica)*

3.3. The effect of temperature

The effect of temperature on the adsorption rate has been investigated in the range 25–50 ºC, for 100 mg dye/L. The adsorption experiments have been carried out using the adsorbent amount of 0.7 g, contact time 60 min and an Orbital Shaker Incubator, at 200 rot/min.

Temperature has an important impact on the adsorption process. The experimental results showed that the adsorption capacity increased as temperature increased up to 50 ºC.

Temperature plays an important role in adsorption process because it influences mobility and solubility of dye molecules in aqueous solution and surface properties of adsorbent. Increase in temperature result in an increased rate of diffusion of dye molecules across the external boundary layer of the adsorbent particles and inside their internal pores [3, 8, 9].

THE ANNALS OF "DUNAREA DE JOS" UNIVERSITY OF GALATI
FASCICLE IX. METALLURGY AND MATERIALS SCIENCE
Nº. 3 - 2021, ISSN 2668-4748; e-ISSN 2668-4756
Article DOI: https://doi.org/10.35219/mms.2021.3.08

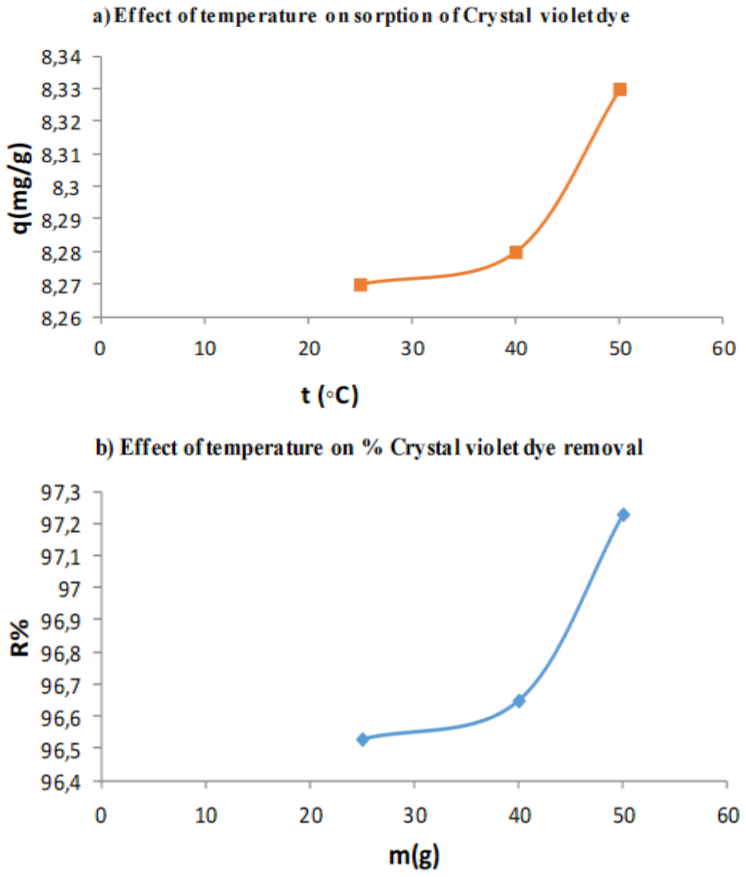

Fig. 4. *The effect of temperature on the adsorption process of Crystal violet dye on chemically modified beech wood sawdust (Fagus sylvatica)*

3.4. The effect of contact time

The effect of contact time on the adsorption rate has been investigated in the range of 20-100 min, for 100 mg dye/L. The adsorption experiments have been carried out using the adsorbent amount of 0.7 g and an Orbital Shaker Incubator, at 200 rot/min.

Figure 5 shows the effect of contact time on the adsorption process of Crystal violet on wood sawdust powder and it clearly indicates that adsorption increased with the increase of the contact time.

The period of contact between the sorbent and biosorbate is very important in costing when designing a biosorption system for large scale application in an industry [3, 10].

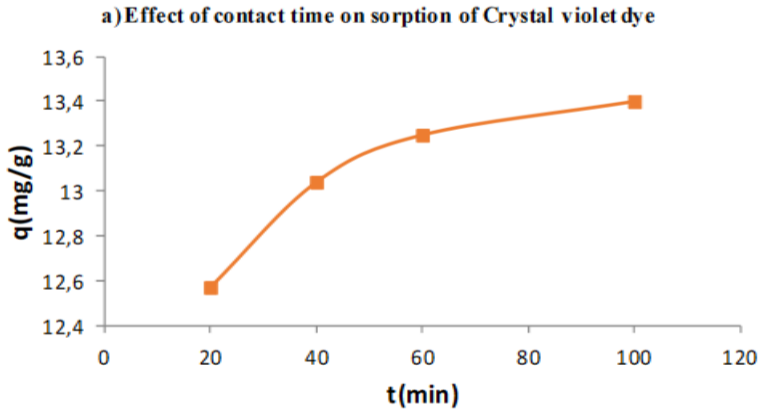

THE ANNALS OF "DUNAREA DE JOS" UNIVERSITY OF GALATI
FASCICLE IX. METALLURGY AND MATERIALS SCIENCE
N°. 3 - 2021, ISSN 2668-4748; e-ISSN 2668-4756
Article DOI: https://doi.org/10.35219/mms.2021.3.08

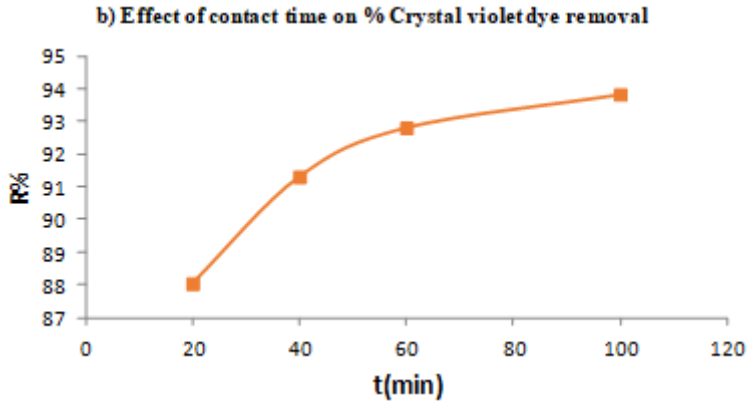

Fig. 5. *The effect of contact time on the adsorption process of Crystal violet dye on chemically modified beech wood sawdust (Fagus sylvatica)*

4. Discussion

4.1. Isotherm study

Adsorption isotherms are mathematical models that describe the distribution of the adsorbate species among the solid and liquid phases. The study of adsorption isotherms provides an effective perspective for determining the adsorption mechanism [5, 7-9]. An adsorption isotherm is a curve which describes the phenomenon governing the retention (or release) or mobility of a substance from aquatic media to a solid-phase, considering a constant temperature and pH [3, 5-8].

Freundlich, Langmuir and Temkin adsorption isotherms have been used to evaluate the data of Crystal violet removal from aqueous media using chemically modified wood sawdust.

The isotherm expressions are given in Equations (3), (4) and (5) [3, 7-10].

Freundlich: $q_e = K_F \cdot C_e^{\,1/n}$ (3)

where: K_F (mg g^{-1}) is the Freundlich constant related to the adsorption capacity; 1/n represents a parameter related the adsorption intensity; q_e (mg g^{-1}) is the equilibrium adsorption concentration of dye per gram of adsorbent; C_e (mg L^{-1}) represents the concentration of the solute in solution at equilibrium [3, 7-10].

Langmuir: $q_e = q_m \cdot K_L \cdot C_e \,/\, 1 + K_L \cdot C$ (4)

where: q_e (mg g^{-1}) represents the amount of solute adsorbed per amount of adsorbent; C_e (mg L^{-1} or mmol L^{-1}) is the aqueous-phase concentration of adsorbate (mg/L) at equilibrium.; q_m (mg g^{-1}) represents the maximum adsorption capacity; K_L (L/mg) is the Langmuir constant related to the free adsorption energy (L mg^{-1} or L $mmol^{-1}$) [3, 7-10].

Temkin: $q = \frac{RT}{b} \ln (K_T \cdot C_e)$ (5)

where K_T (L mg^{-1}) and b_T (KJ/mol) are Temkin isotherm constants linked with the adsorption heat and the equilibrium binding constant [3, 7-10].

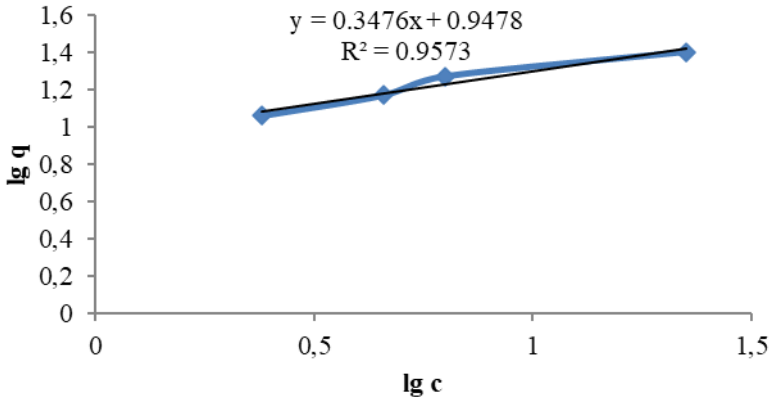

Fig. 6. *The linearized Freundlich adsorption isotherm for the sorption of Crystal violet by beech wood sawdust (Fagus sylvatica)*

THE ANNALS OF "DUNAREA DE JOS" UNIVERSITY OF GALATI
FASCICLE IX. METALLURGY AND MATERIALS SCIENCE
Nº. 3 - 2021, ISSN 2668-4748; e-ISSN 2668-4756
Article DOI: https://doi.org/10.35219/mms.2021.3.08

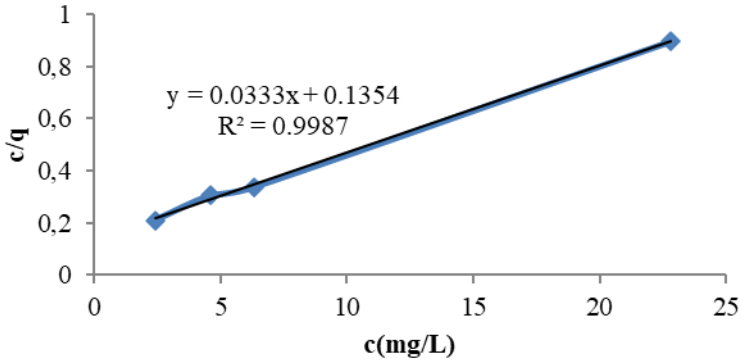

Fig. 7. *The linearized Langmuir adsorption isotherm for the sorption of Crystal violet by beech wood sawdust (Fagus sylvatica)*

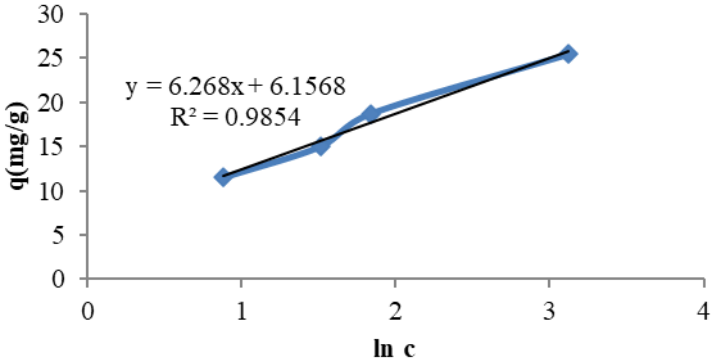

Fig. 8. *The Temkin adsorption isotherm for the sorption of Crystal violet by beech wood sawdust (Fagus sylvatica)*

The results suggest that Crystal violet dye has been favourably adsorbed by modified wood sawdust with high values of the correlation coefficient (R^2 = 0.9987), indicating that the Langmuir isotherm has been best fitted for the adsorption of dye on modified wood sawdust.

Langmuir isotherm model infers that the adsorption occurs at specific homogeneous sites on the adsorbent and it is used in many monolayer adsorption processes [3, 8-10]. It is noteworthy to point out that experimental data fitted well both Langmuir and the Temkin adsorption isotherms models indicating that both models are suitable for describing the adsorption equilibrium of this dye in the studied concentration ranges.

5. Conclusions

This paper is part of a series of works aiming at valorising sawdust for the removal of synthetic dyes from aqueous solution by adsorption method.

The use of adsorbents based on natural cellulosic supports for the removal of synthetic dyes from wastewater has many benefits, including the cost of investment and outstanding performance. This research study revealed that chemically modified beech wood sawdust (Fagus sylvatica) is a viable and affordable adsorbent for the adsorptive removal of Crystal violet dye from contaminated wastewater, with over 97% dye removal.

The effect of temperature, contact time, adsorbent mass and initial dye concentration has been investigated to evaluate the performance of modified wood sawdust for adsorption of Crystal violet from aqueous solutions.

The Langmuir, Temkin and Freundlich mathematical models were suitable to describe the equilibrium behavior of Crystal violet dye adsorption using modified beech wood sawdust. The experimental data showed the best fit to Langmuir model, with high correlation coefficient (R^2 = 0.9987) indicating that the model was appropriate to describe the adsorption process of Crystal violet dye onto beech wood sawdust (Fagus sylvatica), suggesting also the spontaneous nature of the process.

This study proved that sawdust, as an agricultural waste which is highly efficient, readily available and relatively inexpensive has the potential to be an applicable alternative adsorbent for Crystal violet dye removal from aqueous media.

References

[1]. Saeed A., Sharif M., Iqbal M., *Application potential of grapefruit peel as dye sorbent: Kinetics, equilibrium and mechanism of crystal violet adsorption*, Journal of Hazardous Materials, 179, p. 564-572, 2010.

[2]. Amarasinghe B. M., Williams R. A., *Tea waste as a low-cost adsorbent for the removal of Cu and Pb from wastewater*, Chemical Engineering Journal, 132 (1-3), p. 299-309, 2007.

[3]. Wanyonyi W. C., Onyari J. M., Shiundu P. M., *Adsorption of congo red dye from aqueous solutions using roots of eichhornia crassipes: kinetic and equilibrium studies*, Energy Procedia, 50, p. 862-869, 2014.

[4]. Oguntimein G. B., *Biosorption of dye from textile wastewater effluent onto alkali treated dried sunflower seed hull and design of a batch adsorber*, J. Environ. Chem. Eng., 3(4), p. 2647-2661, 2015.

[5]. Martins L., Vieira Rodrigues J., Herrera Adarme O., Sacramento Melo T., Gurgel L., Gil L., *Optimization of cellulose and sugarcane bagasse oxidation: Application for adsorptive removal of crystal violet and auramine-O from aqueous solution*, Journal of Colloid and Interface Science, 494, p. 223-241, doi: 10.1016/j.jcis.2017.01.085, 2017.

[6]. Gilbert K., Wycliffe C., Joyce J., Esther N. M., *Adsorption of toxic crystal violet dye using coffee husks: Equilibrium, kinetics and thermodynamics study*, Scientific African, 5, p. 1-11, 2019.

[7]. Bombos D., Ganea R., Matei V., Marinescu C., Bondarev A., Mihai S., Natu T., Tamas I., *Modified Bentonite for Purification of Dyeing Waste WaterRev*, Chim., 65 (8), p. 976-982, 2014.

[8]. Lafi R., Rezma S., Hafiane A., *Removal of toluidine blue from aqueous solution using orange peel waste (OPW)*, Desalin. Water Treat., 56(10), p. 1-12, 2014.

[9]. Razmovski R., Ciban M., *Biosorption of Cr(VI) and Cu(II) by waste tea fungal biomass*, Ecological Engineering, 34(2), p. 179-186, 2008.

[10]. Rajeswari M., Revanth T., Aniruth A., Prasad B., *Removal of Crystal Violet dye from aqueous solution using water hyacinth: Equilibrium, kinetics and thermodynamics study*, Resource-Efficient Technologies, 3 (1), p. 71-77, 2017.

[11]. Hou S., *Adsorption properties of pomelo peels against methylene blue in dye wastewater*, Adv. Mater. Res., 634-638, p. 178-181, 2013.

[12]. Erfani M., Javanbakht V., *Methylene Blue removal from aqueous solution by a biocomposite synthesized from sodium alginate and wastes of oil extraction from almond peanut*, Int. J. Biol. Macromol, 114, p. 244-255, 2018.

[13]. Rominiyi O., Adaramola B., Ikumapayi O., *Potential Utilization of Sawdust in Energy, Manufacturing and Agricultural Industry: Waste to Wealth*, World Journal of Engineering and Technology, 05(03), p. 526-539, 2017.

[14]. Bondarev A, Gheorghe C. G, Gheorghe V., Bombos M., *Removal of Dyes from Textile Wastewater Using Sawdust as Low-cost Biosorbent*, Rev. Chim., 71 (3), p. 387-396, 2020.

[15]. Apafaian A. I., Proto A. R., Borz S. A., *Performance of a mid-sized harvester-forwarder system in integrated harvesting of sawmill, pulpwood and firewood*, Ann. For. Res., 60(2), p. 227-241, doi: 10.15287/afr.2017.909, 2017.

[16]. Bello K., Sarojini B. K., Narayana B., Rao A., Byrappa K., *A study on adsorption behavior of newly synthesized banana pseudo-stem derived superabsorbent hydrogels for cationic and anionic dye removal from effluents*, Carbohydr. Polym., 181, p. 605-615, doi: 10.1016/j.carbpol.2017.11.106, 2018.

[17]. Monda L., M. K., *Removal of Pb(II) ions from aqueous solution using activated tea waste: Adsorption on a fixed-bed column*, Journal of Environmental Management, 90(11), p. 3266-3271, 2009.

MANUSCRISELE, CĂRŢILE ŞI REVISTELE PENTRU SCHIMB, PRECUM ŞI ORICE CORESPONDENŢE SE VOR TRIMITE PE ADRESA:

MANUSCRIPTS, REVIEWS AND BOOKS FOR EXCHANGE COOPERATION, AS WELL AS ANY CORRESPONDANCE WILL BE MAILED TO:

LES MANUSCRIPTS, LES REVUES ET LES LIVRES POUR L'ECHANGE, TOUT AUSSI QUE LA CORRESPONDANCE SERONT ENVOYES A L'ADRESSE:

MANUSCKRIPTEN, ZIETSCHRITFTEN UND BUCHER FUR AUSTAUCH SOWIE DIE KORRESPONDENZ SID AN FOLGENDE ANSCHRIFT ZU SEDEN:

After the latest evaluation of the journals by the National Center for Science Policy and Scientometrics (**CENAPOSS**), in recognition of its quality and impact at national level, the journal will be included in the B^+ category, 215 code (http://cncsis.gov.ro/userfiles/file/CENAPOSS/Bplus_2011.pdf).

The journal is already indexed in:

DOAJ: https://doaj.org/

SCIPIO-RO: http://www.scipio.ro/web/182206

EBSCO: http://www.ebscohost.com/titleLists/a9h-journals.pdf

Google Academic: https://scholar.google.ro

Index Copernicus: https://journals.indexcopernicus.com

Crossref: https://search.crossref.org/

The papers published in this journal can be viewed on the website: http://www.gup.ugal.ro/ugaljournals/index.php/mms

Name and Address of Publisher:
Contact person: Elena MEREUȚĂ
Galati University Press - GUP
47 Domneasca St., 800008 - Galati, Romania
Phone: +40 336 130139
Fax: +40 236 461353
Email: gup@ugal.ro

Name and Address of Editor:
Prof. Dr. Eng. Marian BORDEI
"Dunarea de Jos" University of Galati, Faculty of Engineering
111 Domneasca St., 800201 - Galati, Romania
Phone: +40 336 130208
Phone/Fax: +40 336 130283
Email: mbordei@ugal.ro

AFFILIATED WITH:

- THE ROMANIAN SOCIETY FOR METALLURGY
- THE ROMANIAN SOCIETY FOR CHEMISTRY
- THE ROMANIAN SOCIETY FOR BIOMATERIALS
- THE ROMANIAN TECHNICAL FOUNDRY SOCIETY
- THE MATERIALS INFORMATION SOCIETY (ASM INTERNATIONAL)

Edited under the care of the FACULTY OF ENGINEERING

Annual subscription (4 issues per year)

Fascicle DOI: https://doi.org/10.35219/mms

Volume DOI: https://doi.org/10.35219/mms.2021.3

Editing date: 15.09.2021
Number of issues: 200
Printed by Galati University Press (accredited by CNCSIS)
47 Domneasca Street, 800008, Galati, Romania